THE DISSERTATION COMMITTEE FOR CHUNGMIN HAN

CERTIFIES THAT THIS IS THE APPROVED VERSION OF THE FOLLOWING DISSERTATION:

A MULTIMODAL IMAGING PERSPECTIVE ON HUMAN SENSORIMOTOR BEHAVIOR

Committee:

James Sulzer, Supervisor

Paul Ferrari, Co-Supervisor

Lawrence Abraham

David Schnyer

Thomas Yankeelov

A MULTIMODAL IMAGING PERSPECTIVE ON HUMAN SENSORIMOTOR BEHAVIOR

BY

CHUNGMIN HAN

DISSERTATION

Presented to the Faculty of the Graduate School of

The University of Texas at Austin

in Partial Fulfillment

of the Requirements

for the Degree of

DOCTOR OF PHILOSOPHY

THE UNIVERSITY OF TEXAS AT AUSTIN

DECEMBER 2021

DEDICATION

To my family

ACKNOWLEDGMENTS

Above all, I would like to acknowledge and thank my advisor, Dr. James Sulzer, for providing unconditional support throughout my journey of pursuing a Ph.D. His idea of conducting research in the hope to benefit society is truly ethical, which I respect above what I have experienced so far. I often had rough times picking up new skills, making critical decisions in research, and questioning myself. He was always supportive and rooting up for my accomplishments. Thank you for being an optimistic, enthusiastic, and friendly advisor.

I would also like to thank both of my co-advisors, Dr. Paul Ferrari, and Dr. David Ress guiding me with each project with a high level of expertise. I learned the methodology in-depth, both provided me with a countless number of rigorous discussions and bared endless patience with me. I would not have been leading two projects without your help. Thank you for being supportive and connecting me to the community for me to meet new colleagues and researchers. I truly admire high-experienced guidance. I would also like to show my gratitude to my dissertation committee members for providing me with valuable feedback on my research. Thank you for providing me with various perspectives on my work, which helped me think outside the box.

I would also like to thank the members of Rewire lab, for being together along my journey. I appreciated discussing results together, writing on the board to understand such theory correctly, and developing new ideas to tackle the next problem one after another. Coffee break from time to time sustained my spirit when I had to go through another gloomy day. It is always good to have nice company beside you, who understands the situation at best, hope all of your journeys turn you into better yourself. I would like to

address my sincere thanks to friends, colleagues, and seniors who were there with me when I desperately needed fresh eyes and comfort to overcome my challenges.

Finally, I appreciate my loving family, supporting me unlimitedly, and having faith in completing my Ph.D. None of this would have been possible without their constant love, encouragement, and patience until now. I thank you again, the unbelievable support they have provided me during the pandemic.

My journey in the Ph.D. program had left me with a number of remarkable memories where I can bring back to my mind as I move forward in my life. The experience was truly unique, hope that I have become a wiser person.

ABSTRACT

A MULTIMODAL IMAGING PERSPECTIVE ON HUMAN SENSORIMOTOR BEHAVIOR

Chungmin Han, Ph.D.

The University of Texas at Austin, 2021

Supervisors: James Sulzer

Paul Ferrari

Understanding motor control has been critical to motor rehabilitation after brain injuries. Neural activity can be detected non-invasively using functional magnetic resonance imaging (fMRI) that measures hemodynamic response and magnetoencephalography (MEG) that measures electrophysiological dynamics. In this dissertation, two scientific questions were investigated with two distinct functional neuroimaging techniques. First, I used fMRI to search for neural correlates of spasticity in individuals with chronic stroke. Spasticity, defined as velocity-dependent resistance to passive stretch, is common after stroke and imposes significant therapeutic challenges. It is believed that disinhibition of brainstem nuclei, possibly the lateral vestibular nuclei or pontine reticular formation, are primarily involved. As such, I aimed to localize the activity of these individual brainstem nuclei via 3T functional magnetic resonance imaging (fMRI) in a cohort of chronic stroke patients and healthy controls. Using both acoustic and visual stimuli to activate the brainstem without inducing motion in the participants. The results

showed that the response of stroke patients was dominantly more correlated to age, duration of a stroke, and total brainstem volume. Another significant motor deficit that stroke patients face is the loss of individual finger control that allows fine motor control like precision pinch. In the second part of my dissertation, I investigated neural correlates of dynamic precision grip tasks, a predictor of sensorimotor impairment or decline. Visuomotor control for precision grip relies on an extensive cortical network for which research has traditionally focused on frontal and parietal regions subserving executive and visuomotor integration functions, respectively. However, the temporal dynamics of how visuomotor integration is expressed in the form of oscillatory modulation as a combination of both low and high-level functions remain unclear. Thus, I used MEG to measure dynamic oscillatory activity in the sensorimotor and visual areas to investigate their contribution to performance in a dynamic precision grip task in healthy individuals. A custom MEG-compatible sensor measured forefinger and thumb forces separately, which controlled the position of a cursor on the screen. My findings suggest that cortical oscillations in both sensorimotor and visual areas can dissociate task and movement parameters during dynamic pinch tasks and that they may share a common network for visuomotor control. My ultimate goal is to better address how the spatial and temporal profiles of neural activity connect behavior to pathologic responses.

TABLE OF CONTENTS

LIST OF TABLES

LIST OF FIGURES

CHAPTER 1

Introduction

Stroke is a leading cause of long-term adult disability. The aging population and accumulating risk factors contribute to an increased lifetime risk of stroke [1]. Direct and indirect costs of stroke in the United States between 2016 to 2017 were $49.8 billion. The direct medical costs are projected to more than double from $36.7 billion to $94.3 billion between 2015 and 2035, with a projected increase in costs from those over 80 years of age. A primary cause of persistent disability post-stroke is incomplete motor recovery [2]. The biological recovery of motor function occurs primarily during the first months after stroke, where the emphasis has been posed on intensive early intervention [3, 4]. However, the recovery itself has been spontaneous and the results of early intervention have also been mixed and complex across individuals [5]. Even with intensive therapy, upper limb impairment resolves up to 70% of the baseline function at maximum recovery [6]. The majority of stroke survivors live with a limited ability to perform skilled hand movements necessary for daily functioning [7]. It is crucial that we need to improve our understanding of the neurophysiology of motor control. Among non-invasive neuroimaging techniques, we introduce functional magnetic resonance imaging (fMRI) and magneto-encephalography (MEG) to reveal the neurophysiology of motor control.

Functional magnetic resonance imaging captures the metabolic function sharing the same physical principles as magnetic resonance imaging (MRI). The strong homogenous

magnetic field in the MRI system aligns hydrogen nuclei (or protons) with the main magnetic field vector, where hydrogen nuclei in the water and lipids compose a large proportion of the human body [8]. The images are collected by sending out the radiofrequency pulse that spins the hydrogen then relaxes to return to its original orientation. The signal depends on the magnetic properties of this spin's micro-environment; allowing to determine the amount of water (or lipid, or other hydrogen-containing tissues) at any spatial point within the body. The MR imaging most often target to produce information related to brain function called BOLD (blood oxygenation level-dependent) contrast imaging. The BOLD signal is sensitive to changes in the state of oxygenation of the hemoglobin [9]. Within any specific imaging voxel (within the brain) the proportion of deoxyhemoglobin relative to oxyhemoglobin dictates the MR signal in the BOLD image; areas with a high concentration of oxyhemoglobin give a higher signal than areas with low concentration. The level of tissue oxygenation is related to the neuronal activity that local variation of the blood supply accords with local variations of the functional activity [10]. Thus, fMRI is based on hemodynamic responses to neuronal activity [11]. The occurrence of a stimulus in a certain brain region accompanies a transient increase in deoxyhemoglobin concentration, which is referred to as an initial dip [12]. This dip is followed with an increase in the oxy/deoxyhemoglobin ratio attributed to high MR signal. This signal increase is proportional to the underlying neural activity and ultimately reaches a plateau if the stimulus is maintained for a subsequent amount of time. After the termination of the stimulus, the MR signal returns to the baseline and undershoots it. By using BOLD fMRI imaging, it is possible to indirectly detect the increase in neuronal

activity associated with a particular task. BOLD images are typically acquired every 2-3 seconds and compared with the model of the expected BOLD response based on the experimental design using a general linear model. The BOLD response typically ranges from 2 – 10% signal change with a 3T magnet [13]. The ability to capture changes in magnetic spins in hydrogen nuclei provides very high spatial resolution (<1mm) over the whole brain.

Due to the high spatial resolution and whole brain coverage of fMRI, I aimed to identify the source of spasticity in chronic stroke patients. Spasticity is a disorder of the sensorimotor system characterized by a velocity-dependent increase in tonic stretch reflexes [14]. Despite the incidence of spasticity in post-stroke survivors and the significant challenge that it poses for patient care, the pathophysiology of post-stroke spasticity remains poorly understood. Although accumulated evidence supports the supraspinal origins of spasticity, it is currently not possible to distinguish between two potentially contrasting theories, one supporting the dominant root cause being in the lateral vestibular nuclei (LVN) and their descending pathways (vestibulospinal), and the other emphasizing the contribution of the reticular nuclei (RN) and their own descending pathways (reticulospinal tract). In an effort to resolve this debate, I aimed to measure in vivo activity of the brainstem in patients with post-stroke spasticity. One recent method of delineating the origin of spasticity is through auditory stimulation, which supposedly activates the LVN by stimulating the sternocleidomastoid muscles [15]. However, detractors believe this may simply be a startle reflex acting through the RN. In this paper, I aimed to:

Aim 1. Localize lateral vestibular nuclei and reticular formation in healthy individuals via visual/acoustic stimuli with fMRI (Chapter 2)

Aim 2. Investigate lateralization of the brainstem response of post-stroke individuals to visual/acoustic stimuli (Chapter 3).

Another motor deficit commonly found in neuromuscular disease is the loss of the upper limb and fine control of the hand. Precision grip, involving coordination of the thumb and index finger, is critical to everyday function of the hand. Precision grip often incorporates visuomotor integration, starting from perception to action in order to achieve specific motor goals. Integration of visual information during object manipulation provides a foundation for internal models of body movement within the external environment [16] and helps to improve accuracy and consistency during goal-directed movements [17]. The posterior parietal cortex (PPC) has been shown to be an essential functional hub within a wide cortical network that subserves visuomotor transformations [18-21]. While there has been extensive research on the role of the PPC, primary motor and sensorimotor cortex (SMC), and executive frontal regions, relatively little is known about the involvement of the primary visual cortex within this greater visuomotor network. The primary role of the motor cortex (M1) is well established. Along with the supplementary motor area (SMA), M1 encodes signals for generating high-level motor output through the corticospinal system [22] of various degrees of complexity [23-26]. However, more recent studies have found that the M1 area also directly encodes visual information associated with the movement planning and sensory feedback [27-30], shedding light on the hierarchical

structure of an integrated action-perception system supporting predictive behavior [31-33]. The fact that M1 motor planning changes the state of somatosensory area indicates M1 prepares S1 to anticipate the sensory information received during the movement [34]. While much less is known about how the primary visual cortex couples to the motor system, there is some evidence of motor representation [35]. Investigation of this dynamically intricate system requires neuroimaging modality with high temporal resolution.

Magnetoencephalography (MEG) detects magnetic field changes generated by activated neurons [36]. In contrast to fMRI, MEG directly measures electromagnetic fields emanating from the brain with a high temporal resolution of less than 1ms and allows the study of neural oscillatory activity over a wide range of frequencies (1 – 600 Hz). Notably, MEG tracks neural population activity on millisecond timescales, revealing large-scale dynamics crucial to understanding brain function. By modeling inverse algorithms, it is possible to construct three-dimensional images that provide reasonable estimates of neural activity [37]. MEG is mainly sensitive to tangential currents in the brain closer to the surface and relatively insensitive to the conductive properties of the skull. The benefit of MEG is that the magnetic field generated from neurons is not distorted by the heterogeneous electrical properties of the brain, therefore the measured magnetic fields are considered undistorted cortical activity. The long apical dendrites of cortical pyramidal cells are arranged perpendicular to the cortical surface and parallel to each other. This anatomical arrangement allows the magnetic fields to sum up to magnitudes large enough to be detected at the scalp. Synchronously fluctuating dendritic currents result in equivalent

current dipoles that produce magnetic fields. The magnetic fields generated from a brain are extremely small, which requires appropriate data collection under the magnetically shielded room and highly sensitive detectors known as superconducting quantum interference devices (SQUIDs) [38]. MEG sensors are configured for measuring differential magnetic fields to reduce ambient noise. MEG systems consist of simultaneous recordings from many sensors that provide whole head coverage. MEG systems are capable of sampling the magnetic fields more than 10 kHz; however, the common sampling rate is around 1 kHz, which still provides excellent temporal resolution for measuring the dynamics of cortical neuronal activity at millisecond order [39]. With respect to the frequency range of the cortical activity, bandwidths are separated representing different functionality, defined as delta (3 – 7 Hz), alpha (8 – 13 Hz), beta (15 – 30 Hz), and gamma (>40 Hz) [40]. The frequency bandwidths I specifically focused on were alpha and beta-bands. Alpha bands are most often found in the occipital area of the brain, mainly representing the primary sensory processing, and known to represent a sensory process in the motor area as well [41]. Beta bands are most often attributed to motor processing; however, evidence shows that the beta band is related to a high-level top-down process and communicates in between the multiple cortical regions [42]. In order to measure the oscillations while performing specific motor task, I designed a sensor that minimize the effect on magnetic field measurement in the MEG room.

Aim 3. Design MRI, MEG compatible force sensor (Chapter 4)

Aim 4. Investigate temporal oscillatory dynamics of primary motor and visual area during dynamic precision grip (Chapter 5)

Understanding of sensory and motor processing represented in both primary motor and visual area will provide evidence that the high level visuomotor processing operates on both independent and network-wise process in multiple regions. In such, the oscillations reflect both bottom-up and top-down process simultaneously being updated throughout the dynamic motor tasks.

CHAPTER 2

Brainstem BOLD response to visual and acoustic stimuli

2.1 INTRODUCTION

The brainstem modulates critical functions involved in sensorimotor control [43] and is composed of many clusters of nuclei [44]. Following a stroke, the normal functions of these nuclei are disrupted by reduced cortical inhibition, resulting in impairments such as spasticity. One clear aspect of spasticity is hyperreflexia, a common movement disorder [45]. It is unclear specifically which dysfunctional nuclei are [1]primarily responsible for hyperreflexia. Miller et al. stimulated stroke survivors with acoustic-startle (AS) bursts, measuring electromyographic (EMG) activity in the sternocleidomastoid muscle as an indirect measure of activity in lateral vestibular nuclei (LVN) [46]. They found that the level of asymmetry of the response to the acoustic startle burst was correlated to clinical measures of spasticity, which are reflective of hyperreflexia. However, it is possible that the AS bursts may have activated the reticular formation (RF) [47]. Functional neuroimaging of the brainstem could help resolve this debate, but few studies have attempted neuroimaging of the vestibular nuclei (VN) and reticular formation (RF).

Functional magnetic resonance imaging (fMRI), with whole-brain coverage and

[1] Han, C., Ress, D., Nuñez, A.I.R., de la Rosa, N., Li, S. and Sulzer, J.S., 2020, July. Brainstem BOLD response to visual and acoustic stimuli. In 2020 42nd Annual International Conference of the IEEE Engineering in Medicine & Biology Society (EMBC) (pp. 2889-2892). IEEE.

millimeter resolution, is likely the optimal tool to investigate human functional brainstem activity, but there remain challenges. With a complex vascular structure and small size, the brainstem is more vulnerable than the rest of the brain to physiological artifacts such as cardiac pulsatility and respiration. Another challenge is that the hemodynamic response in the brainstem differs from the more well-researched cortex [48]. Once an activity is identified, there is not yet an atlas for functional neuroimaging that clearly defines the boundaries of the nuclei. Despite these challenges, there is some evidence that functional brainstem activity in LVN and RF can be measured. In particular, Wildenberg et al. [49] measured VN activation using an optokinetic stimulus [50], to induce the sensation of self-motion. They observed a single $2mm^3$ region of activity in the LVN after multiple comparison corrections. Thus, functional imaging of brainstem nuclei remains preliminary, and more work is needed.

My goal was to observe and differentiate functional activation in LVN and RF using 3T fMRI in healthy individuals. I aimed to reproduce the Wildenberg et al. study using optokinetic stimuli but also used an AS stimulus hypothesized to excite both VN and RF. I used a high-resolution fMRI sequence optimized for subcortical imaging and used a stimulus alternation frequency designed to avoid physiological confounds. My goal is to enable clinical assessments of brainstem function.

2.2 STUDY DESIGN

I recruited 11 neurologically intact participants with normal or corrected-to-

normal vision (mean age 46.36, SD 14.41, 4 males). After obtaining informed consent according to the University of Texas at Austin Institutional Review Board, participants underwent two sessions of fMRI scanning. All participants experienced the optokinetic stimuli and 10 experienced the AS stimuli (Figure 2.1). One subject was dropped due to technical issues with their fMRI session.

The optokinetic stimulus was a two-dimensional moving and rotating checkerboard (Figure 2.1(a)) intended to elicit a feeling of self-motion that stimulates the lateral vestibular network in healthy adults [51]. Auditory stimuli designed to elicit an Acoustic Startle Response (ASR) were based on previous work [47]. Loud (100 dB) pulses (50-ms duration, 1kHz) were played through a binaural headset at pseudorandom time points within a minimum interval of 1s. Both stimuli were presented as blocked alternations consisting of 15 seconds of stimulation followed by 15 seconds of rest. Figure 2.1 (a) illustrates the protocols. I ran both stimuli on the same individual on different days. Functional images were obtained using a T2*-weighted, spiral-trajectory sequence with TR/TE of 1.5s/38ms to obtain cubic 1.5-mm voxels [52]. An illustration of the stimuli and field of view is shown in Figure 2.1 (a). For each subject, I also collected a structural volume using a T1 MPRAGE sequence with a resolution of $1mm^3$, which was used to permit co-registration of the data obtained from the two experiments.

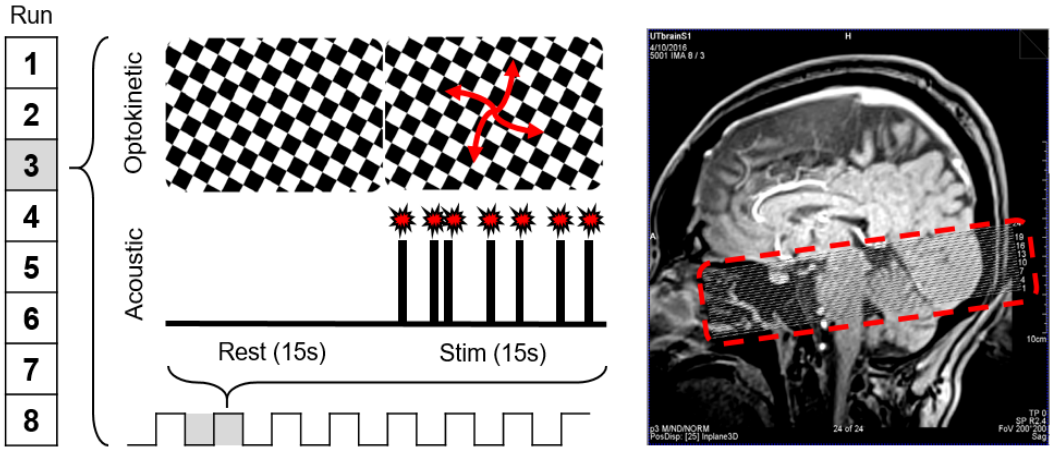

(a)

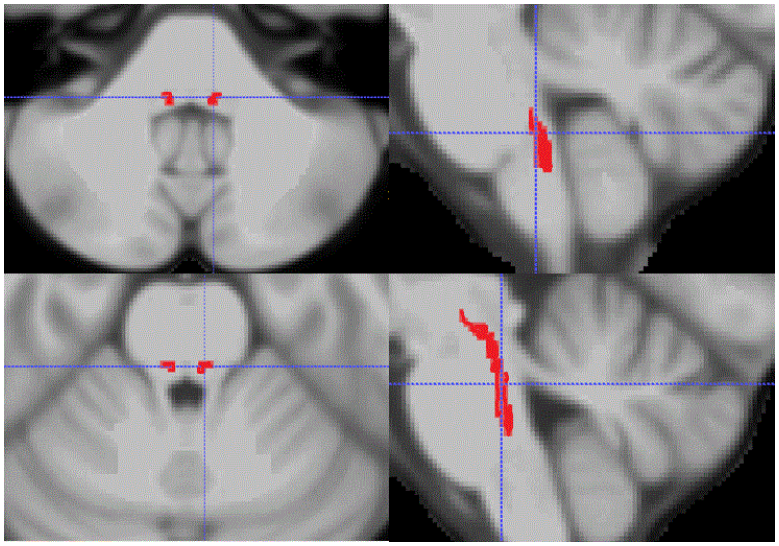

(b)

Figure 2.1. (a) Experimental design – the acoustic burst/visual optokinetic stimuli are presented during the Stim block (15 seconds) and Rest block (15 seconds). Slice orientation and limited FOV during fMRI scanning are presented. (b) The vestibular network (VN) (top) and reticular formation (RF) (bottom) were qualitatively masked in the MNI152 space.

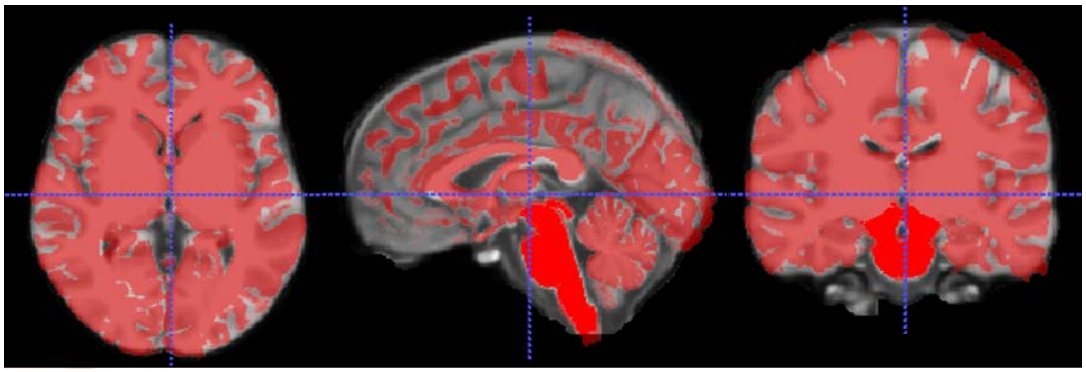

(a)

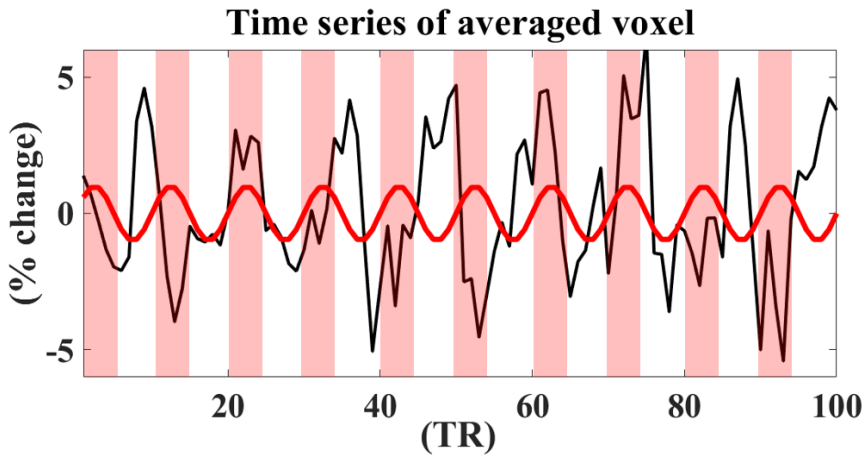

(b)

Figure 2.2. (a) Co-registration (ANTs) and segmentation (b) Representative data showing fMRI response to a sinusoidal stimulus input.

2.3 DATA ANALYSIS

I performed preprocessing including slice timing correction, movement correction within each run and between runs, registration to each subject's own native space and then co-registered to MNI152 standard space using the ANTs resliced by FreeSurfer [53] (Figure 2.2 (a)). Between TR motions were estimated with temporal

smoothing of 5 TRs to improve SNR; this approach compensates for the lower SNR obtained at these higher spatial resolutions. I discarded the runs in each subject where more than 0.75mm/TR occur, the remaining runs were averaged across 7~10 runs containing 80 TRs and 100 TRs for vection and ASR respectively. Spatial smoothing was not applied due to the need to localize small nuclei. The BOLD response was modeled to have a sinusoidal response with a delay described in the equation and in Figure 2.2 (b).

$$\boldsymbol{I(t) = Asin(2\pi f_0 t + \varphi) + n(t)}$$

$$\boldsymbol{\varphi: response\ delay}$$

The significance of each voxel was determined by ranking its signal against a null distribution generated using a non-parametric permutation of 1000 iterations, reordering stimulus, and rest blocks for each iteration. I created a customized region-of-interest (ROI) to cover the brainstem in the MNI152 space described in Figure 2.1 (b). Vestibular nuclei are located inferior and lateral to the 4th ventricle while reticular formation (RF) is superior to the pontomedullary junction and surrounds the neuraxis [54]. I chose the entire VN instead of LVN due to the small size of the LVN. Voxels were filtered with an uncorrected significance level of $p \leq 0.05$. Additionally, I analyzed the whole brainstem response after excluding the corticospinal tract located anterior of the pons to inspect the overall response of the brainstem. The common coverage of the brainstem available in all subjects is described in Figure 2.3, which includes the whole VN but likely does not encompass the entire RF. Brainstem volume was using automatic segmentation with FreeSurfer [55].

My main outcome measures were: 1) number of significantly activated voxels forming a connected structure within each ROI (nVox); 2) mean strength of activity on each side of the brainstem (% change), and 3) mean phase of the response (rad) representing the time delay of the fMRI response to the stimuli. Model was designed to represent the response to the block-design stimuli as a sinusoid at 1/30 Hz. I ran a bootstrap analysis to provide a null distribution observed across our data in each stimulus. Within-subject comparisons between the two stimuli were made using a paired t-test ($\alpha < 0.05$). Additional covariates were examined using a linear regression model. Our linear regression model contained dependent variables of activity strength (number of voxels) and average response amplitude, and with covariates of age and brainstem volume in each subject's native space.

2.4 RESULTS

Over the whole brainstem, I observed 3,576 mm^3 activated voxels, 0.66% change in mean response, and a 3.5 rad mean delay. In the VN, found an average of 22.3 mm^3 of activation with a mean amplitude 0.32%. In the RF, 14.9 activated voxels had on average 0.24% amplitude. Results are summarized in Table 2.1 and the group response is visualized in Figure 2.3. In two of the younger subjects, I observed bimodal phase distributions (Figure 2.4). The average motion/TR across the subjects was 0.47 ± 0.17 mm.

Over the whole brainstem, I observed 3,106 mm^3 activations and 0.79%

amplitude. In the VN, I found 46.8 mm^3 activations with 0.30% amplitude. In the RF, I had 10.6 mm^3 activations and 0.19% amplitude. Results are summarized in Table 2.2 and visualized in Figure 2.3. Again, bimodal phase distributions were observed in the younger subjects. The average motion/TR was 0.39 ± 0.18 mm. I compared between stimulus on measurements on 9 subjects with paired Wilcoxon-rank sum test. I found no significant differences in the type of stimulus in any ROIs or subjects (Table 2.3).

Finally, I built a model to explain the measured variables by two factors: subject age and brainstem volume. I validated a fixed-effect linear model with the low number of samples collected. The results follow that the number of voxels activated in RF during the optokinetic stimuli was both significantly correlated with age and brainstem volume. ($p = 0.0029, 0.00049$ respectively with R-squared 0.801) However, there were no significant correlations for the ASR stimulus.

TABLE 2-1. MEASUREMENTS FOR OPTOKINETIC STIMULUS (CI 95%)

Stats	ROI	Both	Left	Right
nVox (mm^3)	Bstem	3576.3 [1498.4, 6298.2]	1780.8 [800.7, 3124.0]	1795.6 [703.6, 3161.3]
	VN	22.3 [12.0, 32.0]	11.6 [3.0, 22.4]	10.8 [4.8, 17.8]
	RF	14.9 [1.8, 35.3]	2.6 [1.0, 4.4]	12.3 [0.4, 31.8]
Avg Response (% change)	Bstem	0.66 [0.53, 0.84]	0.65 [0.51, 0.84]	0.67 [0.53, 0.85]
	VN	0.32 [0.19, 0.45]	0.24 [0.08, 0.40]	0.28 [0.16, 0.39]
	RF	0.24 [0.12, 0.34]	0.24 [0.12, 0.35]	0.16 [0.05, 0.28]
Avg phase delay (rad)	Bstem	3.54 [2.82, 4.08]	3.52 [2.83, 4.07]	3.56 [2.90, 4.09]
	VN	3.38 [1.78, 4.68]	2.62 [1.00, 4.24]	3.51 [1.86, 5.02]
	RF	2.59 [1.33, 4.02]	2.96 [1.38, 4.45]	1.46 [0.07, 2.86]

TABLE 2-2. MEASUREMENTS FOR ACOUSTIC STIMULUS (CI 95%)

Stats	ROI	Both	Left	Right
nVox (mm^3)	Bstem	3106.6 [1710.8, 4852.3]	1532.9 [895.6, 2357.4]	1573.7 [870.1, 2490.8]
	VN	46.8 [20.2, 76.8]	24.6 [4.3, 53.5]	22.2 [8.8, 39.2]
	RF	10.6 [1.7, 23.1]	9.0 [0.0, 24.2]	1.6 [0.2, 3.3]
Avg Response (% change)	Bstem	0.79 [0.57, 1.03]	0.72 [0.54, 0.92]	0.86 [0.61, 1.13]
	VN	0.30 [0.17, 0.45]	0.28 [0.12, 0.45]	0.25 [0.16, 0.34]
	RF	0.19 [0.10, 0.29]	0.10 [0.00, 0.21]	0.09 [0.03, 0.19]
Avg phase delay (rad)	Bstem	3.21 [2.72, 3.72]	3.18 [2.62, 3.72]	3.24 [2.69, 3.73]
	VN	2.62 [1.35, 3.79]	2.30 [1.05, 3.77]	2.33 [1.09, 3.58]
	RF	2.16 [0.89, 3.41]	1.03 [0.16, 2.20]	1.13 [0.00, 2.52]

TABLE 2-3. NONPARAMETRIC P-VALUES OF OPTOKINETIC VS ASR

Stats	ROI	Both	Left	Right
nVox (mm^3)	Bstem	0.910	1.000	0.910
	VN	0.359	0.734	0.250
	RF	0.742	0.938	0.742
Avg Response (% change)	Bstem	0.496	0.820	0.359
	VN	0.734	0.734	0.570
	RF	0.547	0.109	0.547
Avg phase delay (sec)	Bstem	0.203	0.164	0.359
	VN	0.570	0.820	0.652
	RF	0.742	0.109	0.625

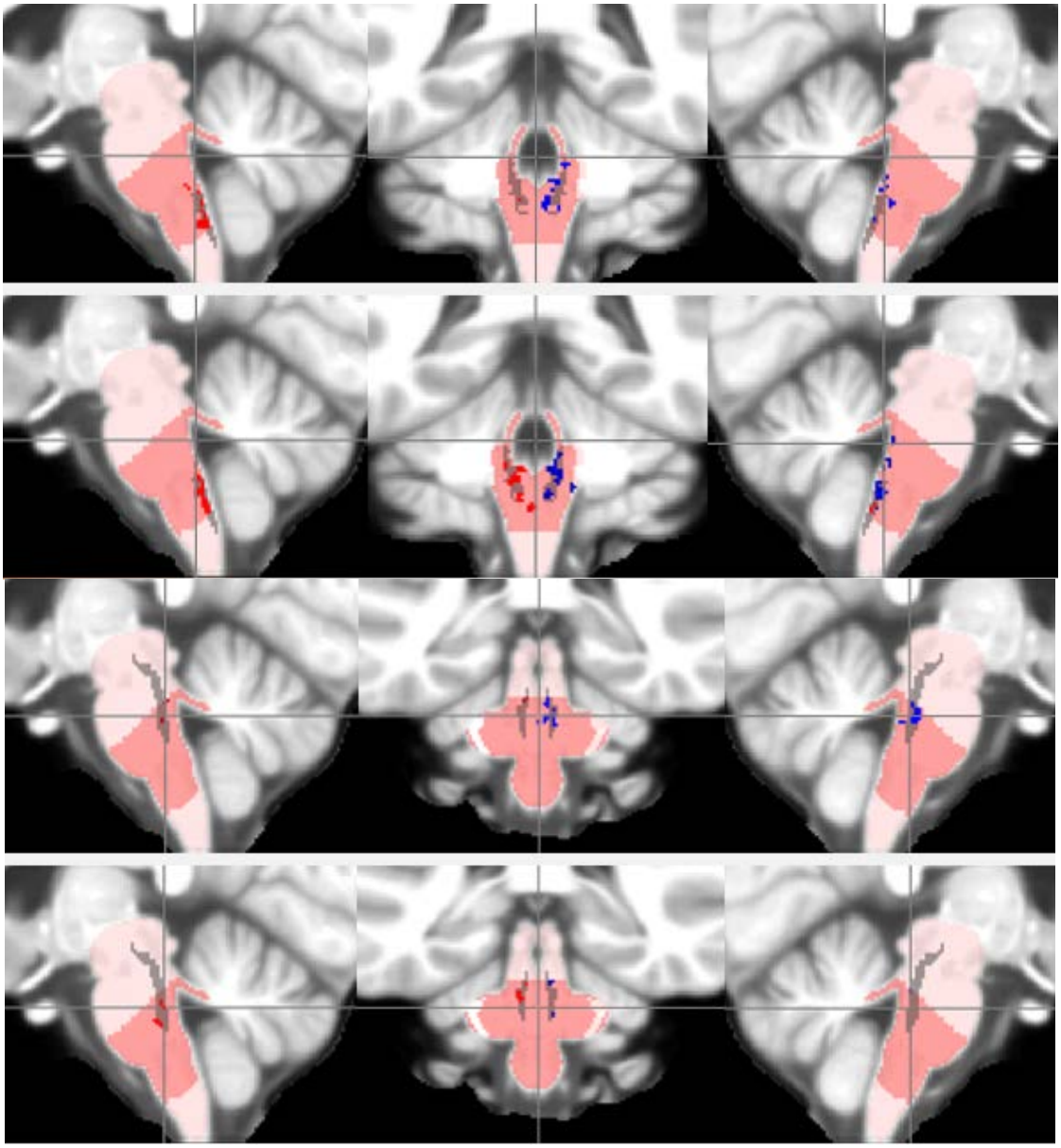

Figure 2.3. The common coverage within the brainstem is in dark red. The average response of all subjects within condition is represented from 1st row (vestibular network with vection stimuli), 2nd (vestibular network with acoustic stimuli), 3rd row (reticular formation with vection stimuli), and 4th (reticular formation with acoustic stimuli). In each brainstem, red represents left side response and blue represents right side response.

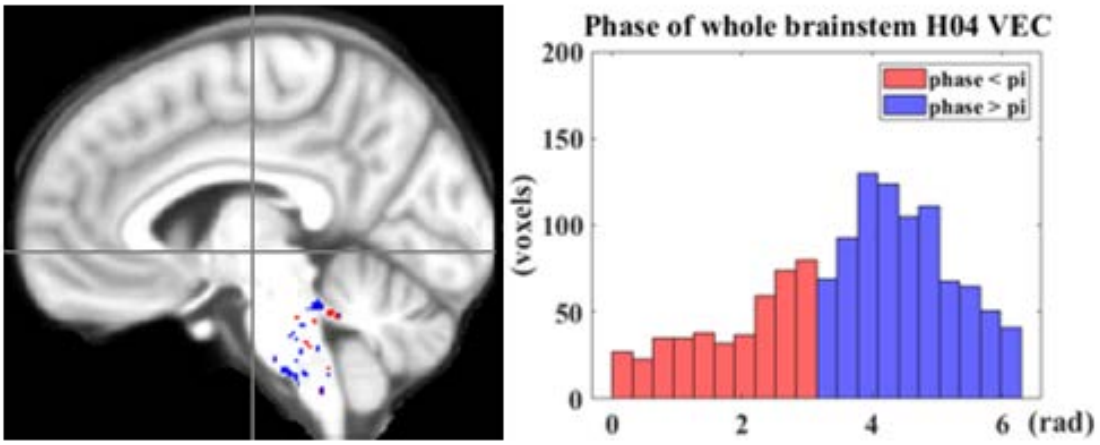

(a)

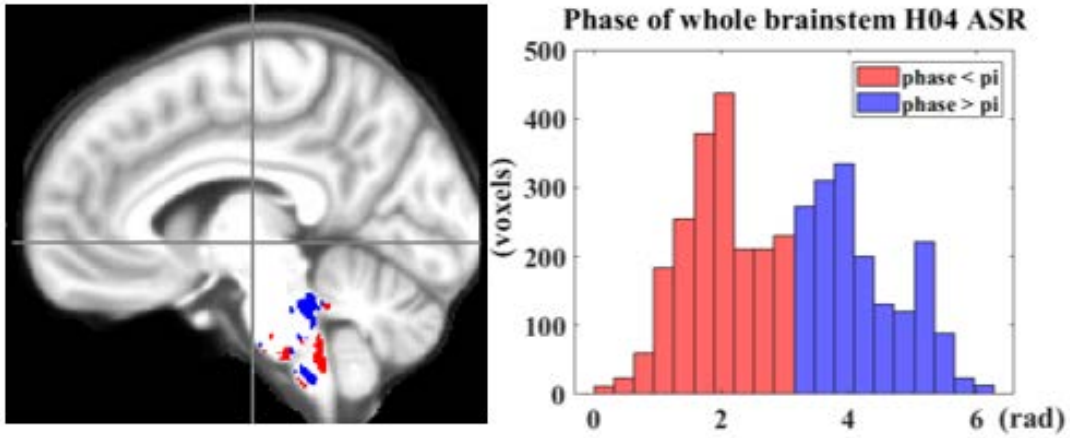

(b)

Figure 2.4. This is an example of a subject's (H04) response to both stimuli across the whole brainstem region. (a) Vection stimuli (b) Acoustic stimuli. The phase distribution of the activated voxels is represented in two colors. Red represents the response phase less than 3.14 rad, where we would take it is following the stimulus design and blue represents the phase over 3.14 rad, anti-correlated to the response. The proximity of voxel correlated and anti-correlated provides potential difficulty in terms of the average signal response.

2.5 DISCUSSION

When exposed to vection and acoustic-startle stimuli, I expected significant localized response in both VN and RF. I did not find any significant voxels activated after performing standard analysis via SPM, because the multiple-comparison correction eliminated all effects. I believe this correction is too conservative for use in brainstem at high resolution I therefore report uncorrected statistical analysis to investigate the trend of the response toward the different type of stimulus. I hypothesized that the VN and RF would respond distinctly to optokinetic and acoustic stimuli, respectively. Wildenburg et al (2011) [49] reported localization of a single voxel in the expected vicinity of the lateral vestibular nuclei activated by optokinetic stimuli on 9 healthy subjects. I was unable to replicate these results. I also found that pontine response varied with age, suggesting an additional factor in conducting brainstem imaging research. These data provide helpful preliminary evidence in functional differentiation of brainstem nuclei.

Our inability to replicate the Wildenberg result was most likely caused our inclusion of many older individuals, which reduced the strength of response given the correlations of brainstem response and age in Table IV. However, younger subjects gave robust activations that could be clinically useful, but our subject population was very small. Thus, more experiments are needed to validate the ability to routinely localize VN using fMRI.

Variability in the registration step was indeed a serious challenge. Regardless of the high resolution of the fMRI scans, the anatomical boundaries within the brainstem

differentiating the nuclei are difficult to discern using most MRI contrasts, particularly at 3T. The boundaries of specific nuclei are not evident from the T1-MPRAGE anatomical scans. I used the MNI-space defined atlas [54] to estimate the positioning of the nuclei, and qualitatively inspected the standard space registration. Generally, registration was imperfect, based on misalignments observed at clear boundaries such as the superficial surfaces of the superior and inferior colliculi. The combination of misalignment and the lack of a clear definition of nuclei boundaries weakens to identify the response clearly.

It may be that our across-subjects analysis was foiled because activations and deactivations occur in proximity among the tightly packed nuclei of the brainstem presented in Figure 2.4. This hypothesis is supported by the bimodal phase distributions observed in the younger subjects. Therefore, when multiple subjects are registered together using available, rather approximate methods, all effects tend to cancel out.

Head movement during the scan is a critical parameter to control for the fMRI experiment. Mean displacement across all scans and subjects was small, <0.5 mm after motion censoring. However, for vection, there was a correlation between age and head motion ($r = 0.53$, $p = 0.12$), but this correlation was not observed for the ASR. Nevertheless, head motion may have degraded the quality of the fMRI data for the older, naïve subjects, partly explaining the observed trends with age. I also suspect that our motion censoring threshold was too lenient, but the small subject population gave us little latitude in the censoring.

Finally, the experimental design to achieve a reliable response was difficult

because the VN and RF fMRI response effect sizes were not known in advance. In order to control the quality of the runs, simultaneous efferent measurement (e.g., eye tracker for visual, muscle activity measures for acoustic stimuli) would provide the quantitative behavior assessment to evaluate the fMRI for quality control. Increasing the number of participants should increase the statistical power, with a greater focus on younger subjects that yield stronger activations. In addition, older and naïve subjects must be more carefully trained with better head restraints to reduce head motion.

2.6 CONCLUSION & FUTURE WORK

I investigated the brainstem neural response via fMRI to characterize the effect of visual/acoustic stimuli. I was unable to replicate results found in an earlier study localizing LVN. The responses in brainstem nuclei were only detectable using uncorrected statistics, suggesting that more sensitive protocols aimed at younger or better-trained subjects are required to reliably quantify functional brainstem activity.

[2]CHAPTER 3

Brainstem BOLD response to visual and acoustic stimuli in people with post-stroke spasticity

3.1 INTRODUCTION

Spasticity is a disorder of the sensorimotor system characterized by a velocity dependent increase in tonic stretch reflexes ('muscle tone') with exaggerated tendon jerks as one component of the upper motor neuron syndrome [44]. Spasticity is known to affect activities of daily living [56], for example, our group has observed a link between spasticity and post-stroke stiff-knee gait [57,58]. While underlying mechanisms of spasticity remain poorly understood, it is accepted that spasticity results from hyper-excitability of the stretch reflex [59,60]. It is unclear specifically which dysfunctional brainstem nuclei are primarily responsible for hyperreflexia. Miller et al. stimulated stroke survivors with acoustic startle bursts (ASB), random sequences of brief loud tones while measuring electromyographic (EMG) activity in the sternocleidomastoid muscle as an indirect measure of neural activity in lateral vestibular nuclei (LVN) [46]. They found that the level of asymmetry of the response to the acoustic startle burst was correlated to clinical measures of spasticity, which are reflective of hyperreflexia. However, it is also possible that the acoustic startle bursts may have activated the medial

[2] Han, C., Ress, D., Nuñez, A.I.R., de la Rosa, N., Li, S. and Sulzer, J.S., 2020. Brainstem BOLD response to visual and acoustic stimuli in people with post-stroke spasticity. In 2020 8th IEEE RAS/EMBS International Conference for Biomedical Robotics and Biomechatronics (BioRob) (pp. 872-877). IEEE.

reticulospinal tract (mRST) creating activity within the pontine reticular formation (PRF) [61]. Resolving this debate could use functional neuroimaging of the LVN and PRF.

Functional magnetic resonance imaging (fMRI), with whole brain coverage and millimeter resolution, is likely the best option for functional brainstem imaging [62]. However, there are very few attempts, possibly due to significant challenges [48], such as a complex vascular structure and small size of the nuclei, making it more vulnerable than the rest of the brain to physiological artifacts such as heart rate and respiration. Spatial and temporal linearity of fMRI responses in brainstem have not yet been evaluated. Some evidence suggests that functional brainstem activity in LVN can be measured. Wildenberg et al. (2011) [49], used visual stimuli in the form of an optokinetic black-and-white checkerboard, a concept known as vection [50], to induce the sensation of self-motion. They observed a single $2mm^3$ voxel of activity in the LVN after multiple comparison corrections. While clearly more robust evidence is needed for functional LVN and PRF imaging, the aim of this work was to use these techniques to probe the spastic post-stroke brain.

I conducted experiments to contrast functional activation in LVN and PRF using 3T fMRI in chronic, spastic stroke participants compared to age-matched healthy controls, whose response is detailed in a companion paper [62]. I employed two stimuli: optokinetic vection, which should activate LVN, and ASB hypothesized to excite both LVN and PRF. I expected to find a greater bilateral asymmetry of response in brainstem nuclei of post-stroke individuals to both stimuli reflecting the supposed pathologic disinhibition asymmetry. I used a scanning sequence optimized for subcortical imaging

[62] of small structures and a simple-blocked alternation stimulus with 30 s period to avoid physiological confounds, which occur at much higher temporal frequencies [64]. Our goal is to resolve a long-standing debate regarding which brainstem nuclei are primarily involved in spasticity, leading towards improved, targeted neural interventions.

3.2 STUDY DESIGN

I recruited 10 chronic stroke individuals (mean age: 58.3 ± 10.9 years, 7 males) recruited by physician co-author (SL) at TIRR Memorial Hermann in Houston, TX. In parallel, 11 neurologically intact participants were also recruited (mean age: 46.3 ± 14.4 years, 4 males). After obtaining informed consent following procedures authorized by the University of Texas at Austin Institutional Review Board, participants underwent two sessions of fMRI scanning. All experienced the visual vection stimuli. Two healthy individuals and two post-stroke individuals did not continue with the ASB stimulus session, limiting data to nine healthy (mean age 48.5±13.2 years, 3 males) and eight post-stroke individuals (mean age 56.7±11.3 years, 2 males).

All subjects had a normal or corrected-to-normal vision. Stroke participants had the following inclusion criteria: age 21-75 years, ability to provide informed consent, chronic hemiparesis from a stroke, spasticity in wrist flexors (Modified Ashworth scale (MAS) of 1, 1+, 2 and 3), able to remain in the scanner for 45 mins. The stroke participants were 5.3 ± 2.4 years post-stroke and assessed a mean 1.15 ± 0.63 MAS score at the elbow.

I used a two-dimensional moving checkerboard (Figure 3.1) to elicit vection (a feeling of self-motion) as a means to evoke LVN activity [15]. ASB designed to elicit

acoustic startle reflex was based on previous work [7]. The bursts were played through a binaural headset (SPL = 100 dB, 1 kHz single frequency, 50 ms duration) at pseudorandom time points with a minimum inter-tone interval of 1s. I applied these stimuli to the same individual in fMRI scanning sessions on different days, with a counterbalanced order of conditions. During both experiments, I collected a structural volume by running a T1 MPRAGE sequence (TI = 900 ms, TR = 2600 ms, flip angle 9°, 1-mm cubic voxels) using a 3T Siemens scanner with a 32 channel head coil. Functional images were obtained using a T2*-weighted spiral-acquisition sequence with TR/TE of 0.75/38ms, 2 interleaves, and voxel resolution of 1.5 mm^3 [62]. An illustration of the stimuli and coverage is shown in Figure 3.1 (a). Each block was composed of 15 seconds of stimulation followed by 15 seconds of rest. Figure 3.1 (a) illustrates the protocols for both experiments.

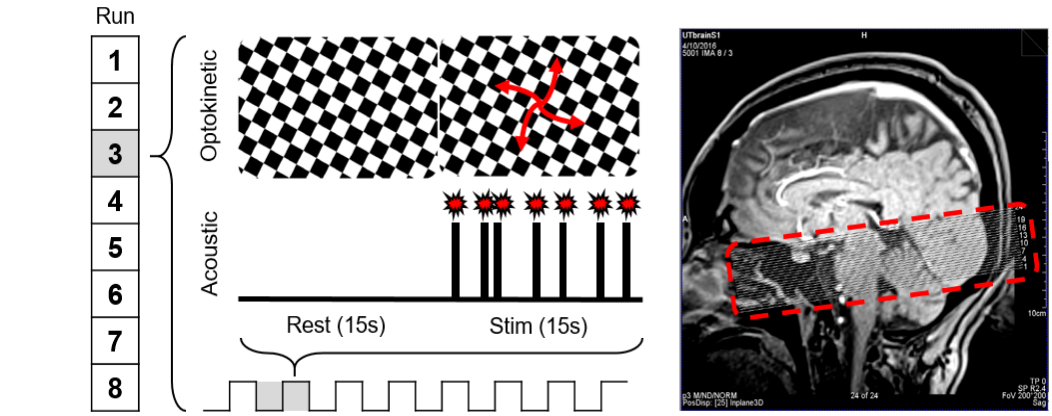

(a)

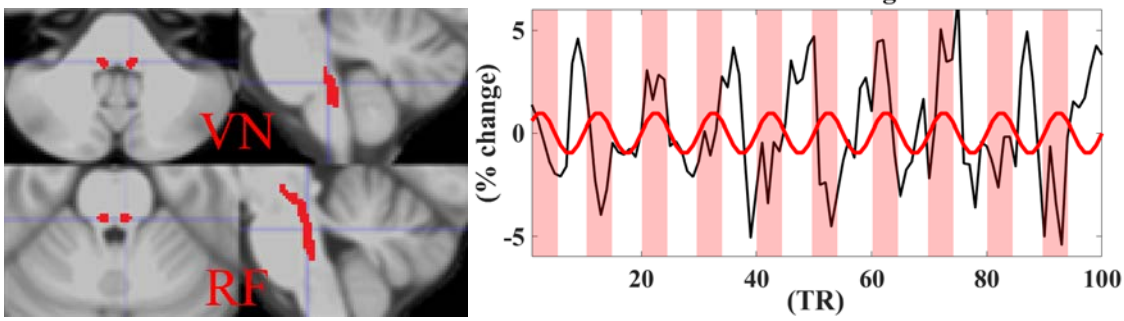

(b) (c)

Figure 3.1. Experimental design –(a) the acoustic burst/visual optokinetic stimuli are presented during the Stim block (15 seconds) and Rest block (15 seconds) with slice orientation and limited FOV during fMRI scanning. (b) The vestibular network (VN) (top) and reticular formation (RF) (bottom) were qualitatively masked in the MNI152 space. (c) Representative data showing hemodynamic response (black curve) to the blocked alternation (pink & white bars) and best-fit sinusoid (red curve).

3.3 DATA ANALYSIS

I performed preprocessing including slice timing correction, movement correction within each run and between runs, registration to each subject's own native space, and then

co-registered to MNI152 standard space using the volume-based Advanced Normalization Tools (ANTs) resliced by FreeSurfer [53]. I also discarded runs that exhibited >0.75mm/TR motion. I did not apply Gaussian spatial smoothing due to the small size of the brainstem nuclei of interest. In order to determine voxel-wise significance, I calculated the ranking of each voxel against a null distribution generated using a non-parametric permutation of 1000 iterations, reordering stimulus, and rest blocks for each iteration. Voxels were filtered with an uncorrected significance level of $p < 0.05$. I targeted our slice prescription to cover appropriate portions of the brainstem (Figure 3.1 (a)). Within the imaged brainstem, I defined two regions of interest (ROIs); see Figure 3.1 (b). ROI masks were created using FSL manually by visual inspection based on atlas results [54, 66]. The estimated reticular formation ROI (RN) primarily covered the PRF. The second vestibular ROI covered the whole vestibular network (VN) due to the small size of the LVN. The VN was located inferior to the pontomedullary junction and lateral to the 4th ventricle while RF was chosen more superior to the pontomedullary junction and medially close to the center of the brainstem. Additionally, I quantified the overall response of the imaged brainstem after excluding the corticospinal tract located in the anterior half of the pons. The common coverage of the brainstem available in all subjects is shown in Figure 3.2 (a), which includes the whole VN but likely does not encompass the entire RF. I segmented the brainstem volume in the native space using FreeSurfer [53]. For the stroke participants, I separated the ROIs into ipsi- and contra-lesional sides for comparison.

I modeled the block design as a sinusoidal input at 1/30 Hz and then analyzed the hemodynamic responses as a best-fit sinusoid at the same frequency [coherence analysis; Figure 3.1 (c)]. My main outcome measures were the 1) number of significantly activated voxels forming a connected structure within the ROI, 2) mean amplitude of the sinusoidal fit (% change), and 3) mean phase of the fit (rad) representing the delay of the

hemodynamic response to the stimuli. I ran a bootstrap analysis to provide a null distribution observed across our data in each stimulus. Within-subject comparisons between the two stimuli were made using a paired t-test ($\alpha < 0.05$). I chose to apply summary statistics within each ROI instead of voxel-based comparisons because of the large variability across subjects within each condition.

Finally, I examined additional covariates using a linear regression model. My linear regression model contained dependent variables of activity strength (number of voxels) and average response amplitude and with covariates of age and brainstem volume directly segmented from the original T1-weighted anatomical scan before co-registration to the standard space.

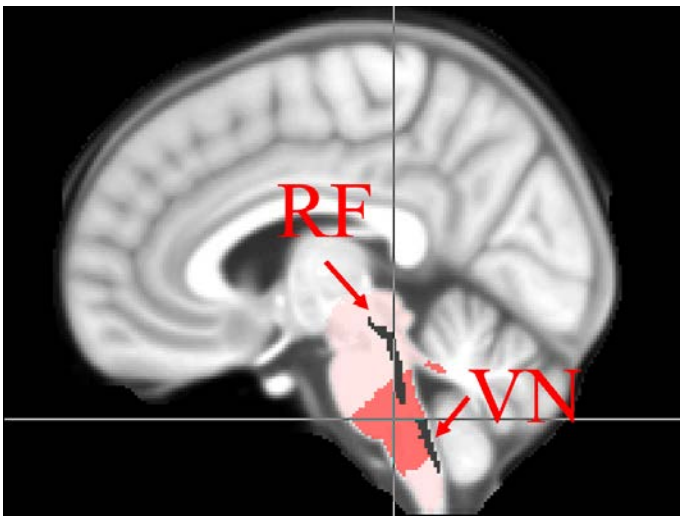

(a)

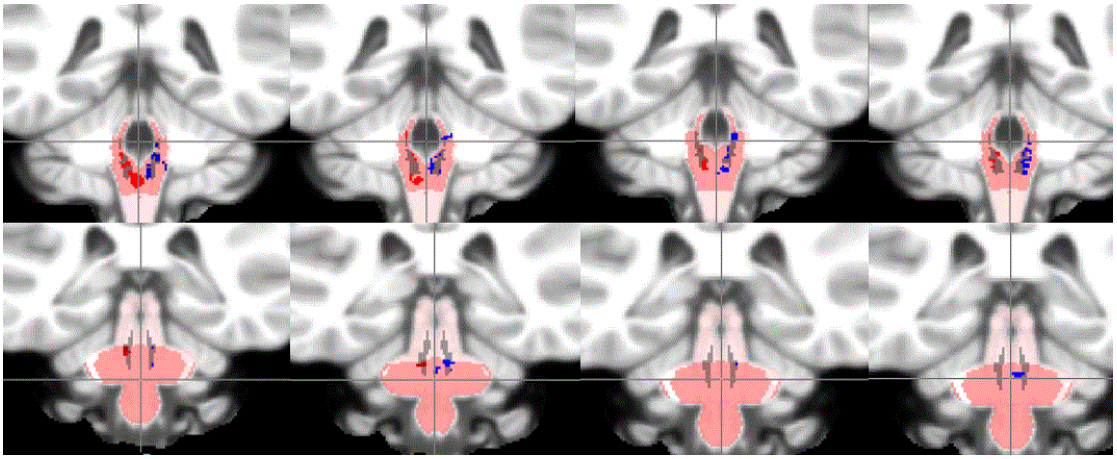

(b)

Figure 3.2. (a) Brainstem (light red), common coverage across all subjects (dark red), and ROIs (RF & VN, black). (b) Average response of all subjects in the MNI space of VN (top row) from left, healthy acoustic, healthy vection, stroke acoustic and stroke vection. Reticular formation in the bottom row in same order of conditions.

3.4 RESULTS

Vection evoked substantial activation volumes, >3,000 mm^3 in the imaged-brainstem ROI (Figure 3.3) for both the healthy and post-stroke groups. Mean response amplitudes were ~0.7%, and mean phase delays in the responses were fairly close to 3.14 rad, suggesting a balance of excitation and inhibition. There were no significant differences between the two groups. In the VN, for healthy much smaller activation volumes were evoked by both stimuli, 22.3 mm^3 on average, with 0.32% mean amplitude and 3.4 rad mean delay and 19.0 mm^3, 0.17%, 1.6 rad respectively in post-stroke individuals. The smaller phase delay is suggestive of more selective activation in VN, but the difference between groups was not significant ($p = 0.079$). In the RF, I observed similar results: for healthy, I found 14.9 mm^3 volume, 0.24% change, and 2.6 rad mean delay and 3.4 mm^3, 0.10%, and 0.73 rad respectively in the post-stroke group. The average voxel-response distribution is shown in Figure 3.2 (b); red represents the left/ipsilesional side, and blue represents the right/contralesional side for each population.

Over the imaged brainstem, activations were similar to those evoked by vection. In the VN, the healthy group had a larger activated volume than for vection, 46.8 mm^3. Average amplitudes and phase shifts were similar to those evoked by vection. The post-stroke group had a non-significant trend toward lower activation volume, 21.6 mm^3 ($p = 0.36$), 0.61%, 1.8 rad respectively in post-stroke individuals. In the RF, I had 4.6 mm^3, 0.14% change and 2.1 rad mean delay, and 0.8 mm^3, 0.08%, 1.1 rad respectively in post-stroke individuals. The average response spatial distribution is presented in Figure 3.2 (b).

I compared observables between stimuli on measurements within the same group with a paired Wilcoxon-rank sum test. Most comparisons between the stimuli were not significant ($p > 0.05$). However, I found that the post-stroke group responded to the vection

stimuli significantly slower than acoustic stimuli across the whole brainstem region ($p = 0.008$), and significantly slower than in healthy individuals ($p = 0.079$). Interestingly, I found the opposite relation when localized to the VN: post-stroke individuals responded slower than healthy individuals ($p = 0.048$). I also observed a trend for the acoustic stimuli to evoke a stronger response in VN than vection ($p = 0.47$). The summary statistics I took from the ROI across the whole brainstem are presented in Figure 3.3.

I hypothesized that response laterality should correlate with the level of spastic response in stroke participants. I compared the left and right in healthy participants to quantify healthy asymmetry and ipsilesional vs. contralesional in the stroke population. However, I did not find any significant lateralization differences in either of the groups for both stimulus conditions described in Figure 3.4.

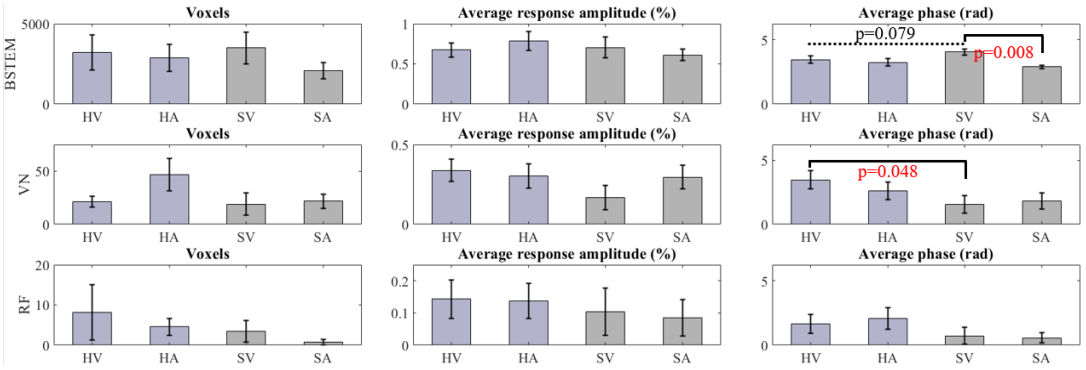

Figure 3.3. Results of the response in all conditions. Participants are labeled as HV (Healthy Vection), HA (Healthy Acoustic), SV (Stroke Vection) and SA (Stroke Acoustic).

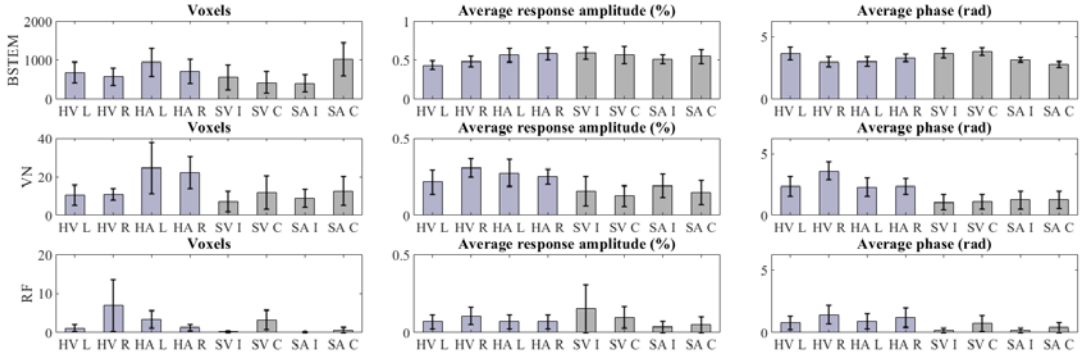

Figure 3.4. Comparison of left/right in the healthy group and ipsilesional /contralesional in the stroke group. We did not find any significant lateralization differences in any condition. Annotation L/R stands for left/right and I/C stands for ipsilesional/ contralesional

I built linear models to test if experimental observables could be explained by participant age and the brainstem volume; three significant relationships were observed. (I employed a fixed-effects linear model instead of a mixed-effects model due to the low number of participants.) First, age and brainstem volume predicted the activation volume in RF-induced by the vection stimulus ($R^2 = 0.73$, $p = 0.01$) for healthy participants (Figure 3.5 (a)). Second, in the post-stroke group, the activation volume across the imaged brainstem ROI evoked by the vection stimulus had a strong correlation ($R^2 = 0.92$, $p = 0.02$) with age, duration, arm MAS and brainstem volume; see Figure 5 (b). Third, the same group showed a strong correlation ($R^2 = 0.89$, $p = 0.037$) between VN activation volume and the same combination of variables (Figure 3.5 (c)). I observed that the post-stroke individuals' average brainstem volumes (mean 23.7 ± 2.4 cm^3) were significantly smaller than the controls (mean 26.3 ± 1.9 cm^3) (two-sample rank-sum test, $p = 0.027$). None of the post-stroke individuals had significant traumatic volume loss in the subcortical area as a direct consequence of their stroke.

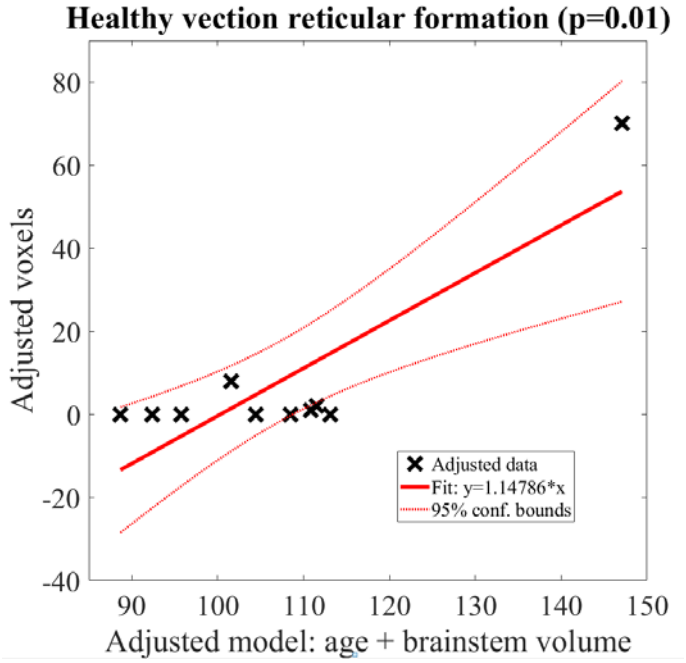
Healthy vection reticular formation (p=0.01)
Adjusted voxels
80
60
40
20
0
-20
-40
90
100
110
120
130
140
150
Adjusted model: age + brainstem volume
Adjusted data
Fit: y=1.14786*x
95% conf. bounds

(a)

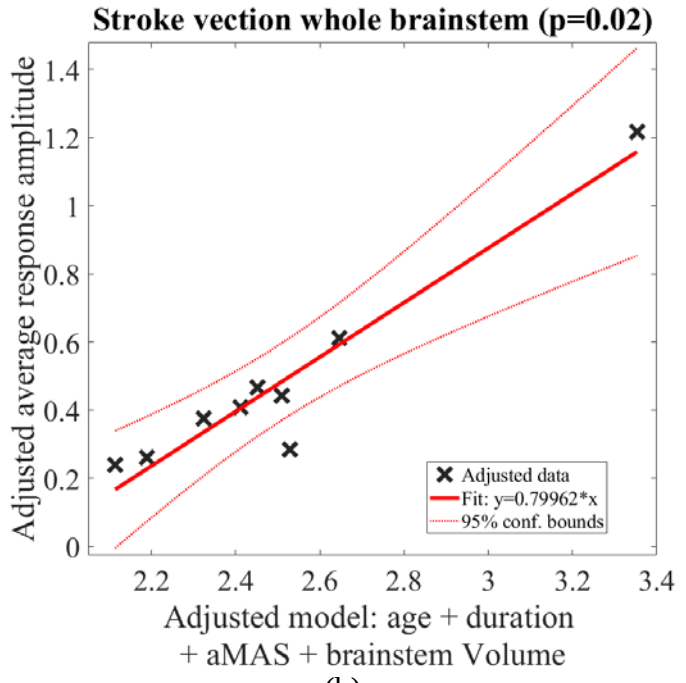
Stroke vection whole brainstem (p=0.02)
Adjusted average response amplitude
1.4
1.2
1
0.8
0.6
0.4
0.2
0
2.2
2.4
2.6
2.8
3
3.2
3.4
Adjusted model: age + duration
+ aMAS + brainstem Volume
Adjusted data
Fit: y=0.79962*x
95% conf. bounds

(b)

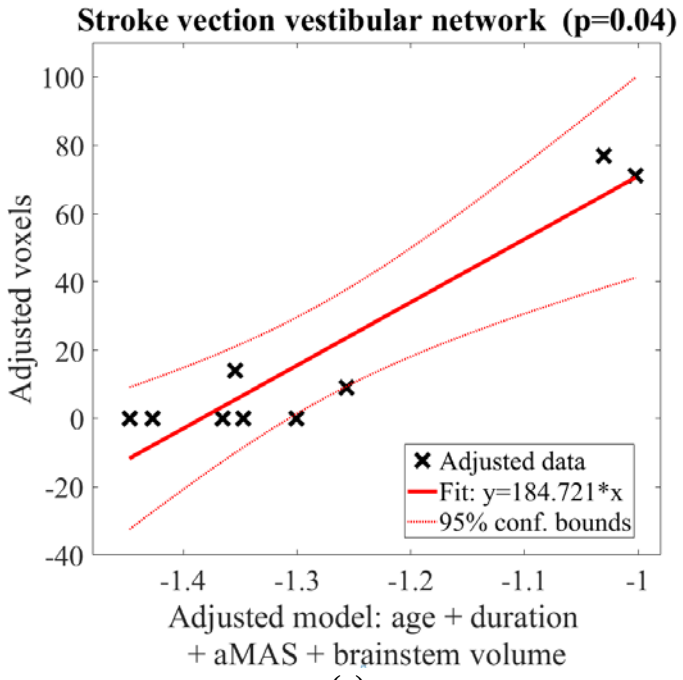

(c)

(a)	$Volume\ (mm^3)$	$= -115.15 - 1.15\ age + 0.007\ Brainstem\ Volume$
(b)	$Avg\ amplitude$	$= \quad -1.52 - 0.01\ age - 0.011\ duration\ + \quad 0.79\ aMAS\ +$ $0.0001\ Brainstem\ volume$
(c)	$Volume\ (mm^3)$	$= \quad 255.69 - 0.88\ age + 10.42\ duration\ - 184.42\ aMAS\ -$ $0.0079\ Brainstem\ volume$

Figure 3.5. Regression models relating observables. Note slopes are shown for each model. (a) Activation volume vs. age and brainstem volume in healthy participants. (b) Response amplitude vs. the combination of age, duration of stroke, arm MAS score and brainstem volume. In stroke participants with the vection stimuli. (c) Activation volume evoked by vection in the VN vs. the same variables for the stroke participants

3.5 DISCUSSION

I examined brainstem correlates of spasticity in VN and RF by applying both visual and acoustic stimuli to a group of spastic post-stroke individuals and healthy control subjects. I did not find evidence of asymmetry in these brainstem nuclei as expected. However, I found differences in a delay to stimuli, age and brainstem volume predictors of the response, and difference in brainstem size between age-matched controls and post-stroke individuals. These results offer a preliminary view into the potential diagnostic utility of functional brainstem imaging after stroke.

I observed differences in hemodynamic response delay between healthy and post-stroke individuals in the VN and the brainstem. In the VN, there was a greater delay between acoustic and visual stimuli in post-stroke individuals, whereas, in the brainstem, this relation was reversed. There were no significant left-right differences in healthy individuals. In post-stroke individuals, there was a greater delay to acoustic compared to visual stimuli. While differences in hemodynamics after stroke were expected, the differential effect of stimuli is a new finding. It could reflect temporal processing differences for visual compared to auditory stimuli. Visual processing occurs first in the thalamus, then in the cortex. Auditory processing, by contrast, occurs first in brainstem nuclei, and the slower hemodynamic responses could be reflective of pathology related to stroke-induced spasticity. On the other hand, the ASB stimuli were not delivered promptly, but rather included a small delay, which could at least partly explain this finding. Further experiments will be necessary to fully understand this observation.

There is evidence of midbrain volume loss with healthy aging [68], and our findings show a similar result across the whole of brainstem. Further, post-stroke individuals

exhibited smaller brainstems than their age-matched counterparts, suggesting possible neurodegeneration.

The linear correlations also highlight interesting relationships. First, activation volumes in the VN of healthy subjects may drop with increasing age, suggesting that brainstem imaging studies in older individuals will be more difficult than in a younger population. However, this trend is mostly based on a single subject, weakening its reliability. Second, brainstem activation amplitude decreased with age, duration since the stroke, and brainstem size in the stroke group. To some extent, this finding explains the weakness of our results: older and more afflicted post-stroke participants showed weaker activations. Third, VN activation volume decreases with age and MAS. This observation is consistent with spasticity-associated hyperactivity in the VN; tonic firing reduces the ability of the vection stimuli to evoke activation. However, this trend was apparently offset by duration and brainstem volume, perhaps suggesting partial recovery over time. It must be noted, however, that the small group size in our study weakens all of our findings. More experiments with larger populations will be necessary to corroborate these observations.

3.6 CONCLUSION & FUTURE WORK

I aimed to isolate and stably localize specific nuclei to identify the true source of spasticity in relation to the motor descending pathways, but results were insufficiently reliable to draw firm conclusions. Several factors could explain the low reliability. First, our movement per TR threshold of 0.75mm was too lenient; many of the naïve subjects showed repeated motion artifacts. Second, due to the difficulties of recruiting chronic

stroke patients, I did not balance the gender for this experiment. There is evidence to suggest gender may affect the response amplitude; this may be incorporated in the future experiment design [69]. Lastly, it is commonly known that the upper-limb movement involves handedness and is shown to modulate the vestibular-ocular reflex [70]. However, it remains an open question if handedness affects subcortical activation [71]. I primarily recruited age-matched participants mostly from associates of the stroke patients. I did not collect the handedness of healthy cohorts because I did not anticipate this factor would become primary without any explicit movement execution inside the scanner. This should be remediated in future work.

While my primary hypothesis of an asymmetric brainstem response to specific stimuli could not be verified, I observed anatomical and functional phenomena of the brainstem that will inform future work. Developing a better understanding of the role of the brainstem in impairment will help improve diagnoses and enable targeted interventions.

[3]CHAPTER 4

An MRI-Compatible Force Sensor for Measuring Differential Isometric Precision Grip Force

4.1 INTRODUCTION

Fine motor control such as precision grip is most acutely developed in humans. Precision grip control is highly influenced by monosynaptic connections from the motor cortex [72]. Studies using functional magnetic resonance imaging (fMRI) have provided a wealth of information about neural correlates of precision grip. For instance, the cortical activity in sensorimotor cortical areas increases linearly with the force of grip [73]. However, dexterous, small force conditions may involve higher activation in premotor areas [74] and bilateral motor cortex, implying that fine control involves more complex neural circuitry including co-activation of antagonist muscles [75]. Subcortically, basal ganglia modulate the amplitude, rate, motor planning, and selection [76]. All of these previous studies have examined precision grip as a combined isometric contraction. However, the relative roles of the forefinger and thumb in precision grip control are unknown. The forefinger and thumb are most often synergistic but are not locked together. For instance, buttoning a shirt requires differential control of the forefinger and thumb. It has been shown that this differential control task is an important

[3] Han, C., Oblak, E., Abraham, L., Ferrari, P., McManis, M., Schnyer, D. and Sulzer, J., 2017, July. An MRI-compatible force sensor for measuring differential isometric precision grip force. In 2017 39th Annual International Conference of the IEEE Engineering in Medicine and Biology Society (EMBC) (pp. 791-794). IEEE.

biomarker of impairment in the elderly [77,78] and those with Parkinson's disease [79]. Yet this diagnostic test is not compatible with a magnetic environment.

Current methods of measuring precision grip force in the MR environment use a single force sensor incapable of delineating forefinger and thumb forces independently [74, 80-85]. I aim to design and characterize a force sensor that measures individual finger and thumb forces while performing complex precision grip motor tasks. Here I present the core design aims, specifications of transducer, material, manufacturing, and simulation results. I empirically characterize the sensor in terms of identifying linearity, hysteresis, and force bandwidth.

4.2 DESIGN

The task assigned in a neuroimaging study is to measure the force of two fingers (thumb and index) while performing an isometric pinch in real-time. Thus, the core specifications of the sensor I aimed to design for our application are as follows:

- Maximum force of 20N in each finger
- Resolution of 0.1N in each finger
- MR compatibility
- Ergonomically designed to fit precision grip posture

My design uses a flexure with an optic fiber to transduce the deflection of the flexure to a voltage, as used in previous designs [9,10,12-15]. The key difference is that the sensor is grounded between the two fingers, allowing independent measurements of

forefinger and thumb forces. Thus, here I describe how the flexure transmits displacement at the fingers to a voltage.

The force is indirectly measured by the fiber optic sensor. The flexure is grounded in the center, with an inclined double parallel mechanism on both sides and optic fibers aligned to measure deformation (Figure 4.1 (a)). The flexure is grounded by firmly positioning it to the aluminum-mounting base with brass bolts and nuts. When force is applied on either side, the deformation of the parallelogram shifts vertically, moving a mirror further away from the fiber optic head, therefore the intensity of the reflected laser decreases, resulting in a change in sensed displacement. The specifications of the fiber optic sensor (Baumer AG, Switzerland) are presented in Table 4.1. Maximum detection displacement is set to 0.2 mm in order to achieve a linear operating range of the fiber optic sensor. The deformation of the sensor and the transition of the displacement are depicted in Figure 4.1 (b).

The two critical criteria for the determination of flexure material were 1) MR compatibility and 2) stiffness appropriate for low force measurement (< 20 N). I used selective laser sintering, a method of 3D printing to achieve high precision and maintain material properties. I used Sinterstation 2500+ HiQ (3D Systems, Valencia, CA, USA), with standard ALM N12 sintering parameters with a part bed temperature of 174 degrees Celsius. The material I used is Nylon12 PA powder provided by Stratasys (see Table 4.2 for material details).

Based on our CAD design (Solidworks 2015-2016, SolidWorks Corporation, MA, USA) imported to Matlab 2016b (Mathworks, Natick MA, USA), I performed a static simulation based on finite element methods (FEM) provided in partial differential equation toolbox. The key parameters regarded in PDE models were Poisson’s ratio of 0.394 and the mesh size of 0.03mm. The simulation was done on 10-node tetrahedral elements with

quadratic interpolation functions. Although not detailed here, the displacement was under 1% difference compared to Solidworks static simulation with mesh size 0.8mm. Critical dimensions in terms of achieving target displacement (0.2mm when static 20N force applied) were the width of the parallel beam, width of the inclined beam, the angle of the inclined beam opposed to the parallel beam, and the thickness of all beams. One example of a geometric dimension satisfying our aim is to set a beamwidth of 0.86 mm, a thickness of 9 mm, and an angle of 60 degrees. The resulting displacement when 20N of static force was applied was 0.2073 mm. The displacement along the vertical axis is described in Figure 4.1 (b). I collected data using a data acquisition board (NIDAQ USB-6009, National Instruments, Austin, TX). Data were collected at 100 Hz.

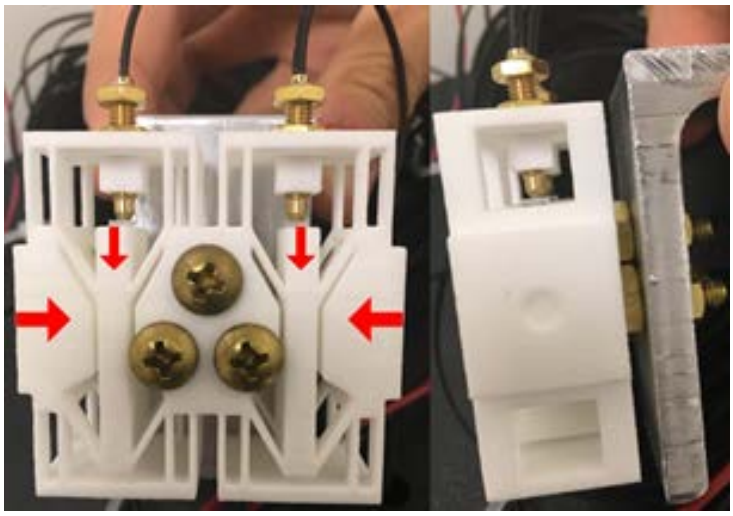

(a)

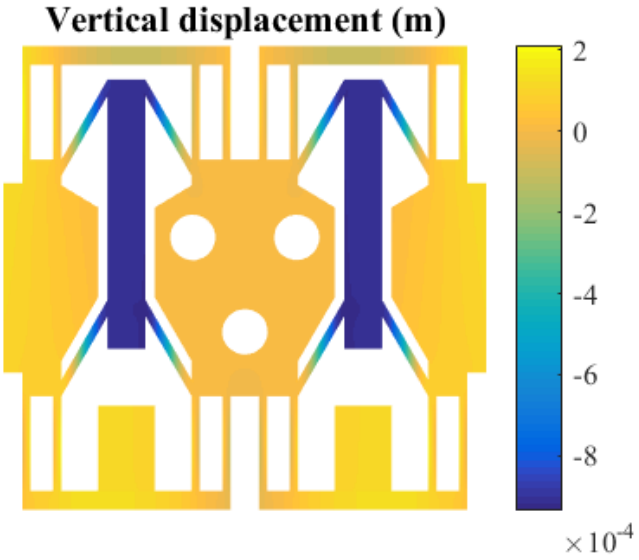

(b)

Figure 4.1. Sensor design (a) Printed force sensor mounted with fiber optic sensor (b) Simulation results: Vertical-displacement

4.3 SENSOR CHARACTERIZATION

I evaluated the linearity, hysteresis, and frequency bandwidth to judge overall sensor performance. The procedure of the experiment performed to characterize each property is described as follows:

I applied standard weights to the ungrounded flexure laying on its side to ensure equivalent force on both sides. The applied weights were 50g, 100g, 200g, 400g, 600g, 800g, and 1000g (= 9.8 N). Each weight was applied 6 times and the output voltage was recorded at the steady-state of the sensor readout. Figure 4.2 (a) shows a linear relationship between force and output voltage. (R^2=0.987)

Hysteresis in a viscoelastic material such as Nylon 12 is a critical property to identify, especially at deformations of varying frequencies. I applied different forces (5N, 10N, 15N maximum range) and different frequencies (0.1 Hz, 0.16Hz, 0.2Hz, 0.33Hz, 0.5Hz, 1Hz, and 2Hz) while simultaneously recording force from a separate transducer (Futek, Advanced Sensor Technology, Inc., Irvine, CA, USA). For each force and frequency combination, 60 cycles of loading and unloading were applied and averaged in the time domain relative to the other. Results are described in Figure 4.2 (b) and Table 4.3. Hysteresis increased with applied force and frequency. The maximum hysteresis was 18.9% of the applied force (10 N at 2 Hz). The minimum hysteresis was 1.6% (5 N at 0.1 Hz).

Regarding that human tapping frequency may reach up to 5 Hz [87, 88], I estimated that the maximum griping frequency may be similar or less than tapping. Thus, I inspected the frequency response of the developed sensor by applying a randomly varying force over a 240-second period. A reference force sensor was used to verify accuracy. I estimated the transfer function by applying a fast Fourier transform. The Bode plot in Figure 4.2 (c)

describes the approximated estimation of magnitude and phase shift in the range of 0.1Hz to 4Hz compared to reference force measurements. The phase shift increases in high frequency as a result of high hysteresis.

The force sensor I aimed to design in this study resulted in a sensitivity of 100 N/mm on the fiber optic end, and 5 N/V on the NIDAQ acquisition end. The peak force measurements are reached within 1 sec after the force is applied. The maximum force detection range was set to 20 N due to our targeted application; however, by alternating dimensions, the range of force detection and the sensitivity of force measurements can be adjusted.

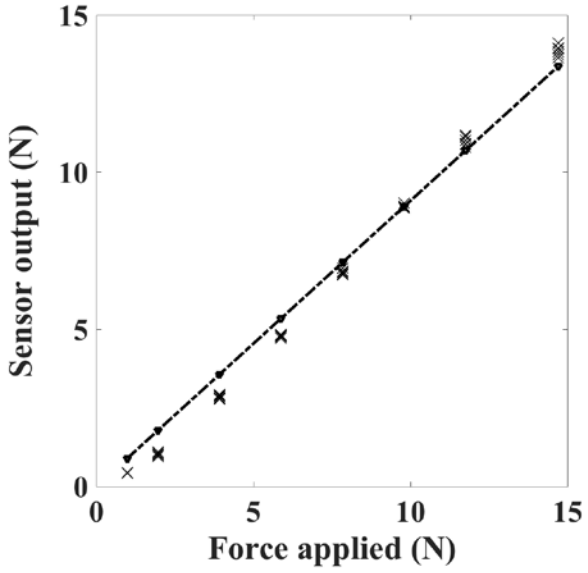

(a) Linearity

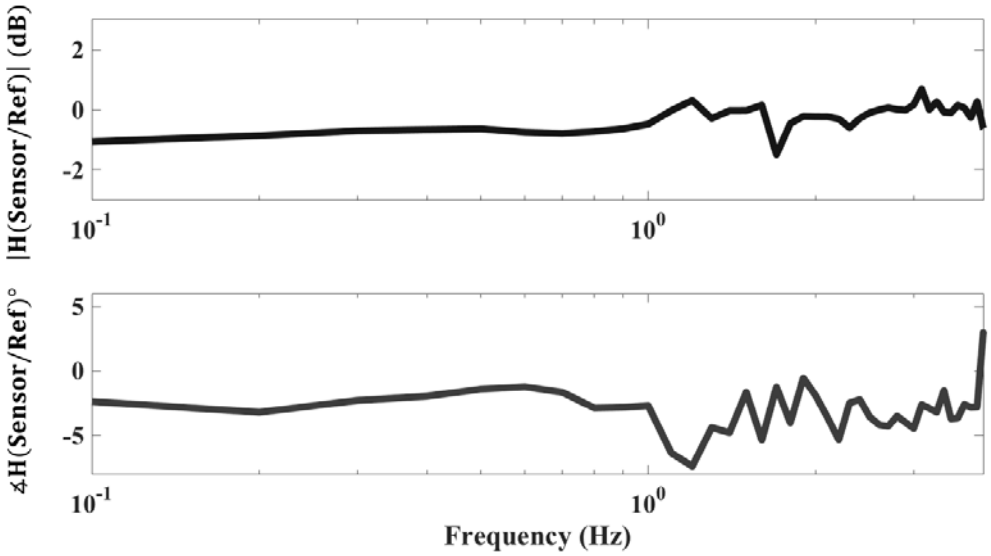

(b) Bode plot of Random input 0.1- 4 Hz

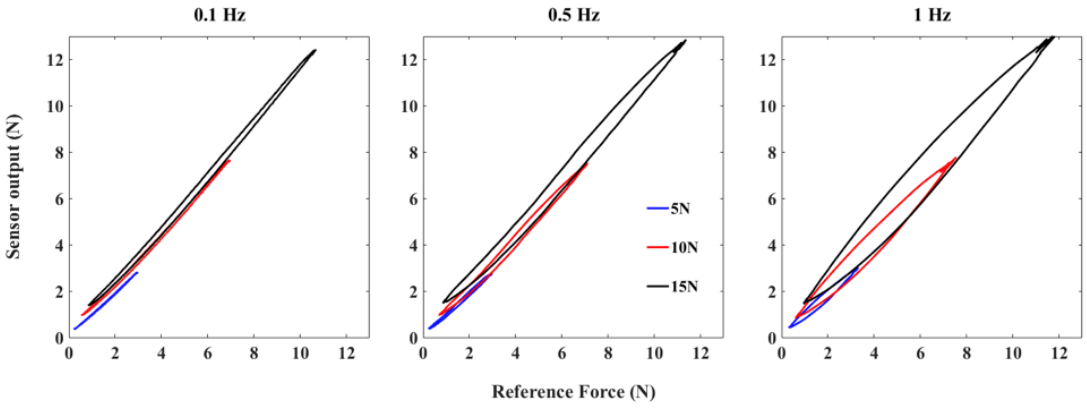

(c) Hysteresis with varying frequency and force

Figure 4.2. Characterization of the force sensor

TABLE 4.1 SPECIFICATIONS OF THE FIBER OPTIC SENSOR

Fiber Optic	FUE200C1004
Optical Amplifier	FWDK 10U84Y0
Cable length	10 m
Range of sensing distance	10 mm
Light source	680 nm pulsed red LED
Response time / release time	1 – 50 ms
Head material	Brass
Sensor head size	Ø4 × 20.0 (L) mm
Sensor base size	10.0 (W) × 29.7 (H) × 60.0 (D) mm

TABLE 4.2 SPECIFICATIONS OF NYLON12 PA

Elastic modulus	1.3×10^9 (N/m^2)
Poisson's ratio	0.394
Shear modulus	3.189×10^9 (N/m^2)
Mass density	1.02×10^3 (kg/m^3)
Tensile strength	4.7×10^8 (N/m^2)
Yield strength	4.698×10^8 (N/m^2)

TABLE 4.3 HYSTERESIS OF FREQUENCY X FORCE (%)

	5N	10N	15N
0.1 Hz	1.60	2.13	2.79
0.16 Hz	2.02	2.59	2.92
0.2 Hz	2.18	2.97	2.98
0.33 Hz	2.78	3.87	4.57
0.5 Hz	3.77	5.53	6.56
1 Hz	9.25	12.2	13.8
2 Hz	13.2	18.9	16.2

4.4 DISCUSSION & CONCLUSION

The purpose of this investigation was to design a force sensor capable of independently measuring forefinger and thumb forces at low force levels in an MR environment. In this work, I described the design of the device, simulate its deformation characteristics, and then perform an engineering evaluation of its linearity, hysteresis, and bandwidth. Our dual flexure design, inspired by previous work [75], was manufactured using Nylon 12, 3D printed by SLS. Overall, its performance was acceptable, with some considerations.

The overall design was found to be fairly linear, with a range of hysteresis between 1.6 and 18.9%. The bandwidth response, like the hysteresis, was primarily affected by higher frequency (i.e., 2 Hz) forces. While this may be acceptable for some applications, the design may be able to be improved using thicker walls. While aluminum would undoubtedly have lower hysteresis values, our prior designs required wall thicknesses that were too thin and thus entered plastic deformation upon typical use. Possible alternative materials with high elastic moduli could be used but may not be able to be 3D printed and thus high precision features such as corners would likely negatively affect performance.

In this study, I presented a force sensor that is MR-compatible, high precision in geometric dimension, and sensitive enough to detect low force range without mechanical failure. The presented sensor is one possible solution specified to accommodate our specific motor task of interest. The design optimization in terms of balancing force detection range, mechanical stability, geometric dimension, precision, accuracy, hysteresis, and analytical modeling is under investigation.

CHAPTER 5

Primary visual beta-band oscillations reflect motor control processes during dynamic visuomotor (pinch-force) tracking

5.1 INTRODUCTION

Control of precision pinch and grasp relies on an extensive cortical network for which research has traditionally focused on frontal and parietal regions subserving executive and visuomotor integration functions, respectively [89]. However, evidence suggests that cortical oscillations within the primary sensorimotor and visual cortices, in addition to reflecting low-level function (e.g., movement or stimulus parameters, respectively), may also process high-level functions (e.g., task or goal-directed processes) as part of a task-based integrative network [90]. Integration of visual information during object manipulation provides a foundation for internal models of body movement within the external environment [91] and helps to improve accuracy and consistency during goal-directed movements [92]. The posterior parietal cortex (PPC) has been shown to be an essential functional hub within a wide cortical network that subserves visuomotor transformations [93-96]. While there has been extensive research on the role of the PPC, primary motor (M1) and sensorimotor cortex (SMC), and executive frontal regions, relatively little is known about the involvement of the primary visual cortex within this greater visuomotor network.

The primary role of the M1 is well established. Along with the supplementary motor association cortex (SMA), M1 codes signals for generating high-level motor

output through the corticospinal system [97] of various degrees of complexity [98-105]. However, more recent studies have found that M1 also directly encodes visual information associated with movement planning and sensory feedback [106-109], shedding light on the hierarchical structure of an integrated action-perception system supporting predictive behavior [110-112]. M1 activity during motor planning changes the state of the somatosensory area indicating M1 prepares S1 to anticipate the sensory information received during the movement [113]. While much less is known about how the primary visual cortex couples to the motor system, there is some evidence of motor representation within V1. Benedetto showed that primary visual and motor cortex BOLD activity displays task-related correlation [114], supporting the idea both M1 and V1 may couple with each having its own representation of sensory and motor processing.

The studies of visual information's effect on visuomotor integration have been in the form of providing visual feedback that directly maps the motor performance. Visual feedback minimizes movement variability [115] and concurrent feedback allows automatic recalibration of visuomotor mapping [116]. The response of the visual area towards the change in task error is nonlinear, where specific regions of the visuomotor system selectively change in activity related to large changes in force error and large changes in the spatial amplitude of visual feedback [117]. Removing visual feedback lowers the structural variability of inter-digit force coordination, which is explained by the change of high-level control strategy, leading to two digits becoming more coupled under somatosensory feedback [118]. This was observed in chronic stroke patients where they expressed higher stability in bimanual force control without visual information

[119]. Accurate visually-guided hand movements are achieved by utilizing perceptual and spatial information processing that is tightly linked to visual inputs [120]. While evidence suggests that sensory input tightly linked to the movement goals reduces movement variability, improved performance was not always achieved with increased amounts of sensory information [121]. The underlying mechanism of how sensory information is attributed to reduced variability in movement within the hierarchical visuomotor network is poorly understood.

Precision grip is a motor skill developed throughout childhood that allows controlled manipulation of objects [122]. The accuracy of precision grip force control is degraded in healthy aging and also in numerous neuromuscular diseases [123-127]. The experimental examination of precision grip has been often in the form of static force control in humans. Comparison of precision grip gently holding an object to power gripping revealed that more regions involved in precision grip than power grip, indicating precision grip incorporates a more demanding manipulation [128]. Manipulation of force level during static grip led to the finding that frontoparietal activations engage with a small force [129]. Experiments designed to have a long duration of static force attempted to identify coherence in between electromyography [130-131], changes of mu rhythm [132], alpha coherence correlating to accuracy [133]. However, the fact that the dynamic task has a differential representation compared to the static task [134], and that dynamic precision grip engages a segregated but differential cortical network compared to the static grip [135] suggest an emphasis on high-temporal dynamics of visuomotor integration.

Investigations of cortical oscillations underlying sensorimotor processing have shown that the beta band (15 ~ 30 Hz) is strongly modulated by movement and somatosensory input. Transient increases and decreases in spectral power recorded using electroencephalography (EEG) and magnetoencephalography (MEG) have been termed event-related synchronization (ERS) and desynchronization (ERD) respectively [136-138]. These phenomena have been shown during and following preparation and performance of voluntary movements [139], passive movements [140], and even during imagined movements [141-143]. Non-invasive scalp EEG, MEG and intracranial measurements using depth or electrocorticogram (ECoG) recordings have provided significant knowledge regarding the time course and putative neural generators of these sensorimotor rhythms in humans. The advance time-domain signal processing have contributed novel information regarding the nature of cortical oscillations within the motor and sensory structures of the brain and will likely continue to play an important role in identifying the underlying mechanisms of motor cortex oscillations and their functional role in motor control. Recently, it was found that the amount of beta ERD within the visual areas during motor execution primarily predicted the amount of motor errors, suggesting both alpha and beta oscillations within visuomotor cortical networks play a prominent role [144]. Another study revealed on monkeys that these top-down beta-frequency oscillatory processes coordinate the processing of sensory information by conveying global states to early levels of sensory cortical hierarchy independently of bottom-up stimulus-driven processing [145]. While these studies strongly implicate a role for visual beta oscillations in visuomotor control, neither study controlled or tested

for the influence of visual information and force level on the beta-band response. Hence, the functional significance of primary visual beta-modulation requires further investigation.

In this study, I measured the oscillatory responses of motor and visual areas. I examined how alpha/beta bands are portrayed in both sensory and motor processing in a hierarchical top-down network during a dynamic visuomotor task with MEG. Magnetoencephalography (MEG) and electroencephalography (EEG) have the ability to capture high-temporal profiles of neural activations measured non-invasively [146]. I chose a task with unique properties: 1) dynamic, isometric precision grip, 2) an instructed constant rate of change of force, 3) a required independent control of forefinger and thumb forces and 4) manipulations in mapping between pinch force and visual target position. The goal of the tracking task was to control a cursor and follow the target moving at a fixed speed along a 45 – degree diagonal trajectory as accurately as possible. The visual feedback was introduced in two conditions, Coupled, where the position of the cursor moved based on the average force of the forefinger and thumb, and Independent, where the cursor's two degrees-of-freedom were independently controlled by thumb and forefinger forces. I predicted that participants would interpret the Coupled condition to be less complicated, leading to a larger error in controlling both finger forces. I anticipated that the more complicated Independent condition would engage bilateral beta oscillations in the motor area. I examined the differences in the time-frequency responses of the motor and visual areas in the form of alpha and beta band modulation. I hypothesized that the variability of alpha and beta modulation would

correlate to changes in the behaviors underlying the performance of the continuous visuomotor processing throughout the task.

5.2 STUDY DESIGN

5.2.1 Subjects

Sixteen healthy participants, eight females, with normal or corrected to normal vision, were recruited to participate in the experiment. All subjects provided informed consent approved by the University of Texas at Austin Institutional Review Board. Participants were asked to avoid caffeine intake and to avoid sleep deprivation the day prior. Two participants were excluded due to excessive artifact or other metallic noise interference during the MEG scanning. Thus, fourteen participants remained in the final analysis (seven females, age 18-34 yrs., mean 25.8 yrs., SD = 5.0). All subjects were right-handed based on the Edinburgh handedness test (mean 83.1, SD = 15.4), [147].

5.2.2 Stimulus and Task description

The task follows the work of Spirduso et al [148]. Participants controlled a computer cursor by isometrically pinching a custom-made non-magnetic force transducer [149]. Forefinger and thumb forces were mapped to horizontal and vertical movement of a cursor on a screen. The sensor mapped 0 – 20 % MVC across the full range of each axis within the viewing screen described in Figure 5.1 (a). The task was displayed on a back-projected screen using a DLP projector connected to a stimulus delivery computer running custom software developed in Python. The distance from the subject's nasion to the

projection screen was 1 m. The display dimension was 1024 x 768 pixels having a visual angle of approximately 7º.

Participants were instructed to manipulate the cursor in order to track a circular target moving along a diagonal tracking line as accurately as possible. The mapping of force across the track line represented 4 – 16 % MVC bottom left to the top right and constituted an angle of 45º (Figure 5.1 (a)). Participants performed two task conditions that were differentiated only by the level visual feedback: (1) Independent, where the horizontal and vertical positions of the cursor were mapped independently onto the force generated by the forefinger and thumb, respectively, and (2) Coupled, where the cursor position was represented as the average of forefinger and thumb forces, thus constraining cursor motion along the diagonal track. Participants were only instructed to follow the target as accurately as possible.

Each trial started with a red trackball at the bottom of the diagonal track-line and the subjects' yellow cursor ball at the very bottom left of the viewing screen. A Trial was initiated by a change in trackball color from red to green, indicating that the participants should apply force to move the cursor toward the trackball. When the cursor reached a 2% force radius of the trackball, the cursor turns blue, and the trackball starts to move along the yellow diagonal trajectory at a constant speed (trial onset). The trackball traveled up the diagonal trajectory for 3 sec, reversed, and moved back for 3 sec to the origin. During tracking, if the cursor diverges more than 2% force radius of the trackball during tracking, the cursor color changed to pink. Once the tracking finished, the trackball turned to red,

the cursor disappeared, and the trackball remained static for 3 sec while participants rested until the next trial. The time evolution of a single trial is described in Figure 5.1 (b).

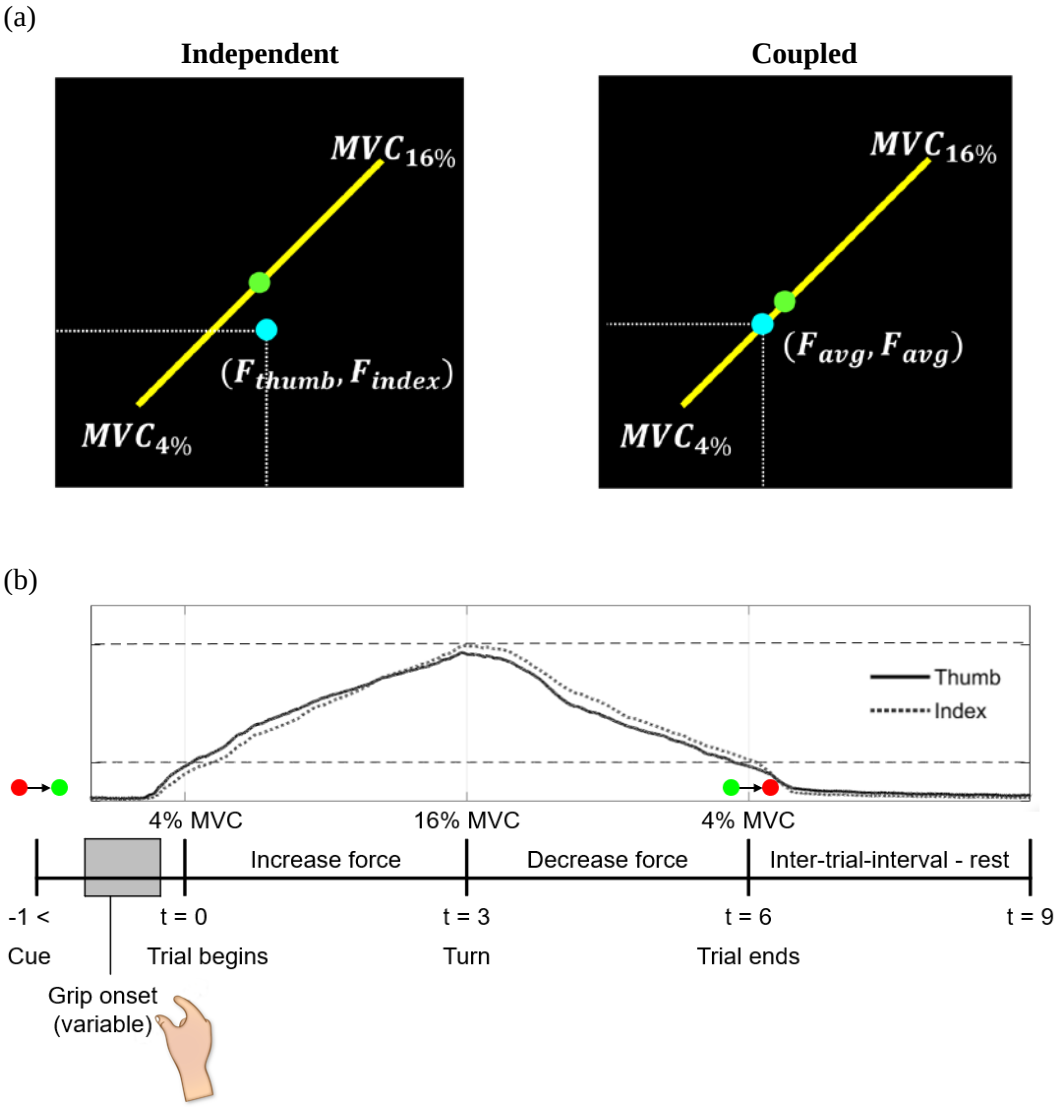

Figure 5.1. Experimental setup in both (a) *Independent* (left) and *Coupled* (right) conditions. The task was mapped to 0-20% of each participant's MVC, visually identical to all participants. In Coupled condition, the target was bounded along the trajectory whereas in the Independent condition, the target was allowed to vary from the pattern. (b) Time evolution of a single trial where the vertical axis is arbitrary units of force.

(c) (d)

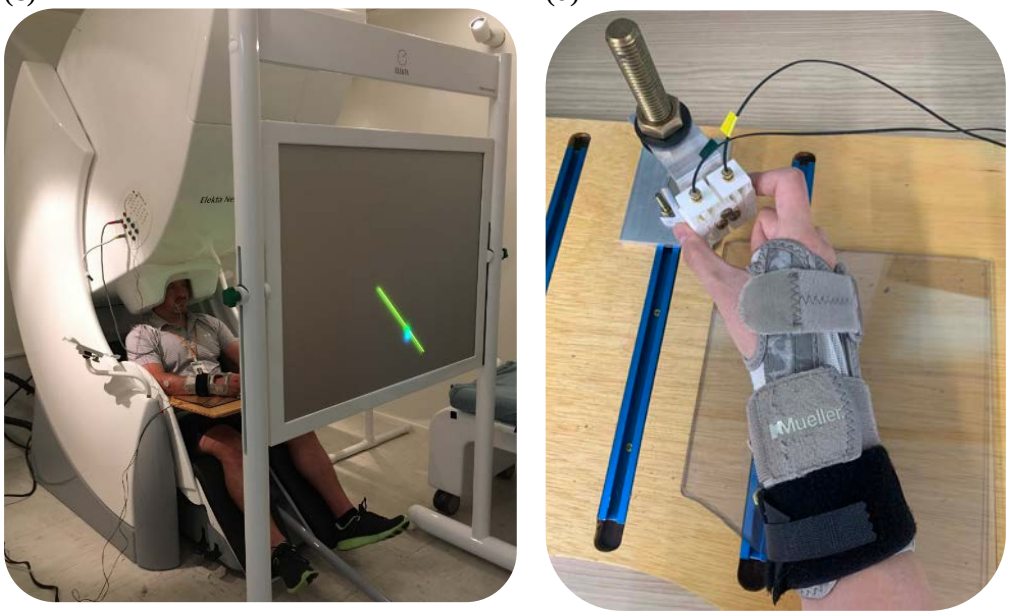

Figure 5.1. (c) Setup in MEG room – participants were seated in an upright posture. (d) Customized desk to fix right forearm with cuffs. The precision grip posture was adjusted to a comfortable position for each participant.

5.2.3 Data Collection

The experiment was carried out over two sessions on separate days. The first session consisted of an MVC determination and task familiarization. MVC was collected to normalize the task difficulty across participants while performing an isometric contraction [150]. MVC was measured for each participant using a manual force measurement system, including a custom-made dual strain gauge mounted on a base capable of differential measurement of forefinger and thumb forces [148,149]. Participants executed three MVC trials with 30 seconds rest in between. Participants were directed to

maintain MVC for 5 seconds within a trial. The average MVC across trials was used to determine the experimental task forces. The training session was composed of five blocks of 20 trials using the Independent condition.

5.2.4 MRI Acquisition

Participants were scanned in a Siemens Skyra 3T MRI scanner with a 32-channel head coil at the University of Texas at Austin. The image was taken using the MPRAGE sequence (TR = 2.3s; TE = 2.98ms; 208 slices; 256 x 240 matrix size; 1 mm slice thickness) to collect structural scans. The images were later used to co-register with the MEG data.

5.2.5 MEG Acquisition

In the second session, participants were brought to the MEG scanner at Dell Children's Medical Center no later than 7 days following the first training session. The neuromagnetic activity was recorded using a whole-head 306-channel MEGIN Triux MEG system (MEGIN OY, Helsinki, Finland) in a magnetically shielded room located within Dell Children's Medical Center (Figure 1(c)). All MEG and peripheral biological data were collected at a 1 kHz sampling rate and band-pass filtered from 0.3 – 330 Hz. Prior to recording, a Polhemus Fastrak system was used to digitize the location of fiducial landmarks at the nasion and left and right tragi, as well as 5 head position coils used for head coordinate system localization within the MEG helmet. Bipolar electrocardiography (ECG), electrooculography (EOG), and surface electromyography (EMG) was recorded using the systems EEG amplifier from (1) lumbrical (unipennate), (2) opponens pollicis, and (3) flexor carpi radialis muscles to track to correlated muscle activation of flexion in

the forefinger, thumb, and wrist, respectively. Electrocardiography (ECG), and a single channel of diagonal to EOG to track eye movement and blinks.

Participants sat in an adjustable upright chair with our custom-designed force sensor mounted on a desk described in Figure 5.1(d). The participant's extraneous arm movement was constrained by using a wrist brace anchored to the apparatus's mounting desk. The angle of the sensor with respect to the hand was adjusted to a comfortable position, the right forearm in the sagittal plane, and the ulnar surface of the hand resting on the desk. Participants were instructed to remain relaxed when not performing the movement.

I collected 5 mins of resting data, a single run of the Independent condition, and a single run of the Coupled condition. The order of the conditions was counterbalanced across participants. Each experimental run contained five blocks of 24 trials each: resulting in 120 trials per run. Rest was assigned 90 seconds in between the blocks. Throughout the trial, three triggers were simultaneously recorded along the MEG signals to mark the following events: trial onset, trackball onset, and rest. The reversal time points were determined in post-hoc analysis. Each run lasted about 25 minutes, and the whole MEG recording took about 70 mins. The location of the head position was checked before and after every run to check for excessive head movement (> 5 mm).

5.3 DATA ANALYSIS

5.3.1 Behavioral analysis

Each trial performance was represented by root-mean-square error (RMSE) of finger forces normalized to the participant's MVC by calculating the Euclidean distance in the 2D task space. The force RMSE was calculated in the following equation.

$$Force\ RMSE_{(x(t),y(t))} = \sqrt{\left(\frac{F_{x(t)} - F_{x_o(t)}}{MVC_{thumb}}\right)^2 + \left(\frac{F_{y(t)} - F_{y_o(t)}}{MVC_{index}}\right)^2}$$

where F_x, F_y are raw force measured F_{x_0}, F_{y_0} are the target force given as the task. To contrast task-relevant errors given that the visual feedback was manipulated, I also calculated the task RMSE, where the definition is, how well 'visually' participants performed the task. For the Independent condition, force RMSE is identical to the task RMSE; however, in the Coupled condition, the task RMSE does not consider how well both finger forces are balanced during the isometric pinch and only considers error along a single dimension of the track line. Therefore, the calculation is as follows:

$$Task\ RMSE_{(x(t),y(t))} = \sqrt{\left(\frac{F_{avg(t)} - F_{x_o(t)}}{MVC_{thumb}}\right)^2 + \left(\frac{F_{avg(t)} - F_{y_o(t)}}{MVC_{index}}\right)^2}$$

The EMG signals were measured to monitor abnormal contractions and to estimate the degree of correlation with neuronal modulations as a result of isometric contraction. The EMG signals were measured to evaluate if the activation level directly correlated to neuronal modulations. The signals were high-pass filtered at 10 Hz, and then Hilbert transformed to estimate the amplitude. The activation was normalized by the average amplitude in the baseline window, -700 – -200 ms before trackball onset. After normalizing the amplitude, I integrated the normalized amplitude over the trial window to represent assess each trial's total EMG activation level.

To evaluate if oculomotor activation was different between the conditions, I normalized EOG activation across the whole run. The signal was band-pass filtered from 0.5 - 50Hz, and I calculated the Pearson's correlation of the normalized EOG signal and the task trajectory over the 6-second window of each trial. The eye movements should follow the task trajectory as the target moves up and down to adjust the focal point of the eye field to have the target located in the center. The correlation reflects how similar the shape of the eye movement follows the task trajectory.

Given that the participants were allowed to initiate the task after the trial onset began, I inspected the reaction time between the trial onset and trackball onset. Trials were discarded where the reaction time exceeded one second or subjects otherwise did not complete the trial. The average number of trials in each condition was 86.1 ± 6.8 in the Independent condition and 88.5 ± 1.8 in the Coupled condition.

5.3.2 MEG preprocessing

MEG preprocessing and source estimation were carried out using BrainWave, a Matlab toolbox developed at the Hospital for Sick Children [151], to estimate and analyze beamformer source estimation from MEG signals. 204 channels of gradiometer MEG data were epoched into 10-second trials from -1 to +9 seconds time-locked to the start of the trackball movement, i.e., trial onset in Figure 5.1 (b). Four corrupted channels specific to the MEG machine was removed from all subjects' data. MEG data underwent automated threshold rejection, and trials containing peak to peak amplitudes greater than 3.5pT were removed from analysis. Trials were further visually inspected, and trials were removed containing excessive muscle and or eye-blink artifacts not captured by the threshold routine. Lastly, trials in which the subject failed to continuously perform the task for the duration of the trial were removed.

5.3.3 Beamformer source estimation

To localize brain activity from the MEG data, I used a linearly constrained minimum variance (LCMV) beamformer, an adaptive spatial filter, that provides no localization bias in the presence of random noise [152]. LCMV Beamformers aim to pass the signal from the location of interest while blocking signals from all other locations. The localization of brain activity, the signal of interest is defined by the forward solution for current sources at each location. The maximal attenuation of other sources in a least-squares approach is based on spatial correlations present in the measured signal. The spatial resolution of the beamformer is dependent on the signal-to-noise ratio of the target source.

A minimum-variance beamformer for the brain location defined by 3D position vector r = (x,y,z) consists of a unique set of a sensor-weighting matrix, denoted as W(r). The total power $S^2(r)$, projected by a spatial filter over an interval of time is given by the temporal integration of the measured signal m(t), scaled by the beamformer weights.

$$S^2(r) = \int |W^T(r)m(t)|^2 \, dt$$

The source power at location r over a given time interval would be obtained from

$$S^2(r) = trace(W^T(r)C_m W(r))$$

where, C_m is a M x M covariance matrix of the data measured at M sensor channels, computed over the time interval T. W(r) is the beamformer weight matrix consisting of N columns of M-dimensional weight vectors, where N represents the number of independent signals emanating from the target location r in the brain. LCMV beamformer is generated with constraints of minimizing signal power while maintaining linear responses of filter to each signal of interest arriving from the target voxel. For brain signals, these sources are modeled by the lead fields of orthogonal dipole sources located at each voxel.

$$W(r) = C_m^{-1}H(r)[H^T(r)C_m^{-1}H(r)]^{-1}$$

where C_m is the data covariance matrix and H(r) is the matrix of forward solutions (lead fields) for all dipole sources at location r. When forward solution is setup with spherical model, only tangential sources contribute to the MEG signal and H(r) can be reduced to two tangential dipoles with orthogonal orientation. With the assumption that signals from cortical sources are primarily due to current flow perpendicular to the cortical surface, the realistic estimate of this direction can be obtained, a scalar beamformer can be computed for a single current direction at each voxel. This method both improved SNR [152,153] and provides a single time series of source strength for each voxel location. The SAM beamformer iteratively searches for this optimal orientation by maximizing the noise normalized source power output of the beamformer over all data segments. This noise normalization of power estimate has been termed 'pseudo-Z' statistics [154,155] necessary to remove spatial distortion due to the uncorrelated (white) noise gain of the weights that scales with increasing distance from the sensors. The weights are used to obtain total source power P(r), over all trials and samples, with weight vector normalization to remove spatial distortion in the image [156].

$$P(r) = W^T(r)C_m W(r)[W^T(r)W(r)]^{-1}$$

The beamformer reconstruction may be erroneous making distinction on highly correlated two closely spaced sources, however, beamformer is shown to be robust to partial correlation between the sources [157]. Additionally, beamformer has shown to preserve interdependencies of periodic sources and that phase-synchronization of

interacting non-linear sources was not perturbed by the analysis. The beamformer output can be computed for all voxels in the predefined source space, forming a statistical parameter mapping (SPM). The images exhibit non-uniform projection of sensor noise throughout the volume. By normalizing the beamformer output, inherent bias can be compensated. Assuming that the sensor noise covariance matrix (∑) is known, the normalized beamformer output is computed as [154]:

$$Z_r^2 = \frac{P_r}{N_r} = \frac{W_r^T C_b W_r}{W_r^T \sum W_r}$$

where, Z_r, is the pseudo-Z statistic for location r and N_r, power of the projected sensor noise. Noise sensitivity is only required for normalization, and in practical situation, this becomes redundant if interested in the statistical difference between contrasting windows. (e.g. active and control conditions). The T-statistics for each voxel can be calculated, where the weight calculation stage is skipped, are called pseudo-T [158]:

$$T_r = \frac{P_r^{active} - P_r^{control}}{N_r^{active} + N_r^{control}}$$

Beamformer output is simply a projection of the measurement vector onto the lead field for the target voxel [159], known as signal space projection (SS)[160].

5.3.4 Region of interest identification

Identification of the primary sensorimotor and visual cortices was carried out via localization of task-related alpha- and beta-band oscillatory modulations of induced brain rhythmic activity using the differential SAM beamformer in BrainWave. Datasets from both conditions were included to identify the primary source; therefore, 28 datasets. First, I registered each participants' structural MRIs and ran FSL [161] to create individual brain surfaces. I marked the fiducial points (nasion, left and right targi) collected during the MEG session using Brainwave import MRI function to co-register the structural MRI and the MEG session and then used FSL BET2 to extract the head surfaces. SPM12 was used for co-registration to align each structural MRI to the template brain and created a 9 cm patch-based multisphere head model [162,163] for forward source modeling. Based on this model, I applied a bandwidth-based scalar SAM beamformer algorithm [154] for each alpha and beta band in each condition across all participants to search for the center of significant volumetric responses. To increase the sensitivity of alpha and beta band modulations, I applied 8 – 13 Hz, 15 – 30 Hz band-pass filters, respectively. To see the time-course changes of the modulations, I took each trial epoch from -3 to 10 seconds, setting t = 0 as the trackball onset. I took baseline as 500 ms before the trackball onset and set the covariance estimation window from 2 – 4 sec. Then a pseudo-Z map was created for each bandwidth and each condition every 500 ms non-overlapped in the whole epoch with root mean square noise of 3 fT/sqrt(Hz). I ran a permutation test iterating 1,024 times and selected the strongest sources accounting for sensorimotor and visual areas bilaterally for further analysis. The MNI coordinates of the source locations are presented in Table

5.1 and depicted in Figure 5.2 (a). The most robust and focal finding across motor and visual cortices was found in the beta-band post-task time period. The virtual sensors were created using the forward solution head model for each participant. The data was band-passed 1-40Hz.

5.3.5 Time-frequency representation

After creating the virtual sensors with significant responses, I estimated the time-frequency response (TFR) using a Morlet wavelet frequency transformation [164] in each trial and averaged it in each participant. The source activity was calculated over a frequency range of 1 – 40 Hz in 1 Hz steps using the following formula:

$$\mathrm{w}(\mathrm{t}, \mathrm{f}_0) = \left(\sigma_t \sqrt{\pi}\right)^{-1/2} \exp(-t^2/2\sigma_t^2) \exp(2\pi f_0 j t)$$

Wavelets were normalized so that the total energy was one by the normalization factor with magnitude in the nAmps scale. To track the change of modulation as a function of the task, I normalized the power to, i.e., percent signal change, of the whole epoch using the average power in the whole trial window of 0 – 6 seconds. (Figure 5.2 (b)) The main purpose of using whole trial time window as baseline, was to maximize relative changes within the task, expected to be a low amplitude signal. Event-related desynchronization (ERD) is a decrease of power modulation, therefore negative percent signal change. Event-related synchronization (ERS) is described as an increase of power modulation relative to

the baseline resulting in positive percent signal changes for group response, I averaged the percent signal change in each source and in each condition.

I validated the first level group time-frequency response to identify the modulation within the epoch. I applied Wilcoxon's sign-rank test on each time-frequency point, filtered $p < 0.05$, and created a cluster on connected valid time-frequency points (uncorrected, Figure 5.2 (c),(d)). To correct for multiple comparisons, I analyzed the time-frequency response in the resting period (Figure 5.2 (d)-1, 2). To account for the probability of forming clusters of time-frequency points where the percent signal change across 14 participants is significantly non-zero, I calculated the percent signal change of the resting period between the trials. I had four blocks of a 90-second resting period. I created non-overlapping 3-sec windows in 70 seconds within the resting period to match the number of trials where I discarded the first and last 10 seconds to avoid any movements occurring. The number of created trials for each participant was 92, and I selected 2.5-sec with random jitter within each 3-sec trial. I generated the percent signal change group average on 2.5-sec window time-frequency response during the resting period converted to percent signal change as I did with the original task trial. Once the clusters were created using Wilcoxon sign-rank test, I calculated the size of each cluster and took the maximum size. By repeating this 2,000 times, I created a distribution of maximum cluster size. I took the top 5% cluster size as a threshold to filter the cluster in the original trial epoch time-frequency response. Only clusters larger than the threshold survived for further analysis (Figure 5.2 (e)).

5.3.6 Contrast between the conditions

I examined both behavioral measurements and time-frequency responses across the conditions for differential effect as a result of setting visual feedback dissociating the behavior and visual feedback. Each participant had behavior parameters represented as the single summary statistics. The RMSE of both force and task were averaged across the whole trial period, from 0 – 6 seconds, the integrated normalized EMG was averaged across the whole trial period. EOG measurement was represented as the average of Pearson's correlation of all trials for each participant in each condition. I applied Wilcoxon sign-rank paired test to check if any of the behavior measurement was different between the conditions.

To test the modulation differences, I performed the Wilcoxon sign-rank test on the time-frequency percent change plot generated by subtracting the Coupled condition from the Independent condition in each participant ($p<0.05$, uncorrected). Then I clustered the differential percent change time-frequency map in each source as the second level group analysis.

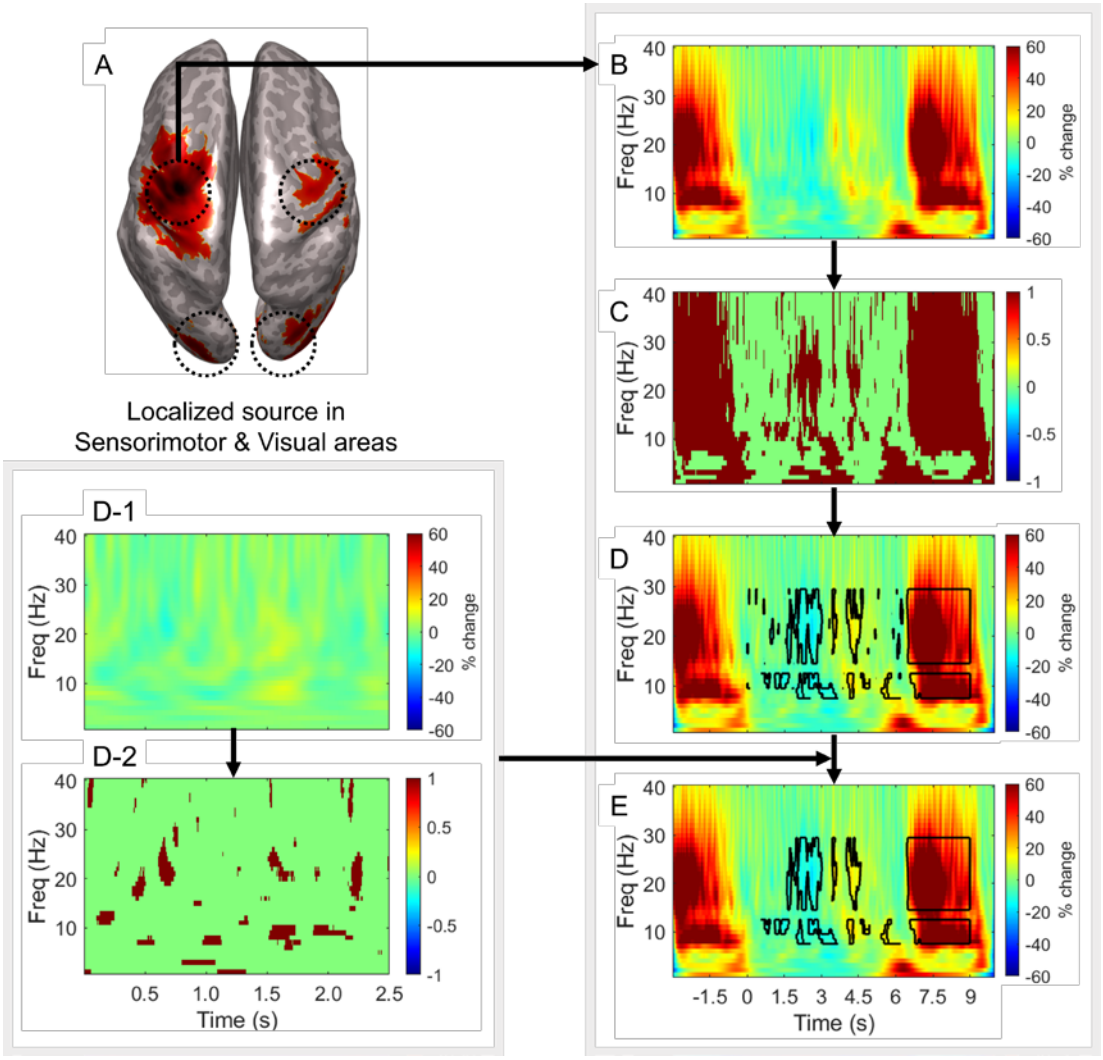

Figure 5.2. Image processing from source localization to 1st level group time-frequency response validation. (A) Sources in M1, V1 with differential SAM beamformer, beta-band filtered, baseline as -0.5 – 0 seconds including all datasets. (B) Average percent change in a single source: power is estimated with Morlet wavelet, then normalized to percent signal change with 0 – 6 seconds. (C) Wilcoxon sign-rank result tested in each time-frequency point with $p < 0.05$, two-sided. (D) Clusters of significant time-frequency points (uncorrected): the clusters are created within the beta band (15 – 30 Hz) and alpha band (8 – 13 Hz) across the epoch of 0 – 9 seconds. (D-1) Average percent change in resting period (D-2) Valid clusters in resting period ($p<0.05$, two-sided): the maximum cluster size of 2000 iterations used to generate null distribution. (E) The clusters are filtered accounting for multiple corrections using a 5% cluster size of null distribution from (D-2).

5.3.7 Trial basis analysis

Individual trial basis analysis was performed after summarizing group-level responses for both behavioral parameters and time-frequency responses. Each trial was converted to percent changes by performing the same Morlet wavelet transform. Two behavioral parameters were set for comparison, force RMSE, and the task RMSE in each participant and in each condition. To represent neural responses on a trial basis, I selected mean (μ), the variance (σ) of the percent signal change as the summary statistics. Additionally, I calculated the Pearson's correlation (ρ) between the time course of error and the envelope of percent signal change in alpha or beta band of bilateral sensorimotor and visual areas. The summary statistics were primarily calculated within the time window of 0 to 6 seconds to represent whole trial.

5.3.8 Two-way repeated measures of ANOVA

In order to identify how behaviors and neural modulations are correlated, two criteria were selected to label the trials in each participant for both conditions: good/bad trials of force RMSE and task RMSE. I selected 40 trials of good performance (low RMSE) and 40 trials of bad performance (high RMSE) then set conditions and performance as factors for a 2 x 2 design study. The response variables were mean (μ), variance (σ) of percent signal changes in both sensorimotor and visual areas and correlation (ρ) between RMSE and the percent signal change. Once I found the significance in the ANOVA test, I ran a post-hoc analysis to further investigate the response in depth.

5.4 RESULTS

5.4.1 Behavior

The average thumb finger MVC was 55.9 ± 17.9 N while the average of index finger MVC was 55.1 ± 18.1 N. The difference between thumb and index finger MVC was on average 0.8 ± 2.1 N that thumb MVC was slightly larger. The average of the parameters was calculated from each participant and compared across conditions by performing paired Wilcoxon paired test. I found no difference across the conditions in all three channels of integrated EMG ($p = 0.345$, 0.336, and 0.369 respectively) and in the Pearson's correlation coefficient representing the eye movement (Independent 0.55 ± 0.11, Coupled 0.56 ± 0.07, $p=0.548$). In short, participants contracted the muscle and moved both eyes similarly in both conditions. The average time for participants to start pinching after the visual cue of the trial was 438.3 ± 169.2 ms and 495.1 ± 333.1 ms in the Independent and Coupled conditions, respectively. We did not observe a difference between conditions ($p=0.502$). The time from squeezing the force sensor to reaching a point to start a fixed 6-sec-pace tracking task was 552.0 ± 170.1 ms and 520.1 ± 160.2 ms ($p = 0.058$). Lastly, the time between the end of the task and the actual release of the finger forces was examined inspecting both force and EMG measurements. Using a threshold based on the correlation between pressure sensor deceleration and EMG decrements, the average time of release was 177.1 ± 123.7 ms and 259.9 ±160.8 ms for Independent and Coupled tasks, respectively. Participants tended to release significantly earlier in the Coupled condition than in the Independent condition ($p=0.035$).

I predicted that the force RMSE would be larger in the Coupled condition due to demanding less visual attention to the task. The force RMSE was significantly larger in the Coupled condition than in the Independent condition ($p=0.0012$). However, contrary to the force RMSE, the task RMSE, visually how task is performed, was significantly larger ($p=0.001$) in the Independent condition than in the Coupled condition. The correlation between the force and task RMSE in the Coupled condition was 0.677 ± 0.272, with range [0.248, 0.992]. The high correlation coefficient indicate that the force error and task error were positively correlated, where participant would achieve this if they pinched the sensor with balance of two fingers. It is possible to achieve low task RMSE but still high force RMSE because task RMSE in the Coupled condition takes the averaged force of both finger forces applied on the sensor. The average force and task RMSE are presented in Figure 5.3.

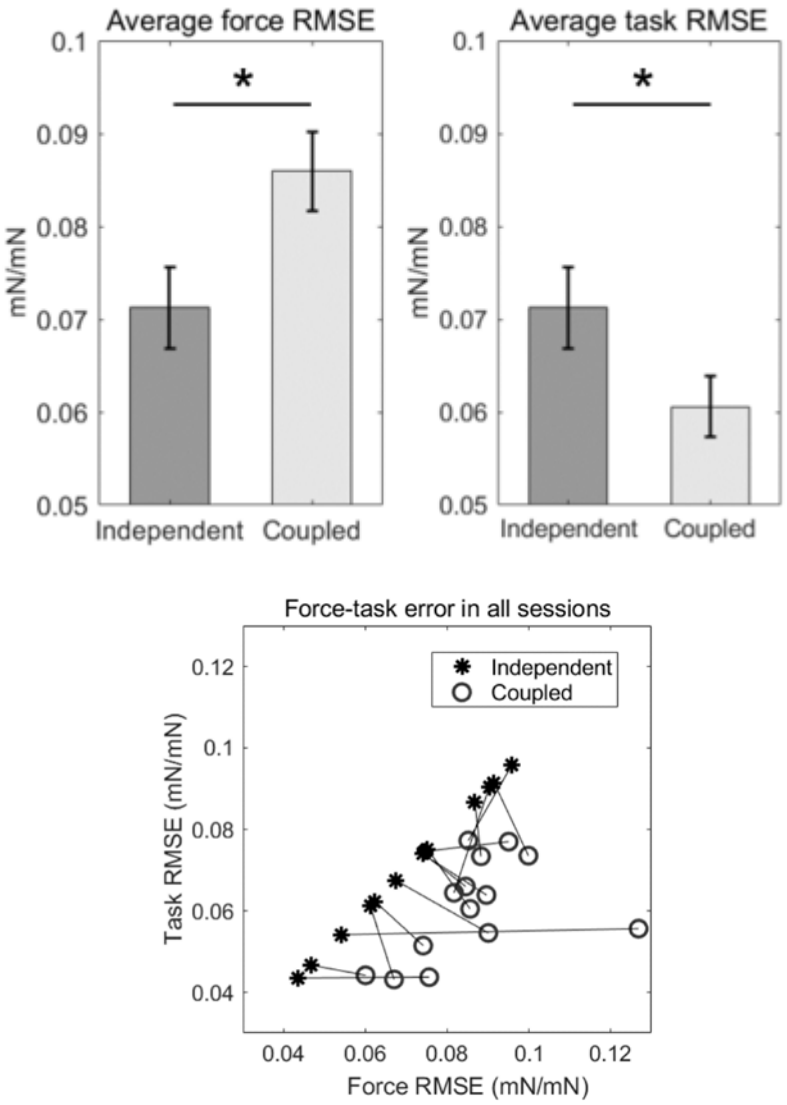

Figure 5.3. Averages of force RMSE (left) and Task RMSE (middle) compared across conditions. Note that participants pinched more off-balanced in the Coupled condition despite visually perceiving to perform better. Force and task RMSE are identical in the Independent condition, but task RMSE in the Coupled condition was calculated based on the 'average' force of two fingers. (right) The relationship between task RMSE and force RMSE slightly varied across participants. Those cases with low task RMSE but high force RMSE indicate that participants performed isometric pinch with less balanced forces on both fingers. This behavior was driven by providing a single instruction, which was to track the target as accurately as possible.

5.4.2 Beamformer source estimations

Beta-band SAM analysis found to have strong positive peak in both sensorimotor and primary visual areas. Both areas showed the highest contrast in the post-task period as an event-related synchrony (ERS), but with different latencies. For visual area, this occurred immediately following the termination of the task in the 6 – 7 second range, whereas sensorimotor area showed a slightly delayed ERS in the 7.5 – 8 second range. The anatomical locations in standard MNI space are summarized in Table 5.1. The volumetric image of the SAM ROI map is visualized in Figure 5.4 (a), as are the Beta-band time courses showing the strong post-task rebounds for both visual and motor cortex (Figure 5.4 (b)). From this point, I will use abbreviated expression to represent source localized in left primary somatosensory area (Brodmann area 03) S1(but including primary motor area (M1)) and right visual area (Brodmann area 17) V1.

(a)

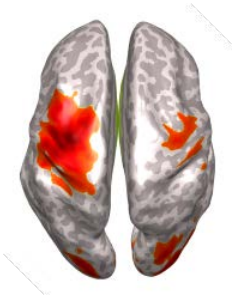

Table 5.1. Locations of analyzed source in MNI space

f	Pseudo-T	MNI (mm)			Gyral location	Brodmann Area	Time window (s)
		X	Y	Z			
β	4.38	-42	-24	54	L Postcentral	BA03(S1)	7.0 – 7.5
	3.06	38	-16	62	R Precentral	BA04(M1)	7.0 – 7.5
	4.71	-22	-88	2	L Middle occipital	BA19(V3-5)	6.5 – 7.0
	4.10	26	-84	6	R Cuneus	BA17(V1)	6.5 – 7.0

(b)

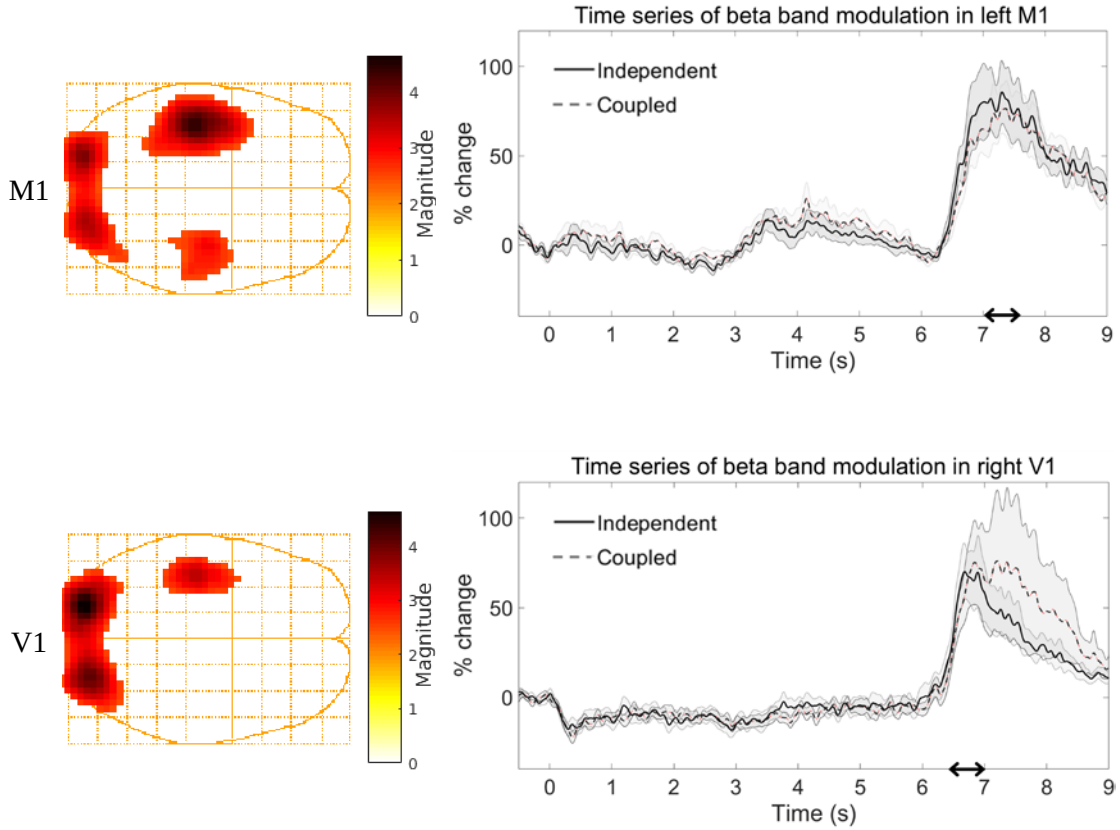

Figure 5.4. (a) Volumetric image of localized sources across all participants and conditions. The localized sources expressed the strongest response in bilateral sensorimotor and visual areas in the beta-band. (b) Left S1 showed the strongest response in the 7.0 – 7.5 seconds time window. (Top left) Right V1 was localized in a 6.5 – 7.0 seconds time window. (Bottom left) The changes of the modulation within the epoch for S1 and V1 are presented on the right column.

5.4.3 Time-frequency response of primary sources

Over the time course of the task and I found significant alpha- and beta-desynchronization and synchronization in both V1 and S1. The TFR maps and values are displayed in Figure 5.5. Left S1 expressed alpha desynchronization in both conditions whereas right M1 alpha desynchronization appeared to be rather spontaneous and weak. V1 also responded during the task with alpha desynchronization, both conditions had stronger ERD in right V1 than left visual area. The beta band modulation during the task in S1 and M1 represents the ERD as a result of movement execution [165], the significant response appeared around the turn-around time point in bilateral sensorimotor areas in both conditions. However, the strength of the beta ERD was stronger in left S1 in the Independent condition. Notably, I found intermediate beta ERS right after the turn left S1 in both conditions, where the effect appeared to be stronger in the Coupled condition than in the Independent condition. Wide frequency range of beta ERD lasted throughout the task in right V1 in both conditions. Left visual area also expressed beta ERD during the task in both conditions but were more localized in the event of task onset and turn around point. Once the task ended, the disengagement of both fingers was expressed in a form of ERS in both alpha and beta band in both sensorimotor and visual areas. Post-movement beta rebound (PMBR) primarily appeared in the left S1 in both conditions. The similar behavior was found in V1 where strong beta and alpha ERS appeared post-task bilaterally and in both conditions. The onset of ERS in V1 was earlier than that of M1 in both conditions as the peak of beta modulation was localized in the earlier time segments of 500 ms. There were no differences between the conditions in TFR plots ($p>0.05$, corrected).

Figure 5.5. Time-frequency response normalized as percent change using baseline (0 – 6 sec). The significant percent change clusters are selected with bootstrapping statistics. (top) Response of left S1 and right M1 (bottom) response of visual area

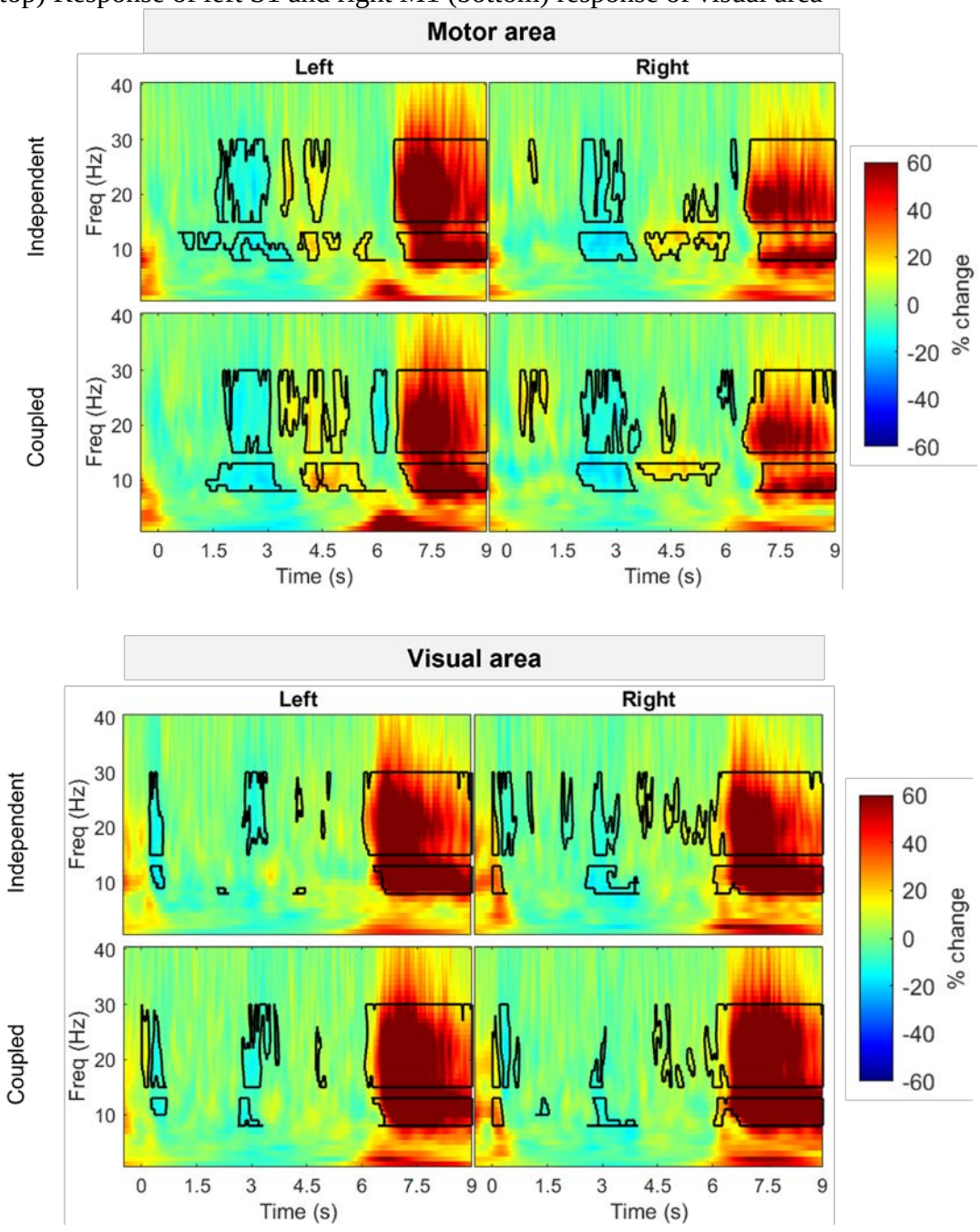

5.4.5 Characterization of significant ERS/ERD

First is the intermediate ERS after the turn in the left somatosensory area and right visual area. I expected strong beta ERD as a reflection of motor execution, however, the synchrony after the turn was quantified to be a positive percent signal change. Therefore, I compared the modulation in the left sensorimotor area and right visual area before and after the turn in each condition (Figure 5.6 (a)). The next modulation I noticed in the left sensorimotor area was in a time window of 5.5 – 6.0 seconds. The strong increase of synchrony after the task terminates is expected as well-known as post-movement rebound, however, I found a short duration of ERD right before the task termination. I also analyzed the modulation comparing across the conditions (Figure 5.6 (b)). On top of the evidence that I anticipate post-movement rebound in sensorimotor area, I found the similar behavior in bilateral visual area in both conditions. The strong synchrony was located with a peak in beta-band. I estimated the amplitude changes in both sensorimotor and visual areas to analyze the beta synchrony post-task (Figure 5.6 (c)).

5.4.5.1 Intermediate ERS right after the turn

I found the beta-band percent signal change in left S1 in both conditions expressed a slight increase right after the turn. I contrasted the modulation by separating the task period into before turn (0 – 3 sec) and after turn (3 – 6 sec) and performed sign-rank test to verify the change in level of synchrony in both conditions (Figure 5.6 (a)).

5.4.5.2 Desynchronized modulation immediately after task termination in left M1

The modulation in left S1 area is expected to express strong beta-band desynchronization as the movement still exists until the end of the task. Before the initiation of beta-rebound, I found a short-term beta desynchronization that was significant in the Coupled condition group time-frequency response, but not in the Independent response. The amplitude of the activation is suppressed as I normalized the modulation by taking the whole trial time-window of 0 – 6 seconds. The time series of average beta-band percent signal change is presented in Figure 5.6 (b).

5.4.5.3 Beta-band modulation post-task period in both M1, V1

Beta-rebound post-task in sensorimotor area is expected supported by the evidence as beta-rebound is associated with the termination of movements. The average percent signal changes within the time window of 6.5 – 8.0 sec were 67.63 ± 51.48 in the Independent condition and 53.85 ± 40.46 in the Coupled condition (Figure 5.6(c)). The difference between conditions was not significant. I found similar beta-band response in bilateral visual area where the amplitude increased immediately after the task was terminated. However, it occurred earlier than in left M1 PMBR (< 350ms) and lasted shorter than PMBR. The average percent signal changes within the time window of 6.5 – 8.0 sec were 64.61 ± 46.37 in the Independent condition and 83.97 ± 127.94 in the Coupled condition (Figure 5.6(d)). The significant time-frequency area in first level group average included the upper alpha band but the peak primarily was within the beta band for both conditions. I compared the average amplitude in resting period, whole-trial period, and the

post-task time window to investigate how strong the synchrony occurred (Figure 5.6 (e)). The average amplitude was suppressed as opposed to the resting period in both sensorimotor and visual areas, and only in sensorimotor area that the amplitude post-task was significantly larger than the average amplitude during the whole-trial period. V1 responded the same, however the amplitude shifts were not as large as the M1.

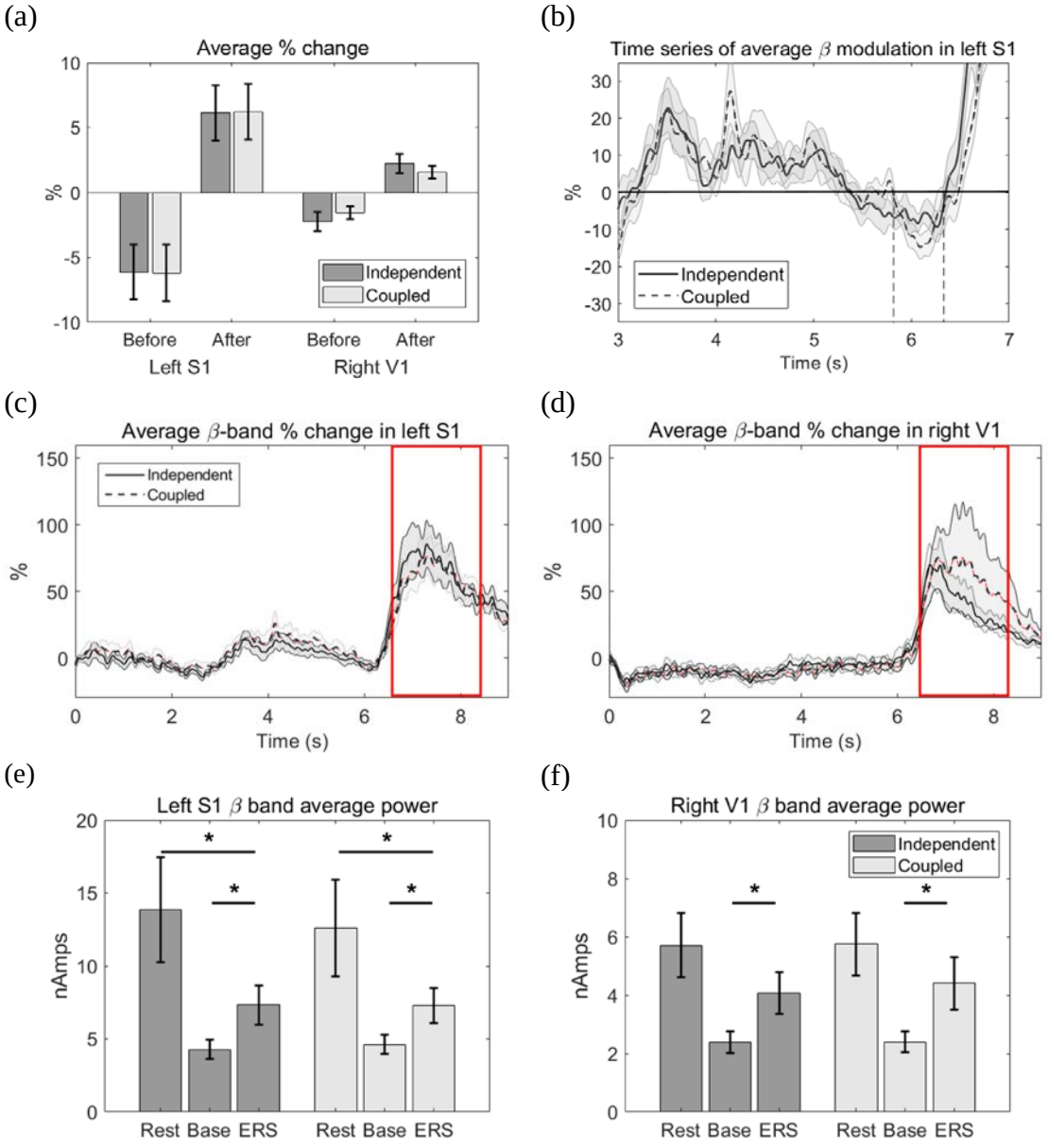

Figure 5.6. Results of post-hoc analysis (a) Both left M1 and right V1 had ERD in the first half of the trial period and ERS in the latter half of the trial period. Because of the existence of movement until the end of the task, we would expect continuous ERD. (b) The short duration of ERD post-task represents that the amplitude is suppressed more than the average trial period followed by the steep increase of synchrony. (c) Post-movement beta rebound. (d) Beta-band synchrony post-task is similar to PMBR. It is notable that V1 had an earlier onset than left M1. (e) Amplitude comparison in left M1 beta-power. (f) Amplitude comparison in right V1 beta-power.

5.4.6 Relating behavior with oscillatory responses - two-way repeated measures of ANOVA

I identified the correlation between force and task RMSE and found that they are not necessarily always strongly correlated. I performed two-way repeated measures ANOVA setting conditions and performance level as factors. Trials were labeled good/bad based on either task or force RMSE, then observations were selected to be mean (μ), variance (σ) of the percent signal change in alpha and beta-bands and Pearson's correlation (ρ) between RMSE and modulations during the whole trial time period (0 – 6 sec). I did not find any mean percent signal changes being affected by either condition or level of performance ($p>0.05$)

I found that the correlation between an alpha-band percent change and force RMSE in both left and right sensorimotor areas was significantly different across conditions ($F(1,13)=12.41$, $p=0.004$ in left S1 and $F(1,13)=10.08$, $p=0.007$ in right M1, described in Figure 5.7 (a)). The beta-band response was similar in bilateral sensorimotor area, that correlation between force RMSE and beta-band percent change was affected by the condition, not by the level of force RMSE. ($F(1,13)=16.26$, $p=0.001$ in left M1 and $F(1,13)=5.15$, $p=0.041$, described in Figure 5.7 (b)). The correlation between task RMSE and alpha-band in right V1 was affected by conditions but not by the level of task RMSE ($F(1,13)=7.02$, $p=0.020$, Figure 5.7 (c)). The correlation between task RMSE and alpha-band right M1 was affected by the level of task RMSE, but not by the condition ($F(1,13)=7.82$, $p=0.015$, Figure 5.7 (d)).

Both condition and the level of performance affected the variance of alpha and beta-band percent signal changes in right V1 during the whole trial-time period. The alpha band

variance was significantly different between condition ($F(1,13)=6.60$, $p=0.023$) and by level of force RMSE ($F(1,13) = 5.14$, $p=0.041$) with no interaction effect ($F(2,13)=0.90$, $p=0.360$). The post hoc analysis revealed that variance was significantly different via the level of task RMSE in the Independent condition. Beta-band variance was different between conditions and level of task RMSE with interaction effect. ($F(1,13)=17.97$, $p<0.0001$, $F(1,13)=5.20$, $p=0.040$, $F(2,12)=3.74$, $p=0.075$). Interestingly, the same trend was found when trials were separated by force RMSE, that alpha band was affected by both conditions and level of force RMSE but no interactions were found ($F(1,13)=5.43$, $p=0.037$, $F(1,13)=5.25$, $p=0.039$ for each condition and level of force respectively). However, beta-band variance was affected by both factors with interactions ($F(1,13)=18.88$, $p<0.0001$, $F(1,13)=5.55$, $p=0.034$, $F(2,13)=4.83$, $p=0.047$). The visualization of the result that variance of beta-band percent signal change in right V1 was affected by both condition and level of performance with interaction is presented in Figure 5.7 (e). Beta-band variance reflected both visual and force variability which force, and visual feedback were dissociated in the Coupled condition.

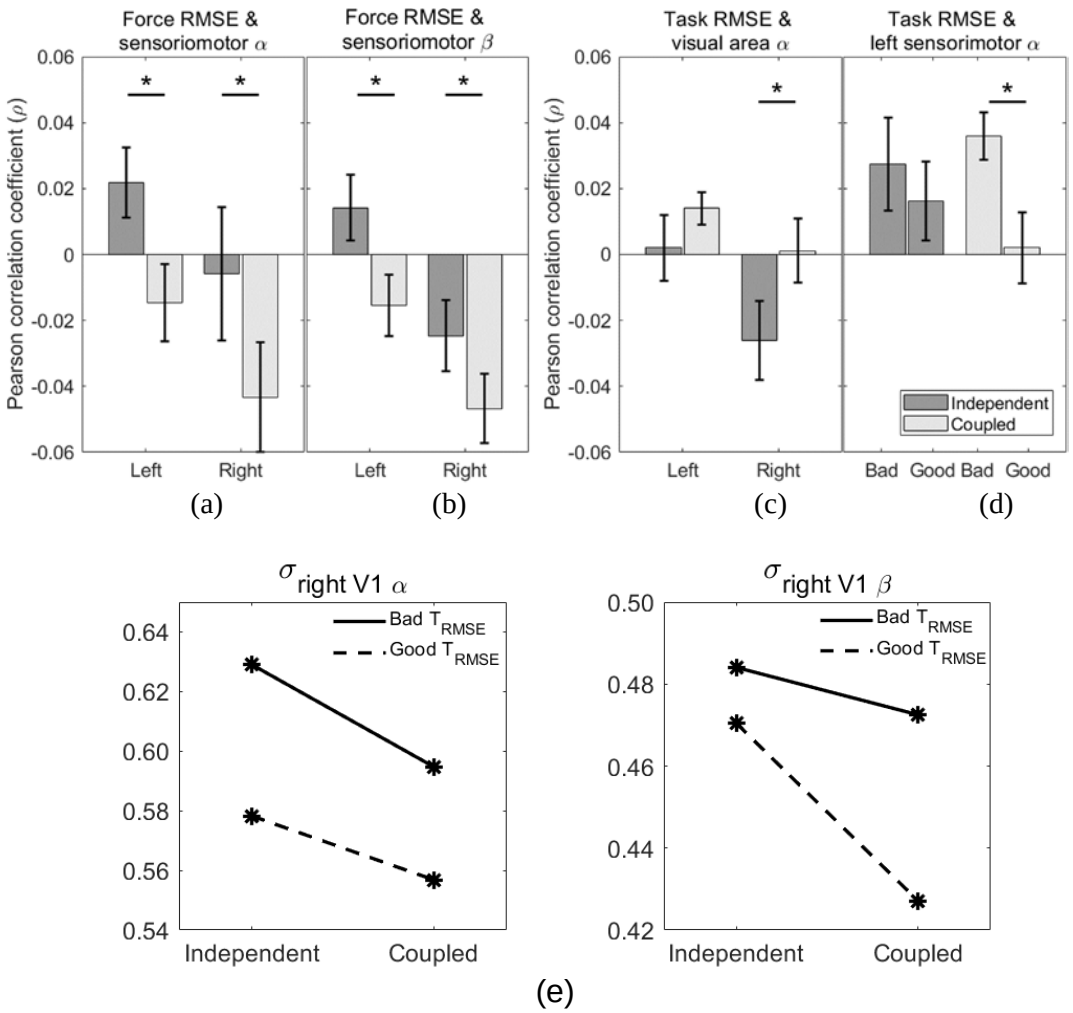

Figure 5.7. Results of two-way repeated measures of ANOVA in search of relating behavior and modulations. Force RMSE was correlated to both (a) alpha and (b) beta band in bilateral sensorimotor area. While task RMSE was correlated to (c) alpha band in right visual area and (d) alpha in left sensorimotor area which both condition and level of performance affected. (e) The variance of alpha and beta bands in right visual area have shown to be affected by both condition and the level of performance. Alpha-band (left) in visual area directly reflects the level of visual process, where in independent condition, processing 2D information. Therefore, the Coupled condition performance did not vary the variance of visual process as much as the Independent condition. However, beta-band (right) in visual area reflects the level of cognitive process because in the Coupled condition, participants 'perceptually' recognize as if they are performing better.

5.4.7 Negative peak – posterior parietal cortex response

I localized the source that had positive peak pseudo-T statistics provided by Brainwave beamformer reconstruction in sensorimotor and visual area. I localized negative peak during the task in right parietal posterior cortex, however, the magnitude of pseudo-T was below 2.5. The localized source location in MNI space is described on Table 5.2 and the time-frequency response in Figure 5.8. The peak occurred during the trial window, where the turn occurs. The difference between conditions was also weak in posterior parietal area. However, the synchrony post-task was similar to that of in both sensorimotor area and visual area.

Table 5.2. Location negative peaks

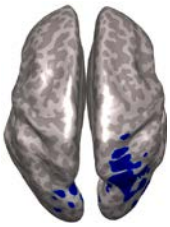

f	Pseudo-T	MNI (mm)			Gyral location	Brodmann Area	Time window (s)
		X	Y	Z			
β	-2.45	26	-72	34	R precuneus	BA07	2.5 – 3.0
	-2.22	-18	-84	22	L cuneus	BA18	3.0 – 3.5

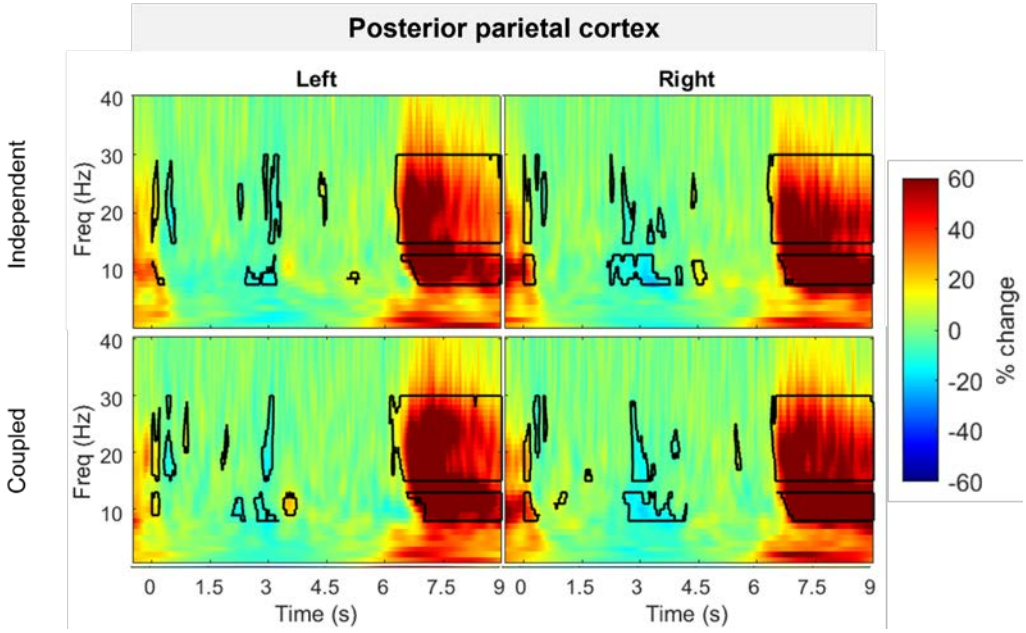

Figure 5.8. Time-frequency response of sources localized as negative peaks. The peaks were located only within the trial period of 0 – 6 seconds. The maximum strength was captured in time window of 2.5 – 3.5 seconds.

5.5 DISCUSSION

In this experiment, I set out to investigate the role of cortical oscillations in the primary visual and motor cortex during a dynamic visuomotor tracking task and found strong focal modulation of the visual cortex in the beta-band frequency that was spatially independent of the posterior parietal cortex. I set up two visual feedback conditions dissociating visual processing to understand the high temporal dynamics of sensorimotor integration in primary M1 and V1. Behavior-wise, the force RMSE was larger in the Coupled condition, however, the task RMSE was smaller in the Coupled condition. This contradiction implies that in the Coupled condition, participants were off-balancing two-finger forces but visually perceiving to perform the task better. Both eye movements and surface EMG activation were excluded as major influences on the observed neuronal oscillations as both measurements were not statistically different across conditions. Then, analyzing the neural response, the strongest response was localized in beta-band activity in both bilateral sensorimotor and visual areas. I expected to find stronger percent signal changes related to the visual degree of freedom, however, the differential effect was not clearly separated via our conditions. The summary statistics of modulation (i.e. mean, standard deviation) did not reveal the differential behavioral effect, however, the time-course correlation to RMSE changes in force or task RMSE revealed that both M1 and V1 modulated according to the changes of force and task RMSE. Force RMSE was dominantly related to bilateral M1 in both alpha and beta bands, regardless of the performance of the trials. Additionally, left M1 alpha-band modulation was affected both by condition and level of task RMSE. The finding that the M1 alpha band reflected sensory processing is supported by the evidence, where this reflects that instantaneous motor correction followed by the continuing motor execution is affected by the visual feedback. Lastly, right V1 alpha

and beta band modulation variability was affected by both conditions and the level of performance.

Role of beta band, traditionally been represented motor process

The function of beta oscillations in sensorimotor cortex has been extensively investigated and is known to fluctuate during movement. Movement-related beta desynchrony is present during spontaneous and triggered movements [166] and successful movement cancellation is associated with an increase in beta [167-169]. It also appears without a muscle contraction (i.e, motor imagery or action observation) and is rather insensitive to parameters like movement type or effector [166]. This evidence led to the idea of beta ERD representing an active process that interferes with the encoding of information income while updating the current state of the system. Thus, the beta-band serves as representing top-down inhibition during motor and cognitive tasks. The PMBR in this sense is interpreted as endogenous fluctuations of beta level during a motor set. That motor-related beta desynchrony is required for controlling the inhibition and allowing the initiation of a motor plan, while PMBR preserves existing motor states both internal and external sources of noise. PMBR has also been interpreted as an indicator of movement outcome processing [170]. Evidence has shown that PMBR is modulated by passive movements [141, 171] and by kinematic errors [172]. The level of PMBR over the sensorimotor cortex served as an index of confidence in predicting motor outcome, equivalent to the forward model [173]. Some studies observed that primary beta synchrony and PMBR have different spatial distributions and may represent independent events [174,175]**.** My task has shown both beta-desynchrony while performing the task and PMBR after the trial termination. The strength of ERD and PMBR was not different between the conditions however, our data suggests that a similar functional role may occur

in primary visual areas. The sensorimotor cortex expressed a contralateral-weighted asymmetric beta modulation, wherein the primary visual area was bilateral and dominant in the right hemisphere. In the visual area, the timing of the beta ERD during the task was correlated with the major event within the trial (e.g., task initiation, turn-around point) and also tracked with the sensorimotor beta ERD. By normalizing the data with respect to the whole task interval, it is clear that beta bursts in both visual and motor cortices are associated with transient changes in movement dynamics, in spite of the fact that relative to pre-task levels, the underlying beta oscillations remain sustained throughout the whole trial (Appendix A Figure 1). The strong beta synchrony in bilateral visual area post-task appeared similar to that of PMBR in the primary motor area, where the onset was significantly earlier than the primary motor area (< 400 ms, $p < 0.05$) and percent signal change were lower in magnitude than in primary motor area. Regarding that, the average amplitude of beta-band in V1 is less than the M1 during the resting state, beta-synchrony post-task in V1 is more to recovering back to its baseline status than expressing upshoot in M1. A similar behavior suggests that the status quo in the primary motor area might also be conveyed through beta-band in the primary visual area as well for the dynamic visuomotor task. The behavior of beta-band synchrony post-task in both M1 and V1 becomes more distinct when contrasted with posterior parietal cortex time-frequency response (Figure 5.8, Appendix A Figure 1). The beta modulation suggests that the beta desynchrony during the task is centered around PPC where both M1 and V1 follow the behavior. Immediately after the task termination, PPC does not express beta-synchrony rather M1 and V1 express strong beta-synchrony as a preservation of the current visuomotor status. Interestingly, the primary visual area is revealed to have alpha band modulation representing bottom-up processing of primary visual processing (e.g., direction, position, color and etc.). It has been shown that the phase is modulated with

bottom-up feature processing that varied saliency levels are processed at different phases of alpha oscillations [176].

The results indicate that both M1 and V1 translate bottom-up & primary sensory processing through alpha band when beta modulation charges in processing top-down cognitive processing. The relatively strong beta desynchrony at the initiation and turn point in V1 denotes impulse in a shift of motor plan sustained for a short period of time (<500ms), that is associated with either visual cue or the directional change in the motion. The shift from ERD to ERS was pinpointed around the time of turning direction, wherein our task would be one of the major events to make a critical motor decision. Both M1 and V1 expressed beta-synchrony after turn, but only M1 expressed small significance. The traditional motor-related desynchronization is expected to appear that links the direct exertion of force through descending cortical pathways, however, the percent signal change right after the turn was not linearly correlated to the decrease of the force. I estimated the correlation between force and beta percent signal change in left M1 in a time window of 3 – 5 seconds. The correlation between the left M1 was -0.004 ± 0.060 in the Independent condition and -0.018 ± 0.063 in the Coupled. The confidence interval by bootstrapping correlation coefficient included 0 in both conditions, therefore, the beta-band change was not strongly correlated to the linear decrease of the force. However, because the task was designed to map up to 20% of the MVC, there is a possibility that beta-ERD change being linearly correlated to the amount of force may have been negligible. I approached this intermediate ERS to be viewed as a partial process that PMBR takes in M1. PMBR supposedly represents the resource collection in primary M1 soon after the termination of motor task [177]. PMBR is affected by various task attributes, such that the complex the motor task is, its duration after the task was longer [178], the larger the amount of force involves, the stronger the PMBR becomes. Therefore, this intermediate ERS may indicate

the partial release of motor resources soon after making the directional turn, which is the most epidemic event in our tracking task. Interesting is that V1 may be functionally doing an identical process as the M1 does. In V1, it is more bilateral as opposed to M1 but still dominating in right V1, this is coherent that the visual process takes dominancy in the right visual field [179].

Posterior parietal cortex (PPC) modulation – mediator in between M1 and V1?

Our focus of the paper was to identify oscillations in M1 and V1 specifically to investigate vision-motor coupling during a dynamic isometric pinching task with low force. However, I also localized sources in both left and right posterior parietal cortex to investigate the time-frequency response simultaneous with M1 and V1. The sources were localized with maximum negative magnitude within the time window of 2 – 4 seconds. The locations of the posterior parietal cortex and the SPM magnitude is presented in Table 5.2. The time-frequency response of the left and right PPC in both conditions are presented in Figure 8, normalizing by baseline as a whole-trial period. Location-wise in the MNI coordinate, I concluded that the source localized during the task in PPC region was not due to leakage estimation in beamformer source reconstruction. The percent signal change during the task does not stand out as much as the M1 and V1 sources, indicating that the amplitude changes were rather consistent throughout the course of the task. However, PPC in both conditions also synchronizes and resulted in higher amplitude immediately after the task was terminated bilaterally. The behavior of this is similar to M1 and V1. The ERD response in both alpha and beta around turning point (t = 3) in right PPC is coherent with the fact that right PPC dominates during visuomotor control.

In extension to discussing PPC response, I compared the time-frequency response normalized to the time window right before the task, -500 ms – 0s. The time-frequency

response of all M1, V1, and PPC taking baseline before the task is presented in Appendix II. Inspecting the response taking baseline before the task, PPC seems to mediate the response of M1 and V1 during the task and release the control of M1 and V1 post-task. Studies have shown that the PPC is functionally in the center of controlling the visuomotor network altogether. Our time-frequency response of the 3 sources represents how dynamically this network changes through alpha and beta band oscillations. However, the condition of restricting visual feedback by a degree of spatial freedom did not evoke differential modulation with 14 participants.

Limitations of the task design

I anticipated finding differential modulation through setting independent and Coupled condition. However, I did not find a significant difference in the level of modulation in both M1 and V1 sources. I investigated the amplitude estimations in the resting period between the sessions of 24 trials and baseline to find if the condition itself already biases the baseline of the activations in each source. Conclusively, I did not find any amplitude difference in both M1 and V1 sources, indicating that the condition by itself did not manipulate modulation baseline effectively enough to suspect different brain states. I normalized the modulation using the whole trial window of 6 seconds to investigate relative changes within the task, however, setting the baseline to be 500 ms just before the task had limitations. I did not control the movement onset to be time-fixed, the beginning of a new trial is indicated by changing the target. Once participants recognized the beginning, they were free to start pinching at their own intention, therefore having variability of the movement onset and by the time task begins, movement is already executed. In order to clearly state the movement onset, it is suggested to be time-locked with a sensory cue.

Another factor that may have been intervening in the modulation is the duration of PMBR. Three seconds was set up as inter-trial-interval, however, studies suggest that PMBR duration varies with parameters such as task difficulty, movement type, and the amount of movement. I may not have allowed modulation to return to a normal state before starting a new trial. However, the length of time required would have extended the experiment to unrealistic lengths.

5.6 CONCLUSIONS & FUTURE WORK

The present study was carried out to better understand the neural correlates of precision grip control while performing dynamic visuomotor task which its temporal dynamics has been remain poorly understood. The experiment controlled for constant rate of force increase and decrease with two visual feedback conditions to dissociate vision from the movement. Both primary motor and visual area alpha and beta band were modulated as a function of the task. I expected correlation in between the change of force and beta-band desynchrony in primary motor area, however, found that modulation reflected major movement parameter changes after the turn. It is expected that the beta-modulation reflect combinations of movement as a response of monosynaptic muscle control, movement prediction, change of cognitive strategy as the trial progresses and interaction in between the visual feedback. The difference between the conditions were not observed, however, additional experimental condition to investigate the layers of hierarchical visuomotor process may be achieved. In visual area, it was expected to find alpha desynchrony during the task reflecting continuous visual process to attribute to movement corrections, however, relative beta desynchrony was found around time-window where major changes of movement occurred. Results show visual area process

movement through beta-band as well, where, post-task synchrony similarly behaving to that of primary motor area may also indicate similar function of post-movement beta synchrony in primary motor area. Further studies are left with identifying the interaction between primary motor, visual and posterior parietal cortex, where other studies provided evidence that beta-band reflect information transfer between regions while performing high-level cognitive functions. Pinpointing the critical feature that determines the overall precision pinching performance is the target in such, it will allow us to compare the response in neuromuscular disorder population.

CHAPTER 6

Conclusion and Future work

6.1 CONCLUSIONS

This work investigated identifying neural correlates of spasticity, a condition common among stroke patients. I took the approach of fMRI due to the whole brain coverage and high spatial resolution necessary to image the brainstem. My second investigation centered on the neural correlates of dynamic precision grip force control. I used high temporal resolution MEG to examine the complex dynamics of the task. The major findings of this work are found below:

1. **Brainstem BOLD response to visual and acoustic stimuli**
    a. Activation of LVN and reticular formation based on previous stimuli expressed weak response

2. **Brainstem BOLD response to visual and acoustic stimuli in people with post-stroke spasticity**
    a. Stroke patients responded toward stimuli weaker than healthy cohorts
    b. Age became dominant factor in determining the level of brainstem response
    c. Brainstem was significantly smaller in volume than in healthy populations

3. **MRI-compatible force sensor to measure independent finger forces**
    a. Device was capable of measuring independent forefinger and thumb forces to a high degree of accuracy

b. Response of the sensor was fairly linear, but had high variable hysteresis

4. **Primary visual beta-band oscillations reflect motor control processes during dynamic visuomotor (pinch-force) tracking**

a. Primary motor beta-band modulation reflected more than the force, where the nonlinear behavior was asymmetric within the trial while visual conditions were. This indicates underlying function may have been different as a result of hierarchy of visuomotor control.

b. Visual area expressed beta-band modulation related to the specific event within the trial and strong synchrony post-task similar to primary motor area. These results support that visual area may have motor network internally reflected.

c. Both primary motor and visual area expressed movement and task variability through alpha and beta band oscillations.

6.2 FUTURE WORK

My work has been dedicated to investigating neural mechanisms of sensorimotor control. I employed the appropriate high-performance non-invasive neuroimaging techniques, i.e. fMRI and MEG, for these investigations.

With respect to fMRI studies, the field is moving towards applying ultra-high-field magnetic fields such as 7T and 9.4T, which under certain conditions can achieve a better signal-to-noise ratio, but not yet commonly applied in clinical cases. With greater knowledge of the subcortical brain anatomy and parallel advances in functional alignment (i.e., hyper-alignment)[180], there are greater opportunities to study the brainstem,

including its neuroplasticity. Neuroplasticity allows potential recovery of the loss function following neurological injury. Taking advantage of advances in functional imaging of the brainstem, enabling targeted neuroplasticity may be possible using fMRI neurofeedback. Yet, there numerous hurdles that remain in regard to robust brainstem imaging, recognizing the signal in real-time, and then the ability to self-regulate the circuit.

MEG measures the high-temporal neural response associated with various tasks. The true source of the neural signal is estimated based upon mathematical modeling. There still exists a debate regarding which model allows the best to estimate the true source. Validation is now appearing that combines more than two neuroimaging modalities. Studies that cross-validate fMRI and MEG using the same cognitive paradigm have started to provide insight on linking both spatial and temporal dynamics of the brain response.

APPENDIX

(a)

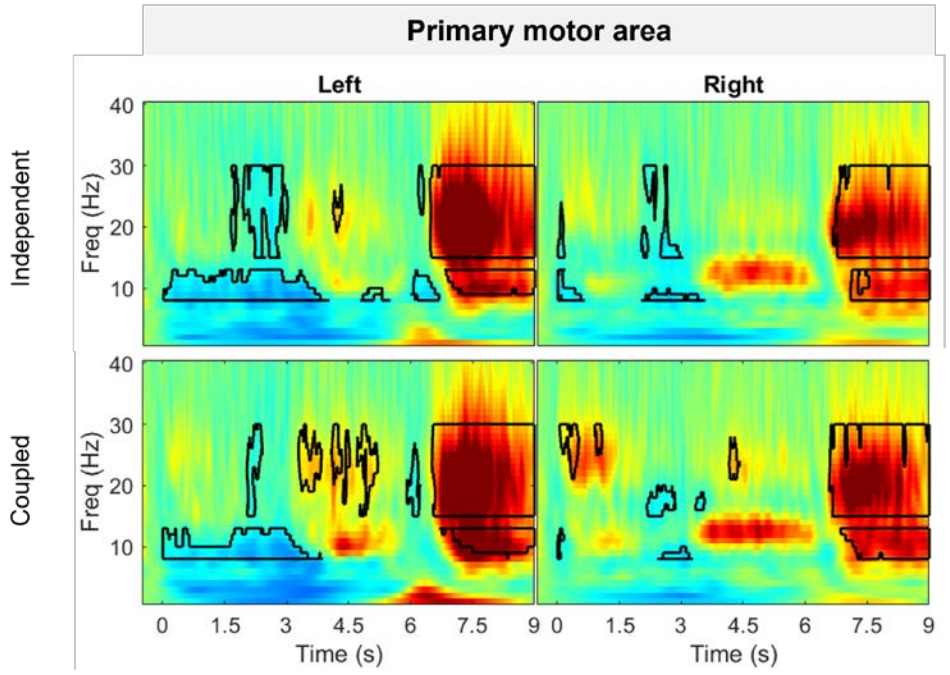
Primary motor area
Left
Right
Independent
Coupled
Freq (Hz)
40
30
20
10
0
1.5
3
4.5
6
7.5
9
Time (s)

(b)

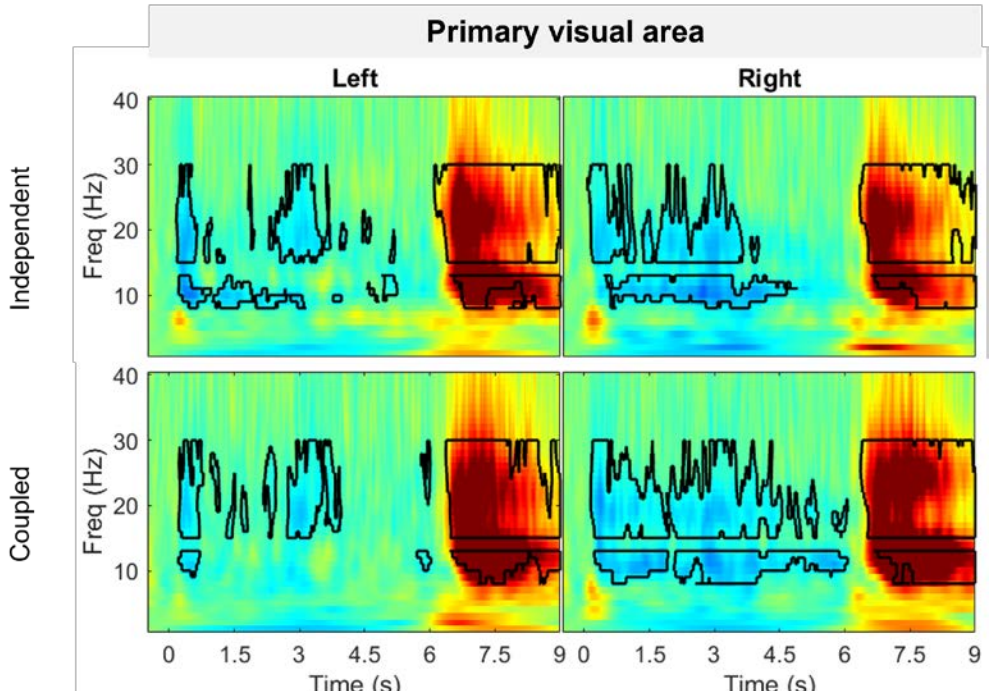
Primary visual area
Left
Right
Independent
Coupled
Freq (Hz)
40
30
20
10
0
1.5
3
4.5
6
7.5
9
Time (s)

(c)

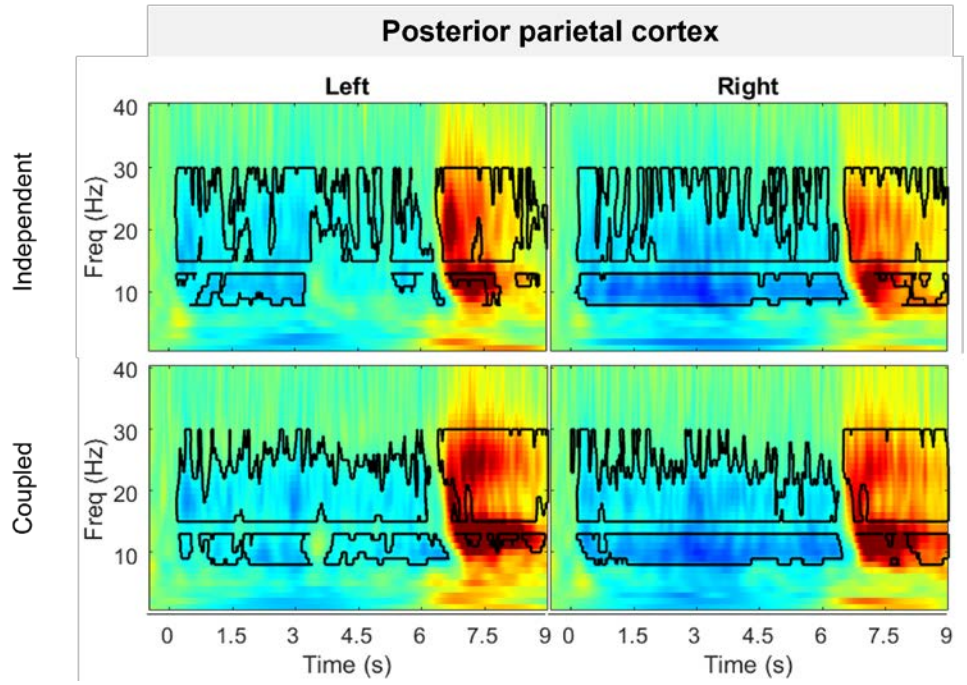

Figure A.1 Time-frequency response of (a) primary motor, (b) primary visual and (c) posterior parietal cortex localized in beta-band. The percent change was calculated using the average amplitude in time window of -500 ms to 0 seconds. The beta-synchrony after turn is distinct in left motor area in both conditions. In visual area, right visual area expressed the stronger beta desynchrony during the task than in left visual area. Both motor and visual area had post-task beta synchrony. In posterior parietal cortex, strong desynchrony maintained in both alpha and beta band in right area dominantly. Immediately after the task terminated, PPC expressed a weak beta synchrony in comparison to motor and visual area.

REFERENCES

1. Virani, S.S., Alonso, A., Aparicio, H.J., Benjamin, E.J., Bittencourt, M.S., Callaway, C.W., Carson, A.P., Chamberlain, A.M., Cheng, S., Delling, F.N. and Elkind, M.S., 2021. Heart disease and stroke statistics—2021 update: a report from the American Heart Association. *Circulation*, *143*(8), pp.e254-e743.
2. Lai, S.M., Studenski, S., Duncan, P.W. and Perera, S., 2002. Persisting consequences of stroke measured by the Stroke Impact Scale. *Stroke*, *33*(7), pp.1840-1844.
3. Cramer, S.C., 2008. Repairing the human brain after stroke: I. Mechanisms of spontaneous recovery. *Annals of neurology*, *63*(3), pp.272-287.
4. Hayward, K.S., Kramer, S.F., Dalton, E.J., Hughes, G.R., Brodtmann, A., Churilov, L., Cloud, G., Corbett, D., Jolliffe, L., Kaffenberger, T. and Rethnam, V., 2021. Timing and Dose of Upper Limb Motor Intervention After Stroke: A Systematic Review. *Stroke*, pp.STROKEAHA-121.
5. Bernhardt, J., Godecke, E., Johnson, L. and Langhorne, P., 2017. Early rehabilitation after stroke. *Current opinion in neurology*, *30*(1), pp.48-54.
6. Winters, C., van Wegen, E.E., Daffertshofer, A. and Kwakkel, G., 2015. Generalizability of the proportional recovery model for the upper extremity after an ischemic stroke. *Neurorehabilitation and neural repair*, *29*(7), pp.614-622.
7. Lang, C.E., Bland, M.D., Bailey, R.R., Schaefer, S.Y. and Birkenmeier, R.L., 2013. Assessment of upper extremity impairment, function, and activity after stroke: foundations for clinical decision making. *Journal of Hand Therapy*, *26*(2), pp.104-115.
8. LANGE, N., 1996. Statistical approaches to human brain mapping by functional magnetic resonance imaging. *Statistics in Medicine*, *15*(4), pp.389-428.

9. Ogawa, S., Lee, T.M., Nayak, A.S. and Glynn, P., 1990. Oxygenation-sensitive contrast in magnetic resonance image of rodent brain at high magnetic fields. *Magnetic resonance in medicine*, *14*(1), pp.68-78.

10. Roy, C.S. and Sherrington, C.S., 1890. On the regulation of the blood-supply of the brain. *The Journal of physiology*, *11*(1-2), pp.85-158.

11. Logothetis, N.K., Pauls, J., Augath, M., Trinath, T. and Oeltermann, A., 2001. Neurophysiological investigation of the basis of the fMRI signal. *nature*, *412*(6843), pp.150-157.

12. Yacoub, E., Shmuel, A., Pfeuffer, J., Van De Moortele, P.F., Adriany, G., Ugurbil, K. and Hu, X., 2001. Investigation of the initial dip in fMRI at 7 Tesla. *NMR in Biomedicine: An International Journal Devoted to the Development and Application of Magnetic Resonance In Vivo*, *14*(7-8), pp.408-412.

13. Krüger, G., Kastrup, A. and Glover, G.H., 2001. Neuroimaging at 1.5 T and 3.0 T: Comparison of oxygenation-sensitive magnetic resonance imaging. *Magnetic Resonance in Medicine: An Official Journal of the International Society for Magnetic Resonance in Medicine*, *45*(4), pp.595-604.

14. Lance, J.W., 1980. The control of muscle tone, reflexes, and movement: Robert Wartenbeg Lecture. Neurology, 30(12), pp.1303-1303.

15. Li, S., Chang, S.H., Francisco, G.E. and Verduzco-Gutierrez, M., 2014. Acoustic startle reflex in patients with chronic stroke at different stages of motor recovery: a pilot study. *Topics in stroke rehabilitation*, *21*(4), pp.358-370.

16. Wolpert, D.M. and Kawato, M., 1998. Multiple paired forward and inverse models for motor control. *Neural networks*, *11*(7-8), pp.1317-1329.

17. Woodworth, R.S., 1899. Accuracy of voluntary movement. *The Psychological Review: Monograph Supplements*, *3*(3), p.i.

18. Rondot, P., De Recondo, J. and Dumas, J.L., 1977. Visuomotor ataxia. *Brain: a journal of neurology*, *100*(2), pp.355-376.

19. Battaglia-Mayer, A., Ferraina, S., Mitsuda, T., Marconi, B., Genovesio, A., Onorati, P., Lacquaniti, F. and Caminiti, R., 2000. Early coding of reaching in the parietooccipital cortex. *Journal of neurophysiology*, *83*(4), pp.2374-2391.

20. Culham, J.C. and Valyear, K.F., 2006. Human parietal cortex in action. *Current opinion in neurobiology*, *16*(2), pp.205-212.

21. Blohm, G., Alikhanian, H., Gaetz, W., Goltz, H.C., DeSouza, J.F., Cheyne, D.O. and Crawford, J.D., 2019. Neuromagnetic signatures of the spatiotemporal transformation for manual pointing. *NeuroImage*, *197*, pp.306-319.

22. Lemon, R.N., 2010. What drives corticospinal output?. *F1000 biology reports*, *2*.

23. Shibasaki, H., Sadato, N., Lyshkow, H., Yonekura, Y., Honda, M., Nagamine, T., Suwazono, S., Magata, Y., Ikeda, A., Miyazaki, M. and Fukuyama, H., 1993. Both primary motor cortex and supplementary motor area play an important role in complex finger movement. *Brain*, *116*(6), pp.1387-1398.

24. Jackson, S.R. and Husain, M., 1996. Visuomotor functions of the lateral pre-motor cortex. *Current opinion in neurobiology*, *6*(6), pp.788-795.

25. Salenius, S., Portin, K., Kajola, M., Salmelin, R. and Hari, R., 1997. Cortical control of human motoneuron firing during isometric contraction. *Journal of neurophysiology*, *77*(6), pp.3401-3405.

26. Thickbroom, G.W., Phillips, B.A., Morris, I., Byrnes, M.L. and Mastaglia, F.L., 1998. Isometric force-related activity in sensorimotor cortex measured with functional MRI. *Experimental brain research*, *121*(1), pp.59-64.
27. Longcamp, M., Tanskanen, T. and Hari, R., 2006. The imprint of action: Motor cortex involvement in visual perception of handwritten letters. *Neuroimage*, *33*(2), pp.681-688.
28. Siegel, M., Engel, A.K. and Donner, T.H., 2011. Cortical network dynamics of perceptual ecision-making in the human brain. *Frontiers in human neuroscience*, *5*, p.21.
29. Taschereau-Dumouchel, V. and Hétu, S., 2012. Visuomotor representations within the human primary motor cortex: the elusive markers of visuomotor associative learning. *Journal of Neuroscience*, *32*(3), pp.759-760.
30. Rao, N.G. and Donoghue, J.P., 2014. Cue to action processing in motor cortex populations. *Journal of neurophysiology*, *111*(2), pp.441-453.
31. Hari, R., 2006. Action–perception connection and the cortical mu rhythm. *Progress in brain research*, *159*, pp.253-260.
32. Goodale, M.A., 2011. Transforming vision into action. *Vision research*, *51*(13), pp.1567-1587.
33. Hayhoe, M.M., 2017. Vision and action. *Annual review of vision science*, *3*, pp.389-413.
34. Gale, D.J., Flanagan, J.R. and Gallivan, J.P., 2021. Human somatosensory cortex is modulated during motor planning. *Journal of Neuroscience*, *41*(27), pp.5909-5922.
35. V1 reponding to motor
36. Hansen, P., Kringelbach, M. and Salmelin, R. eds., 2010. *MEG: an introduction to methods*. Oxford university press.

37. Darvas, F., Pantazis, D., Kucukaltun-Yildirim, E. and Leahy, R.M., 2004. Mapping human brain function with MEG and EEG: methods and validation. *NeuroImage*, *23*, pp.S289-S299.

38. Burghoff, M., Albrecht, H.H., Hartwig, S., Hilschenz, I., Körber, R., Sander-Thömmes, T., Scheer, H., Voigt, J. and Trahms, L., 2009. SQUID system for MEG and low field magnetic resonance. *Metrol. Meas. Syst*, *16*(3), pp.371-376.

39. Weiergraeber, M., Papazoglou, A., Broich, K. and Mueller, R., 2016. Sampling rate, signal bandwidth and related pitfalls in EEG analysis. *Journal of neuroscience methods*, *268*, pp.53-55.

40. Başar, E., 2012. *Brain function and oscillations: volume I: brain oscillations. Principles and approaches*. Springer Science & Business Media.

41. Schürmann, M. and Başar, E., 2001. Functional aspects of alpha oscillations in the EEG. *International Journal of Psychophysiology*, *39*(2-3), pp.151-158.

42. Khanna, P. and Carmena, J.M., 2015. Neural oscillations: beta band activity across motor networks. *Current opinion in neurobiology*, *32*, pp.60-67.

43. Brodal, A. "Anatomy of the vestibular nuclei and their connections." Vestibular system part 1: Basic mechanisms. Springer, Berlin, Heidelberg, 1974. 239-352.

44. Biacabe, Bernard, et al. "Functional anatomy of auditory brainstem nuclei: application to the anatomical basis of brainstem auditory evoked potentials." Auris Nasus Larynx 28.1 (2001): 85-94.

45. Feldman, Robert G., Robert R. Young, and Werner Paul Koella, eds. "Spasticity, disordered motor control." Symposia Specialists, 1980.

46. Miller, Derek M., et al. "Asymmetries in vestibular evoked myogenic potentials in chronic stroke survivors with spastic hypertonia: evidence for a vestibulospinal role." Clinical Neurophysiology 125.10 (2014): 2070-2078.

47. Davis, Michael., et al. "A primary acoustic startle circuit: lesion and stimulation studies." Journal of Neuroscience 2.6 (1982): 791-805.

48. Beissner, F. "Functional MRI of the brainstem: common problems and their solutions." Clinical neuroradiology 25.2 (2015): 251-257.

49. Wildenberg, Joseph C., et al. "High-resolution fMRI detects neuromodulation of individual brainstem nuclei by electrical tongue stimulation in balance-impaired individuals." Neuroimage 56.4 (2011): 2129-2137.

50. Hettinger, Lawrence J., et al. "Vection and simulator sickness." Military Psychology 2.3 (1990): 171-181.

51. Pavlou, Marousa. "The use of optokinetic stimulation in vestibular rehabilitation." Journal of Neurologic Physical Therapy 34.2 (2010): 105-110.

52. Glover, Gary H. "Spiral imaging in fMRI." Neuroimage 62.2 (2012): 706-712.

53. Fischl, Bruce. "FreeSurfer." Neuroimage 62.2 (2012): 774-781.

54. Mai, Jürgen K., and Milan Majtanik. Human Brain in Standard MNI Space: A Comprehensive Pocket Atlas. Elsevier, 2017.

55. Iglesias, Juan Eugenio, et al. "Bayesian segmentation of brainstem structures in MRI." Neuroimage 113 (2015): 184-195.

56. Saulino, Michael, et al. "Medical cost impact of intrathecal baclofen therapy for severe spasticity." Neuromodulation: Technology at the Neural Interface 18.2 (2015): 141-149.

57. Akbas, T., Neptune, R. and Sulzer, J., 2019. Neuromusculoskeletal simulation reveals abnormal rectus femoris-gluteus medius coupling in post-stroke gait. Frontiers in neurology, 10, p.301.

58. Akbas, T., Kim, K., Doyle, K., Manella, K., Lee, R., Spicer, P., Knikou, M. and Sulzer, J., 2019. Rectus femoris hyperreflexia predicts knee flexion angle in Stiff-Knee gait after stroke. bioRxiv, p.699108.

59. Burke, David, Jörg Wissel, and Geoffrey A. Donnan. "Pathophysiology of spasticity in stroke." Neurology 80.3 Supplement 2 (2013): S20-S26.

60. Nielsen, Jens Bo, Clarissa Crone, and H. Hultborn. "The spinal pathophysiology of spasticity–from a basic science point of view." Acta physiologica189.2 (2007): 171-180.

61. Biacabe, B., Chevallier, J.M., Avan, P. and Bonfils, P., 2001. Functional anatomy of auditory brainstem nuclei: application to the anatomical basis of brainstem auditory evoked potentials. Auris Nasus Larynx, 28(1), pp.85-94.

62. V. Singh, J. Pfeuffer, T. Zhao, and D. Ress, "Evaluation of spiral acquisition variants for functional imaging of human superior colliculus at 3T field strength," Magn Reson Med, vol. 79, pp. 1931-1940, Apr 2018.

63. Chungmin Han, David Ress, Aurora Ramos, Natasha De LaRosa, Sheng Li and James S Sulzer “Brainstem BOLD response to visual and acoustic stimuli” in review at the 42nd Annual International Conferences of the IEEE Engineering in Medicine and Biology Society

64. Glover, G.H., Li, T.Q. and Ress, D., 2000. Image-based method for retrospective correction of physiological motion effects in fMRI: RETROICOR. Magnetic Resonance in Medicine:

An Official Journal of the International Society for Magnetic Resonance in Medicine, 44(1), pp.162-167.

65. Pavlou, M., 2010. The use of optokinetic stimulation in vestibular rehabilitation. Journal of Neurologic Physical Therapy, 34(2), pp.105-110.

66. Jenkinson M, Beckmann CF, Behrens TE, Woolrich MW, Smith SM. Fsl. Neuroimage. 2012 Aug 15;62(2):782-90.

67. Iglesias, J.E., Van Leemput, K., Bhatt, P., Casillas, C., Dutt, S., Schuff, N., Truran-Sacrey, D., Boxer, A., Fischl, B. and Alzheimer's Disease Neuroimaging Initiative, 2015. Bayesian segmentation of brainstem structures in MRI. Neuroimage, 113, pp.184-195.

68. Fearnley, J. M. & Lees, A. J. Ageing and Parkinson's disease: substantia nigra regional selectivity. Brain 114, 2283–2301 (1991).

69. Dehan CP, Jerger J. Analysis of gender differences in the auditory brainstem response. The Laryngoscope. 1990 Jan;100(1):18-24.

70. Arshad Q, Nigmatullina Y, Bronstein AM. Handedness-related cortical modulation of the vestibular-ocular reflex. Journal of Neuroscience. 2013 Feb 13;33(7):3221-7.

71. Källstrand J, Nehlstedt SF, Sköld ML, Nielzén S. Lateral asymmetry and reduced forward masking effect in early brainstem auditory evoked responses in schizophrenia. Psychiatry research. 2012 Apr 30;196(2-3):188-93.

72. Muir, R. B., and R. N. Lemon. "Corticospinal neurons with a special role in precision grip." Brain research 261.2 (1983): 312-316.

73. J. S. Sulzer, Chib, V. S., Hepp-Reymond, M., Kollias, S., and Gassert, R., "BOLD correlations to force in precision grip: an event-related study," Engineering in Medicine and Biology Society, EMBC, 2011 Annual International Conference of the IEEE. IEEE, pp. 2342-2346, 2011.

74. Kuhtz-Buschbeck, Johann P., H. Henrik Ehrsson, and Hans Forssberg. "Human brain activity in the control of fine static precision grip forces: an fMRI study." European Journal of Neuroscience 14.2 (2001): 382-390.

75. Ehrsson, H. Henrik, Anders Fagergren, and Hans Forssberg. "Differential fronto-parietal activation depending on force used in a precision grip task: an fMRI study." Journal of Neurophysiology 85.6 (2001): 2613-2623.

76. Prodoehl, Janey, Daniel M. Corcos, and David E. Vaillancourt. "Basal ganglia mechanisms underlying precision grip force control." Neuroscience & Biobehavioral Reviews 33.6 (2009): 900-908.

77. Cole, Kelly J., and Christina L. Beck. "The stability of precision grip force in older adults." Journal of motor behavior 26.2 (1994): 171-177.

78. Diermayr, Gudrun, Tara L. McIsaac, and Andrew M. Gordon. "Finger force coordination underlying object manipulation in the elderly–a mini-review." Gerontology 57.3 (2010): 217-227.

79. Spirduso, Waneen W., et al. "Quantification of manual force control and tremor." Journal of motor behavior 37.3 (2005): 197-210.

80. Arata, Jumpei, et al. "MRI-compatible grasping force sensor with an inclined double parallel structure using fiber optics." Transactions of the Institute of Systems, Control and Information Engineers 26.3 (2013): 110-116.

81. Chen, WeiHai, et al. "A novel flexure-based uniaxial force sensor with large range and high resolution." Science China Technological Sciences 56.8 (2013): 1940-1948.

82. Tan, U-Xuan, et al. "Triaxial MRI-compatible fiber-optic force sensor." IEEE Transactions on Robotics 27.1 (2011): 65-74.

83. Kesner, Samuel B., and Robert D. Howe. "Design principles for rapid prototyping forces sensors using 3-D printing." IEEE/ASME Transactions on mechatronics 16.5 (2011): 866-870.

84. Turkseven, Melih, and Jun Ueda. "Analysis of an MRI compatible force sensor for sensitivity and precision." IEEE Sensors Journal 13.2 (2013): 476-486.

85. Bützer, Tobias L., et al. "Design and Evaluation of a Fiber-Optic Grip Force Sensor with Compliant 3D-Printable Structure for (f) MRI Applications." Journal of Sensors 2016 (2016).

86. Bützer, Tobias, Bogdan Vigaru, and Roger Gassert. "Design and evaluation of a compact, integrated fMRI-compatible force sensor printed by additive manufacturing." World Haptics Conference (WHC), 2015 IEEE. IEEE, 2015.

87. Rocca, M. A., et al. "Evidence for widespread movement-associated functional MRI changes in patients with PPMS." Neurology 58.6 (2002): 866-872.

88. Lutz, K., et al. "Asymmetry of cortical activation during maximum and convenient tapping speed." Neuroscience letters 373.1 (2004): 61-66.

89. Sakai, K., Hikosaka, O., Miyauchi, S., Takino, R., Sasaki, Y. and Pütz, B., 1998. Transition of brain activation from frontal to parietal areas in visuomotor sequence learning. Journal of Neuroscience, 18(5), pp.1827-1840.

90. Michel, C.M., Thut, G., Morand, S., Khateb, A., Pegna, A.J., de Peralta, R.G., Gonzalez, S., Seeck, M. and Landis, T., 2001. Electric source imaging of human brain functions. Brain Research Reviews, 36(2-3), pp.108-118.

91. Wolpert, D.M., Goodbody, S.J. and Husain, M., 1998. Maintaining internal representations: the role of the human superior parietal lobe. Nature neuroscience, 1(6), pp.529-533.

92. Woodworth, R.S., 1899. Accuracy of voluntary movement. The Psychological Review: Monograph Supplements, 3(3), p.i.

93. Rondot, P., Recondo, J. & de Ribadeau Dumas, J. Visuomotor ataxia. Brain 100, 355–376 (1977).

94. Battaglia-Mayer, A., Ferraina, S., Mitsuda, T., Marconi, B., Genovesio, A., Onorati, P., Lacquaniti, F. and Caminiti, R., 2000. Early coding of reaching in the parietooccipital cortex. Journal of neurophysiology, 83(4), pp.2374-2391.

95. Culham, J.C., Cavina-Pratesi, C. and Singhal, A., 2006. The role of parietal cortex in visuomotor control: what have we learned from neuroimaging?. Neuropsychologia, 44(13), pp.2668-2684.

96. Blohm, G., Alikhanian, H., Gaetz, W., Goltz, H.C., DeSouza, J.F., Cheyne, D.O. and Crawford, J.D., 2019. Neuromagnetic signatures of the spatiotemporal transformation for manual pointing. NeuroImage, 197, pp.306-319.

97. Lemon, R.N., 2010. What drives corticospinal output?. F1000 biology reports, 2.

98. Foerster, O., 1936. The motor cortex in man in the light of Hughlings Jackson's doctrines. Brain, 59(2), pp.135-159.

99. Penfield, W. and Rasmussen, T., 1950. The cerebral cortex of man; a clinical study of localization of function.

100. Muir, R.B. and Lemon, R.N., 1983. Corticospinal neurons with a special role in precision grip. Brain research, 261(2), p

101. Grafton, S.T., MAZZIOTTA, J.C., Woods, R.P. and Phelps, M.E., 1992. Human functional anatomy of visually guided finger movements. Brain, 115(2), pp.565-587.

102. Shibasaki, H., Sadato, N., Lyshkow, H., Yonekura, Y., Honda, M., Nagamine, T., Suwazono, S., Magata, Y., Ikeda, A., Miyazaki, M. and Fukuyama, H., 1993. Both primary

motor cortex and supplementary motor area play an important role in complex finger movement. Brain, 116(6), pp.1387-1398.

103. Jackson, S.R. and Husain, M., 1996. Visuomotor functions of the lateral pre-motor cortex. Current opinion in neurobiology, 6(6), pp.788-795.

104. Salenius, S., Portin, K., Kajola, M., Salmelin, R. and Hari, R., 1997. Cortical control of human motoneuron firing during isometric contraction. Journal of neurophysiology, 77(6), pp.3401-3405.

105. Byrnes, M.L., Thickbroom, G.W., Wilson, S.A., Sacco, P., Shipman, J.M., Stell, R. and Mastaglia, F.L., 1998. The corticomotor representation of upper limb muscles in writer's cramp and changes following botulinum toxin injection. Brain: a journal of neurology, 121(5), pp.977-988.

106. Salinas, E. and Romo, R., 1998. Conversion of sensory signals into motor commands in primary motor cortex. Journal of Neuroscience, 18(1), pp.499-511.

107. Longcamp, M., Tanskanen, T. and Hari, R., 2006. The imprint of action: Motor cortex involvement in visual perception of handwritten letters. Neuroimage, 33(2), pp.681-688.

108. Rao, N.G. and Donoghue, J.P., 2014. Cue to action processing in motor cortex populations. Journal of neurophysiology, 111(2), pp.441-453.

109. Siegel, M., Engel, A.K. and Donner, T.H., 2011. Cortical network dynamics of perceptual decision-making in the human brain. Frontiers in human neuroscience, 5, p.21.

110. Hari, R., 2006. Action–perception connection and the cortical mu rhythm. Progress in brain research, 159, pp.253-260.

111. Goodale, M.A., 2011. Transforming vision into action. Vision research, 51(13), pp.1567-1587.

112. Hayhoe, M.M., 2017. Vision and action. Annual review of vision science, 3, pp.389-413.

113. Gale, D.J., Flanagan, J.R. and Gallivan, J.P., 2021. Human somatosensory cortex is modulated during motor planning. Journal of Neuroscience, 41(27), pp.5909-5922.

114. Benedetto, A., Binda, P., Costagli, M., Tosetti, M. and Morrone, M.C., 2021. Predictive visuo-motor communication through neural oscillations. Current Biology.

115. Johnston, J., Rearick, M. and Slobounov, S., 2001. Movement-related cortical potentials associated with progressive muscle fatigue in a grasping task. Clinical neurophysiology, 112(1), pp.68-77.

116. Hinder, M.R., Tresilian, J.R., Riek, S. and Carson, R.G., 2008. The contribution of visual feedback to visuomotor adaptation: how much and when?. Brain research, 1197, pp.123-134.

117. Coombes, S.A., Corcos, D.M., Sprute, L. and Vaillancourt, D.E., 2010. Selective regions of the visuomotor system are related to gain-induced changes in force error. Journal of neurophysiology, 103(4), pp.2114-2123.

118. Li, K., Marquardt, T.L. and Li, Z.M., 2013. Removal of visual feedback lowers structural variability of inter-digit force coordination during sustained precision pinch. Neuroscience letters, 545, pp.1-5.

119. Kang, N. and Cauraugh, J.H., 2015. Bimanual force variability in chronic stroke: with and without visual information. Neuroscience letters, 587, pp.41-45.

120. Lebar, N., Bernier, P.M., Guillaume, A., Mouchnino, L. and Blouin, J., 2015. Neural correlates for task-relevant facilitation of visual inputs during visually-guided hand movements. NeuroImage, 121, pp.39-50.

121. Johnson, V., Hsu, W.Y., Ostrand, A.E., Gazzaley, A. and Zanto, T.P., 2020. Multimodal sensory integration: Diminishing returns in rhythmic synchronization. Journal of Experimental Psychology: Human Perception and Performance.

122. Forssberg, H., Kinoshita, H., Eliasson, A.C., Johansson, R.S., Westling, G. and Gordon, A.M., 1992. Development of human precision grip. Experimental Brain Research, 90(2), pp.393-398.

123. Fellows, S.J., Noth, J. and Schwarz, M., 1998. Precision grip and Parkinson's disease. Brain: a journal of neurology, 121(9), pp.1771-1784.

124. Eliasson, A.C., Forssberg, H., Hung, Y.C. and Gordon, A.M., 2006. Development of hand function and precision grip control in individuals with cerebral palsy: a 13-year follow-up study. Pediatrics, 118(4), pp.e1226-e1236.

125. Lindberg, P., Ody, C., Feydy, A. and Maier, M.A., 2009. Precision in isometric precision grip force is reduced in middle-aged adults. Experimental brain research, 193(2), pp.213-224.

126. Gordon, A.M., Bleyenheuft, Y. and Steenbergen, B., 2013. Pathophysiology of impaired hand function in children with unilateral cerebral palsy. Developmental Medicine & Child Neurology, 55, pp.32-37.

127. Patel, P., Kaingade, S.R., Wilcox, A. and Lodha, N., 2020. Force control predicts fine motor dexterity in high-functioning stroke survivors. Neuroscience letters, 729, p.135015

128. Kuhtz-Buschbeck, J.P., Ehrsson, H.H. and Forssberg, H., 2001. Human brain activity in the control of fine static precision grip forces: an fMRI study. European Journal of Neuroscience, 14(2), pp.382-390.

129. Ehrsson, H.H., Fagergren, A. and Forssberg, H., 2001. Differential fronto-parietal activation depending on force used in a precision grip task: an fMRI study. Journal of neurophysiology, 85(6), pp.2613-2623.

130. Kilner, J.M., Alonso-Alonso, M., Fisher, R. and Lemon, R.N., 2002. Modulation of synchrony between single motor units during precision grip tasks in humans. The Journal of physiology, 541(3), pp.937-948.

131. Kilner, J.M., Salenius, S., Baker, S.N., Jackson, A., Hari, R. and Lemon, R.N., 2003. Task-dependent modulations of cortical oscillatory activity in human subjects during a bimanual precision grip task. Neuroimage, 18(1), pp.67-73.

132. Muthukumaraswamy, S.D., Johnson, B.W. and McNair, N.A., 2004. Mu rhythm modulation during observation of an object-directed grasp. Cognitive brain research, 19(2), pp.195-201.

133. Rilk, A.J., Soekadar, S.R., Sauseng, P. and Plewnia, C., 2011. Alpha coherence predicts accuracy during a visuomotor tracking task. Neuropsychologia, 49(13), pp.3704-3709.

134. Keisker, B., Hepp-Reymond, M.C., Blickenstorfer, A. and Kollias, S.S., 2010. Differential representation of dynamic and static power grip force in the sensorimotor network. European Journal of Neuroscience, 31(8), pp.1483-1491.

135. Neely, K.A., Coombes, S.A., Planetta, P.J. and Vaillancourt, D.E., 2013. Segregated and overlapping neural circuits exist for the production of static and dynamic precision grip force. Human brain mapping, 34(3), pp.698-712.

136. Leocani, L., Toro, C., Manganotti, P., Zhuang, P. and Hallett, M., 1997. Event-related coherence and event-related desynchronization/synchronization in the 10 Hz and 20 Hz EEG during self-paced movements. Electroencephalography and Clinical Neurophysiology/Evoked Potentials Section, 104(3), pp.199-206.

137. Pfurtscheller, G. and Aranibar, A., 1977. Event-related cortical desynchronization detected by power measurements of scalp EEG. Electroencephalography and clinical neurophysiology, 42(6), pp.817-826.

138. Pfurtscheller, G., Stancak Jr, A. and Neuper, C., 1996. Event-related synchronization (ERS) in the alpha band—an electrophysiological correlate of cortical idling: a review. International journal of psychophysiology, 24(1-2), pp.39-46.

139. Pfurtscheller, G. and Da Silva, F.L., 1999. Event-related EEG/MEG synchronization and desynchronization: basic principles. Clinical neurophysiology, 110(11), pp.1842-1857.

140. Cassim, F., Monaca, C., Szurhaj, W., Bourriez, J.L., Defebvre, L., Derambure, P. and Guieu, J.D., 2001. Does post-movement beta synchronization reflect an idling motor cortex?. Neuroreport, 12(17), pp.3859-3863.

141. Schnitzler, A., Salenius, S., Salmelin, R., Jousmäki, V. and Hari, R., 1997. Involvement of primary motor cortex in motor imagery: a neuromagnetic study. Neuroimage, 6(3), pp.201-208.

142. Schnitzler, A., Salenius, S., Salmelin, R., Jousmäki, V. and Hari, R., 1997. Involvement of primary motor cortex in motor imagery: a neuromagnetic study. Neuroimage, 6(3), pp.201-208.

143. Neuper, C., Scherer, R., Reiner, M. and Pfurtscheller, G., 2005. Imagery of motor actions: Differential effects of kinesthetic and visual–motor mode of imagery in single-trial EEG. Cognitive brain research, 25(3), pp.668-677.

144. Kurz, M.J., Proskovec, A.L., Gehringer, J.E., Heinrichs-Graham, E. and Wilson, T.W., 2017. Children with cerebral palsy have altered oscillatory activity in the motor and visual cortices during a knee motor task. NeuroImage: Clinical, 15, pp.298-305

145. Richter, C.G., Coppola, R. and Bressler, S.L., 2018. Top-down beta oscillatory signaling conveys behavioral context in early visual cortex. Scientific reports, 8(1), pp.1-12.

146. Gross, J., 2019. Magnetoencephalography in cognitive neuroscience: a primer. Neuron, 104(2), pp.189-204.

147. Oldfield, R.C., 1971. The assessment and analysis of handedness: the Edinburgh inventory. Neuropsychologia, 9(1), pp.97-113.

148. Spirduso, W.W., Francis, K., Eakin, T. and Stanford, C., 2005. Quantification of manual force control and tremor. *Journal of motor behavior, 37*(3), pp.197-210.

149. Han, C., Oblak, E., Abraham, L., Ferrari, P., McManis, M., Schnyer, D. and Sulzer, J., 2017, July. An MRI-compatible force sensor for measuring differential isometric precision grip force. In *2017 39th Annual International Conference of the IEEE Engineering in Medicine and Biology Society (EMBC)* (pp. 791-794). IEEE.

150. Soderberg, G.L., 1992. Selected topics in surface electromyography for use in the occupational setting: expert perspectives. US Department of Health and Human Services, Public Health Service, Centers for Disease Control, National Institute for Occupational Safety and Health

151. Jobst, C., Ferrari, P., Isabella, S. and Cheyne, D., 2018. BrainWave: A MATLAB toolbox for beamformer source analysis of MEG data. Frontiers in neuroscience, 12, p.587.

152. Van Veen, B.D. and Buckley, K.M., 1988. Beamforming: A versatile approach to spatial filtering. *IEEE assp magazine*, *5*(2), pp.4-24.

153. Vrba, J. and Robinson, S.E., 2001. Signal processing in magnetoencephalography. Methods, 25(2), pp.249-271.

154. Sekihara, K., Nagarajan, S.S., Poeppel, D. and Marantz, A., 2004. Asymptotic SNR of scalar and vector minimum-variance beamformers for neuromagnetic source reconstruction. IEEE transactions on biomedical engineering, 51(10), pp.1726-1734.

155. Robinson, S.E. and Vrba, J., 1999. Functional neuroimaging by synthetic aperture magnetometry (SAM) Recent Adv.

156. Sekihara, K., Nagarajan, S.S., Poeppel, D., Marantz, A. and Miyashita, Y., 2001. Reconstructing spatio-temporal activities of neural sources using an MEG vector beamformer technique. IEEE Transactions on Biomedical Engineering, 48(7), pp.760-771.

157. Van Veen, B.D., Van Drongelen, W., Yuchtman, M. and Suzuki, A., 1997. Localization of brain electrical activity via linearly constrained minimum variance spatial filtering. IEEE Transactions on biomedical engineering, 44(9), pp.867-880.

158. Vrba, J. and Robinson, S.E., 2001. Signal processing in magnetoencephalography. Methods, 25(2), pp.249-271.

159. Barnes, G.R. and Hillebrand, A., 2003. Statistical flattening of MEG beamformer images. Human brain mapping, 18(1), pp.1-12.

160. Tesche, C.D., Uusitalo, M.A., Ilmoniemi, R.J., Huotilainen, M., Kajola, M. and Salonen, O., 1995. Signal-space projections of MEG data characterize both distributed and well-localized neuronal sources. Electroencephalography and clinical neurophysiology, 95(3), pp.189-200.

161. Jenkinson, M., Beckmann, C.F., Behrens, T.E., Woolrich, M.W. and Smith, S.M., 2012. Fsl. Neuroimage, 62(2), pp.782-790.

162. Hillebrand, A. and Barnes, G.R., 2005. Beamformer analysis of MEG data. International review of neurobiology, 68, pp.149-171.

163. Cheyne, D.O. and Papanicolaou, A.C., 2015. Chapter II: Magnetoencephalography and magnetic source imaging.

164. Daubechies, I., 1993. Wavelets: Algorithms and Applications. Science, 262(5139), pp.1589-1592.

165. Neuper, C. and Pfurtscheller, G., 2001. Event-related dynamics of cortical rhythms: frequency-specific features and functional correlates. International journal of psychophysiology, 43(1), pp.41-58.

166. Kilavik, B.E., Zaepffel, M., Brovelli, A., MacKay, W.A. and Riehle, A., 2013. The ups and downs of beta oscillations in sensorimotor cortex. Experimental neurology, 245, pp.15-26.

167. Swann, N., Tandon, N., Canolty, R., Ellmore, T.M., McEvoy, L.K., Dreyer, S., DiSano, M. and Aron, A.R., 2009. Intracranial EEG reveals a time-and frequency-specific role for the right inferior frontal gyrus and primary motor cortex in stopping initiated responses. Journal of Neuroscience, 29(40), pp.12675-12685.

168. Rowland, N.C., De Hemptinne, C., Swann, N.C., Qasim, S., Miocinovic, S., Ostrem, J., Knight, R.T. and Starr, P.A., 2015. Task-related activity in sensorimotor cortex in Parkinson's disease and essential tremor: changes in beta and gamma bands. Frontiers in human neuroscience, 9, p.512.

169. Wagner, J., Wessel, J.R., Ghahremani, A. and Aron, A.R., 2018. Establishing a right frontal beta signature for stopping action in scalp EEG: implications for testing inhibitory control in other task contexts. Journal of cognitive neuroscience, 30(1), pp.107-118.

170. Baker, S.N., 2007. Oscillatory interactions between sensorimotor cortex and the periphery. Current opinion in neurobiology, 17(6), pp.649-655.

171. Alegre, M., Labarga, A., Gurtubay, I.G., Iriarte, J., Malanda, A. and Artieda, J., 2002. Beta electroencephalograph changes during passive movements: sensory afferences contribute to beta event-related desynchronization in humans. Neuroscience letters, 331(1), pp.29-32.

172. Tan, H., Jenkinson, N. and Brown, P., 2014. Dynamic neural correlates of motor error monitoring and adaptation during trial-to-trial learning. Journal of Neuroscience, 34(16), pp.5678-5688.

173. Tan, H., Wade, C. and Brown, P., 2016. Post-movement beta activity in sensorimotor cortex indexes confidence in the estimations from internal models. Journal of Neuroscience, 36(5), pp.1516-1528.

174. Gaetz, W., Edgar, J.C., Wang, D.J. and Roberts, T.P., 2011. Relating MEG measured motor cortical oscillations to resting γ-aminobutyric acid (GABA) concentration. Neuroimage, 55(2), pp.616-621.

175. Muthukumaraswamy, S.D., Myers, J.F., Wilson, S.J., Nutt, D.J., Lingford-Hughes, A., Singh, K.D. and Hamandi, K., 2013. The effects of elevated endogenous GABA levels on movement-related network oscillations. Neuroimage, 66, pp.36-41.

176. Jia, J., Fan, Y. and Luo, H., 2021. Alpha-Band Phase Modulates Bottom-up Feature Processing. Cerebral Cortex.

177. Alegre, M., Alvarez-Gerriko, I., Valencia, M., Iriarte, J. and Artieda, J., 2008. Oscillatory changes related to the forced termination of a movement. Clinical Neurophysiology, 119(2), pp.290-300.

178. Nakayashiki, K., Saeki, M., Takata, Y., Hayashi, Y. and Kondo, T., 2014. Modulation of event-related desynchronization during kinematic and kinetic hand movements. Journal of neuroengineering and rehabilitation, 11(1), pp.1-9.

179. Roser, M.E., Fiser, J., Aslin, R.N. and Gazzaniga, M.S., 2011. Right hemisphere dominance in visual statistical learning. Journal of cognitive neuroscience, 23(5), pp.1088-1099.

180. Nishimoto, S. and Nishida, S., 2016. Lining up brains via a common representational space. Trends in cognitive sciences, 20(8), pp.565-567.